10-10-2024 10:00 AM

Pressure-Tuned Structures and Optoelectronic Properties of 2D Hybrid Organic-Inorganic Perovskites

Aditya Kutty Mr., *Western University*

Supervisor: Song, Yang, *The University of Western Ontario*

A thesis submitted in partial fulfillment of the requirements for the Master of Science degree in Chemistry

Abstract

In recent years research interest and the use of 2D hybrid organic-inorganic perovskites (HOIPs) in optoelectronic devices, in particular solar cells, has increased substantially due to their high stability, relatively cheap costs and ease of fabrication, and intriguing optoelectronic properties, in comparison to their 3D counterparts. Optimization of these properties for solar cells applications however still requires more in-depth studies. Of the various methods used previously, high external pressure has emerged as a clean and effective method for inducing modifications to the structures of 2D HOIPs, in turn inducing modifications to the optoelectronic properties. In this study, we report the first high-pressure studies on three different 2D HOIPs: N,N-dimethylphenylene-*p*-diammonium (DPDA) lead iodide ($DPDAPbI_4$), cyclohexane methylamine (CMA) methyl ammonium (MA) lead iodide ($CMA_2MAPb_2I_7$), and cyclohexane methylamine (CMA) formamidinium (FA) lead iodide ($CMA_2FAPb_2I_7$).

The effects of high-pressure on both the structures and optoelectronic properties of $DPDAPbI_4$ were studied by performing Raman spectroscopy, Fourier-transform infrared (FTIR) spectroscopy X-ray diffraction (XRD), photoluminescence (PL), and UV-Vis absorption measurements. The vibrational spectroscopy in tandem with the XRD and PL measurements identifies a phase transition. Vibrational spectroscopy also indicates pressure-induced enhancement of the N–H···I hydrogen bonding interactions between the NH_3^+ groups and the lead iodide octahedra, indicating shortening of the Pb-I bond lengths, confirmed by the computational studies, thus providing critical information regarding the mechanism behind the bandgap reduction. Synchrotron XRD measurements confirm the phase transition with distortion analysis indicating enhancement of the

octahedral distortion between 1-2 GPa. The enhancements in both the hydrogen bonding interactions and the octahedral distortion were found to constitute the origins behind the phase transition. PL measurements show a redshift of the free exciton (FE) peak along with broadening of the self-trapped exciton (STE) peak at low-pressure. UV-Vis absorption confirms the bandgap reduction, and all measurements indicate reversible structural modifications and pressure-induced optoelectronic properties. For $CMA_2MAPb_2I_7$ and $CMA_2FAPb_2I_7$ FTIR measurements suggest a possible phase transition between 3-5 GPa along with N–H···I hydrogen bonding interactions between the NH_3^+ groups and the lead iodide octahedra. Synchrotron XRD measurements confirm the phase transition while analysis of the LeBail refined cell parameters indicates negative linear compressibility for both compounds. PL measurements show a redshift for both major PL peak and UV-Vis absorption shows a bandgap reduction for both compounds. In general, the structural modifications and optoelectronic properties were found to be reversible upon decompression. Our results provide a solid understanding of the pressure effects on the structures and optoelectronic properties of both n =1 and n = 2 2D HOIPs with differing organic spacers, a crucial step for the use of 2D HOIPs in applications such as solar cells.

Keywords: 2D hybrid organic-inorganic perovskites, high-pressure, diamond anvil cell, Raman spectroscopy, Fourier-transform infrared spectroscopy, X-ray diffraction, photoluminescence, UV-Vis absorption, phase transition, bandgap

Summary for Lay Audience

The use of sustainable energy sources, in particular solar energy, has increased significantly over the years as a result of the increasing concerns of climate change. As such, research has heavily focused on two-dimensional hybrid organic-inorganic perovskites (HOIPs) for use in solar cells. 2D HOIPs are semiconducting materials consisting of an inorganic octahedra separated by organic spacers. The efficiency of perovskite solar cells has increased considerably over the years. However, optimization of their properties, in particular for solar cells applications, still requires more in-depth studies, thus modification of said properties is crucial. The goal is to permanently reduce the bandgap of 2D HOIPs to achieve the limit for maximum efficiency.

In this work we study the effects of high-pressure (HP) on 3 2D HOIPs, $DPDAPbI_4$, $CMA_2MAPb_2I_7$, and $CMA_2FAPb_2I_7$ with differing organic spacers. We use Raman spectroscopy, Fourier-transform infrared (FTIR) spectroscopy, X-ray diffraction (XRD), photoluminescence (PL), and UV-Vis absorption measurements. Our findings provide critical information on the behavior of both the structures, in particular phase transitions, hydrogen bonding, distortion, and amorphization, and the optoelectronic properties, such as the PL emissions and the bandgap upon pressure treatment. Understanding the changes in the optoelectronic properties is crucial for applications such as solar cells. These findings in turn also provide a solid understanding of the behavior of 2D HOIPs with both soft and rigid ring spacers as well as a basis for modifying the structures through HP to achieve the desired properties for solar cell applications.

Statement of Co-Authorship

All samples studied were synthesized by Matthew Hautzinger from Prof. Song Jin's group at the University of Wisconsin-Madison. All computations were performed by Rongfeng Guan from Dr. Yang Song's group at the University of Western Ontario. Initial Raman and FTIR measurements on $DPDAPbI_4$ were conducted by former Master Student Jesse Ratte. Further Raman and FTIR measurements were conducted by Aditya Kutty to help confirm the results. FTIR measurements for $CMA_2MAPb_2I_7$ and $CMA_2FAPb_2I_7$ were collected by both Aditya Kutty and Sean Tao. Far-IR measurements were performed at the Canadian Light Source by Andrew Yin from Dr. Yang Song's group and analysis was performed by Aditya Kutty.

XRD measurements were performed remotely by Jesse Ratte and Jingyan Liu with assistance from Dr. Maddury Somayazulu and Dr. Guoyin Shen of the Advanced photon source, with initial analysis for $DPDAPbI_4$ performed by Jesse Ratte. All XRD analysis for the CMA compounds was performed by Aditya Kutty.

Photoluminescence measurements were performed by Sean Tao and Aditya Kutty and all UV-Vis absorption measurements were performed by Aditya Kutty. All photoluminescence and UV-Vis absorption analysis was performed by Aditya Kutty. All analysis not previously performed by Jesse Ratte was performed by Aditya Kutty with assistance from Dr. Yang Song. Aditya Kutty wrote the draft of the thesis and Dr. Yang Song edited the content.

Acknowledgements

Firstly, I would like to acknowledge and thank my supervisor Dr. Yang Song for being a fantastic mentor and for his continued support throughout this project. His support and patience during my Master's has been invaluable. The guidance and assistance he has given me has not only helped make me a better researcher, but also a better presenter and communicator in an academic setting. I will be forever grateful for everything you have done for me.

I would like to thank Matthew Hautzinger of Prof. Song Jin's group at the University of Wisconsin-Madison for synthesizing the samples used in this study. I would also like to acknowledge Jesse Ratte for his previous work on $DPDAPbI_4$, Jingyan Liu for her help with the XRD measurements, and Andrew Yin for completing the Far-IR measurements. Additionally, I would also like to acknowledge Rongfeng Guan for his contributions towards the computational work in this project. Furthermore, I would like to acknowledge Sean Tao for his help with the FTIR and photoluminescence measurements of the CMA samples. You have all made these experiments and analysis possible, and for that I will be forever grateful.

Lastly, I would like to thank the members of the Yang Song research group, my friends, and my parents for their amazing support throughout my Master's. I would like to give particular thanks to my parents, whose continued support throughout not only my Master's but my entire life has been vital, and I would not be the person I am today without their love and support. Thank you for everything.

Table of Contents

List of Figures

List of Tables

List of Abbreviations

BA	Butylammonium
CBM	Conduction band minimum
CMA	Cyclohexane methyl amine
DFT	Density functional theory
DJ	Dion-Jacobson
DPDA	N,N-dimethylphenylene-*p*-diammonium
FA	Formamidinium
FE	Free Exciton
FET	Field effect transistor
HOIP	Hybrid organic-inorganic perovskite
LED	Light emitting diode
LHP	Lead halide perovskite
MA	Methylammonium
MHP	Metal halide perovskite
PDOS	Partial density of states
PEA	Phenylethylammonium
RP	Ruddlesden-Propper
STE	Self-trapped exciton
VBM	Valence band maximum

1. Introduction

1.1 Perovskites in Energy Applications

It has been well documented that the continued use of current sources of energy, such as fossil fuels, has had a severely damaging impact on the environment, leading to intense changes in climate and increased global warming, which in turn results in the rapid melting of glaciers, rising sea levels, ect.[1] The use of these current sources have also had a negative impact on the worldwide economy.[1] As a result, significant research has gone into the discovery of alternate sources of energy, one of the most common being solar energy.[1] Photovoltaic solar cells, which operate by photovoltaics, have emerged as a leading candidate in the search for renewable energy sources as a result of their ability to produce an adequate amount of energy for human use.[1] Photovoltaics involves the conversion of light into electricity; hence in the case of solar cells, sunlight is absorbed and converted into energy via photovoltaics.

Solar cells consist of two semiconducting layers, an n-type where the negative charges dominate (i.e. electrons), such as silicon doped with phosphorus, and a p-type where the positive charges dominate, such as silicon doped with boron, separated by an interface known as a junction. The semiconducting layers consist of a lower-level valence band and a higher-level conduction band, separated by a bandgap of particular energy, as shown in Figure 1.1.[2]

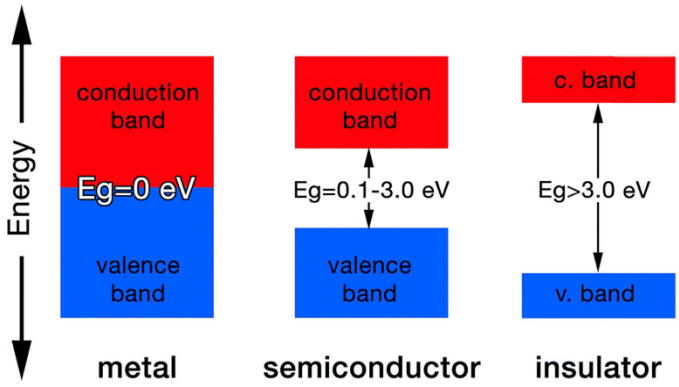

Figure 1.1. Diagram of the bandgap in a metal, semiconductor, and insulator.[2]

Upon absorption of sufficient energy equivalent to the bandgap, the electrons in the valence band are able to transfer to the conduction band, thus allowing them to conduct electricity. In terms of single-junction solar cells the efficiency limit, given the optimal bandgap, is widely known as the Shockley-Queisser limit.[3,4] This limit was first theorized by William Shockley and Hans Queisser in 1961, with their calculations determining that the maximum efficiency of a single-junction solar cell was limited to around 30% with a bandgap of 1.1 eV using a sun temperature of 6000 K and a cell temperature of 300 K.[4] It has also been determined that illumination via the AM 1.5G spectrum, the standard spectral irradiance spectrum, leads to a maximum efficiency of about 33.7% (bandgap of around 1.34 eV).[5,6]

Silicon is the most commonly used material in solar cell fabrication, however the production and disposal of Silicon-based solar cells often have highly negative effects on both the environment and public health.[7] The production often requires the purification of silane (SiH_4), which is highly toxic, and phosphine and diborane are often used to dope the silicon, both of which are also highly toxic.[7] As a result, other semiconducting materials have been studied for use in solar cells, such as perovskites, with applications in solar cell fabrication steadily increasing over the years. In particular, perovskite solar cells have shown significant improvement in their efficiencies,

reaching a record 25.2% as of July 2020, which is also very close to the record efficiency of 26.7% for c-Si solar cells.[8] The power conversion efficiencies of the best performing perovskite solar cells can be seen in Figure 1.2.[9]

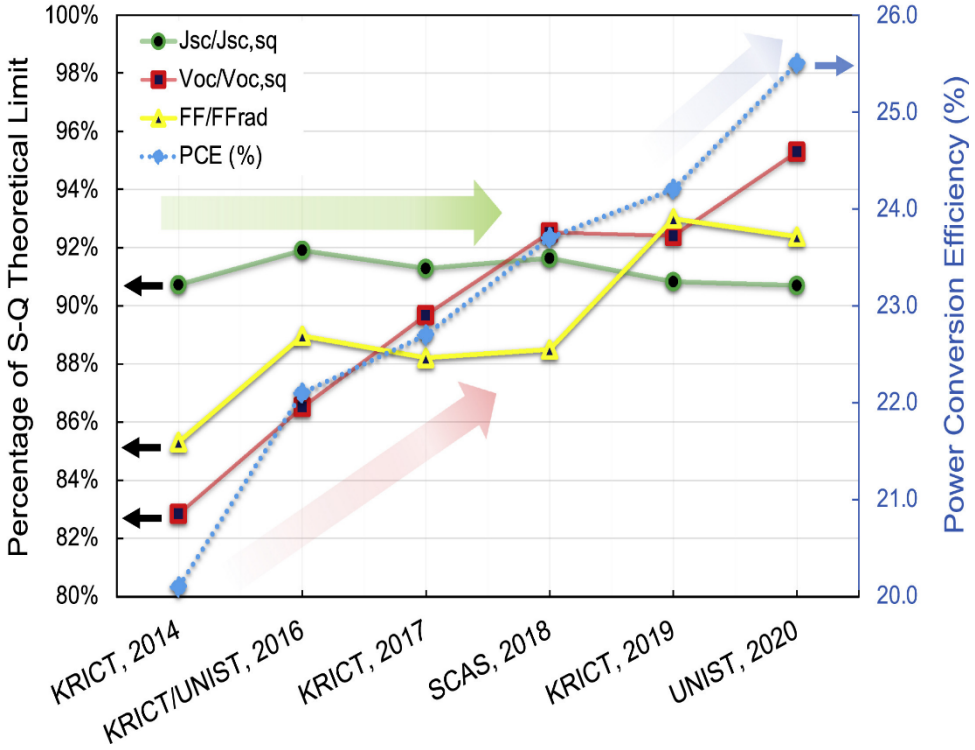

Figure 1.2. Efficiencies of the best performing single junction perovskite solar cells as of 2020.[9]

In addition to applications in the field of solar cell fabrication, perovskites, especially in the form of metal halide perovskites (MHPs), have also been used in Light Emitting Diodes (LEDs), Field Effect Transistors (FETs), lasers, photodetectors, and hard radiation detectors.[10,11] MHPs, first studied by Weber et al. in 1978, have been the most common type of perovskite used in such applications for several years.[10,11] MHPs have also been proven to work effectively in both energy storage, in particular batteries and supercapacitors, and conversion devices.[10] MHPs have been used in lithium ion batteries, however this is a field that still requires serious improvement.[10] MHPs have also been extensively studied in supercapacitors due to their electronic and ionic conduction characteristics, thus allowing them to act as the electrode in the supercapacitor.[10]

1.2 Structures of Perovskite

Perovskite, named after Lev Perovski, was first discovered as a calcium titanium oxide mineral ($CaTiO_3$) within a piece of skarn rock in 1839 by Prussian minerologist Gustav Rose.[12,13] Since its discovery, the crystal structure has been utilized in various other compounds over the years. Perovskite compounds typically exist as an ABX_3 structure (3D perovskites), similar to the structure of $CaTiO_3$, where A is typically a cation, B a divalent cation, and X an anion.[13] The three common crystalline phases of the typical ABX_3 perovskite include cubic, tetragonal, and orthorhombic, as shown in Figure 1.3.[1, 13]

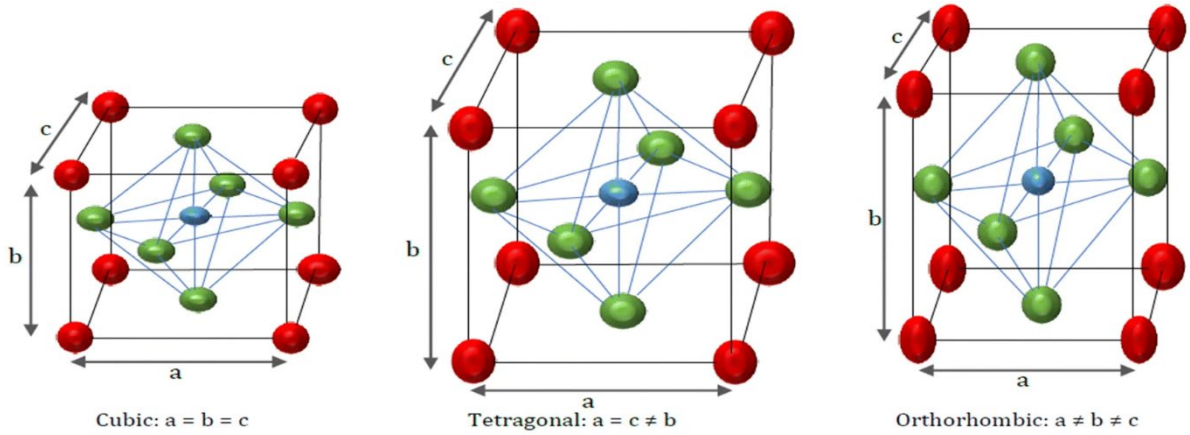

Figure 1.3. Three common crystalline phases of ABX_3 perovskite, where red balls are A, blue balls are B, and green balls are X.[1]

For a crystal to be identified as a perovskite, it must adhere to two unique factors, the tolerance factor and the octahedral factor, both first proposed by Victor Goldschmidt in 1926, and are often used to identify stability.[1] The tolerance factor, t, can be described as the ratio between the distances between the A and X sites and the B and X sites, as shown in Equation 1.1, where R_A, R_B, and R_X are the ionic radii of A, B, and X, respectively, where R_A is always greater than R_B, and a typical value of 0.7-1.11 means the crystal can be identified as a perovskite.[1,14]

$$t = \frac{R_A + R_X}{\sqrt{2}(R_B + R_X)} \tag{1.1}$$

The octahedral factor, μ, is the ratio between R_B and R_X, as shown in Equation 1.2, with a value of 0.44-0.90 being the ideal crystal structure.[1]

$$\mu = \frac{R_B}{R_X} \tag{1.2}$$

The material must have tolerance and octahedral factors that fall within the ideal ranges for it to operate as a perovskite in applications such as solar cells, materials with values out of the ideal range will degrade much faster, thus disrupting the cell.[1]

Additionally, non-cubic perovskites have been known to exhibit the piezoelectric effect, which is the ability of a crystal to generate an electrical charge in response to applied mechanical stress. In particular, the external stress results in the atoms in the unit cell shifting with respect to each other, with a shift in certain directions resulting in polarization.[15] Given that perovskites are semiconducting materials, the electrical charge created upon the application of stress can be correlated with the electrical conductivity achieved upon the excitation of the electrons from the valence band to the conduction band upon the absorption of energy equivalent to the bandgap. Furthermore, perovskites, specifically hybrid perovskites, are also known to exhibit piezochromism, which is the ability of a material to change colour upon the application of pressure and is closely related to the electronic bandgap change.

Over the years a transition from fully inorganic to hybrid perovskites, known as hybrid organic-inorganic perovskites (HOIPs), formed from combinations of organic and inorganic materials, has witnessed a major influx of research. In 2009, Kojima et al. successfully developed a perovskite

solar cells from methyl ammonium (MA) lead iodide ($CH_3NH_3PbI_3$) and methyl ammonium lead bromide ($CH_3NH_3PbBr_3$) nanocrystals, as n-type semiconductors, self-assembled on a TiO_2 surface, with power conversion efficiencies of 3.8% and 3.1%, respectively.[16] This was the first significant report of hybrid perovskites, and the efficiency of the $CH_3NH_3PbI_3$ cell was further improved to 9.7% by Kim et al. in 2012.[17]

Unfortunately, 3D HOIPs suffer from some serious drawbacks, such as stability concerns, restricted chemicals for composition, and use of toxic chemicals, that tend to limit their utilization in optoelectronic applications.[11,18-19] In the ABX_3 structure, A is typically Cs^+, $CH_3NH_3^+$ (MA), or $[HC(NH_2)_2]^+$ (FA), B is Pb^{2+}, Ge^{2+}, or Sn^{2+}, and X is Cl^-, Br^-, or I^-.[11] However, only 3 A-site cations in regards to the 3D type are capable of maintaining the ideal corner-sharing octahedral network (Cs^+, MA, and FA).[18] Furthermore, 3D HOIPs also tend to use more volatile and toxic cations, whilst also suffering from further stability issues due to humidity and light.[19] The instability of 3D HOIPs in the presence of humidity and water is believed to be a result of their low formation energy.[20] Further toxicity issues arise due to the high toxicity of lead, which is also highly water soluble.[21] Cesium-based perovskites, where Cesium replaces the A-site organic cations, have been shown to improve stability and efficiency.[1] The stability, structural, and composition concerns of 3D perovskites are often significantly lowered by switching to 2D perovskites.

1.3 2D Hybrid Organic-Inorganic Perovskites

2D HOIPs have become popular materials for solar cell development with the efficiency of 2D HOIP solar cells jumping from 4.7% in 2014 to 18.2% by 2018.[19] Additionally, 2D HOIPs also have certain advantages over their 3D counterparts, in that they much more stable against humidity

and light, they are generally able to use larger and less volatile (usually hydrophobic) organic cations, thus enhancing both the chemical and thermal stability, they are much more durable, have greater chemical versatility, and have greater processability.[19] The octahedral connectivity mode is a major factor in determining stability in 2D HOIPs, as seen in Figure 1.4.[11] The three modes that have been observed include corner-sharing (sharing of a corner), edge-sharing (sharing of an edge), and face-sharing (sharing of a face).[11] The best stability is provided by the corner-sharing octahedral network as it lowers the bandgap, with 2D perovskites more capable of achieving this network, making them ideal for optoelectronic applications.[11]

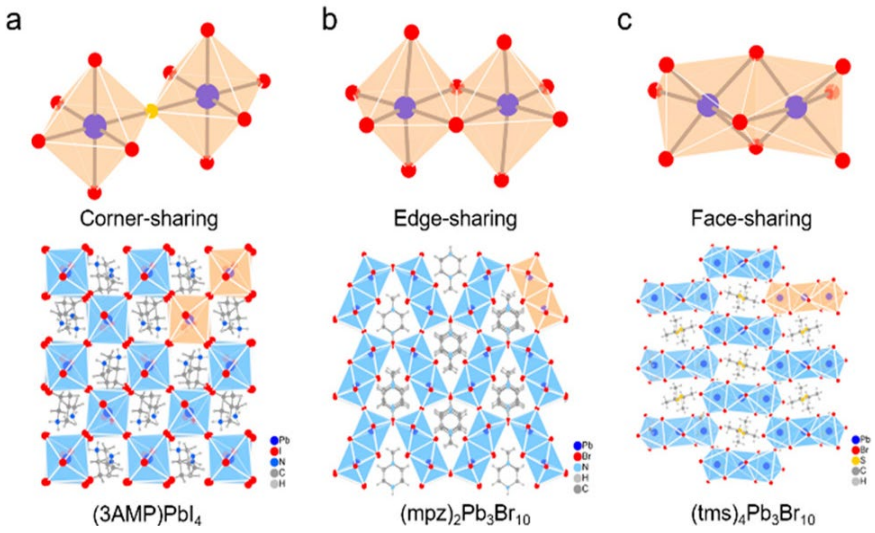

Figure 1.4. Octahedral Connectivity Modes in 2D Perovskites and examples, where (a) is corner-sharing, (b) is edge-sharing, and (c) is face-sharing.[11]

The impact of 2D HOIPs in applications such as solar cells, has steadily increased over the years.[22] One major reason for this is that 2D HOIPs are much simpler in structure and reducing from 3D to 2D allows for both improving the optoelectronic properties and access to various hybrid organic-inorganic materials.[11] 2D perovskites typically consist of metal halide octahedra situated in between two adjacent organic cation layers.[22] The organic layers typically act as insulating

barriers, restricting the charge carriers to 2D.[11] 2D HOIPs have a $(A')_m A_{n-1} B_n X_{3n+1}$ formula, as seen in Figure 1.5, where A', the organic spacer, can be either monovalent (m = 1) or divalent (m = 2), and n is the number of metal halide octahedra.[11,22]

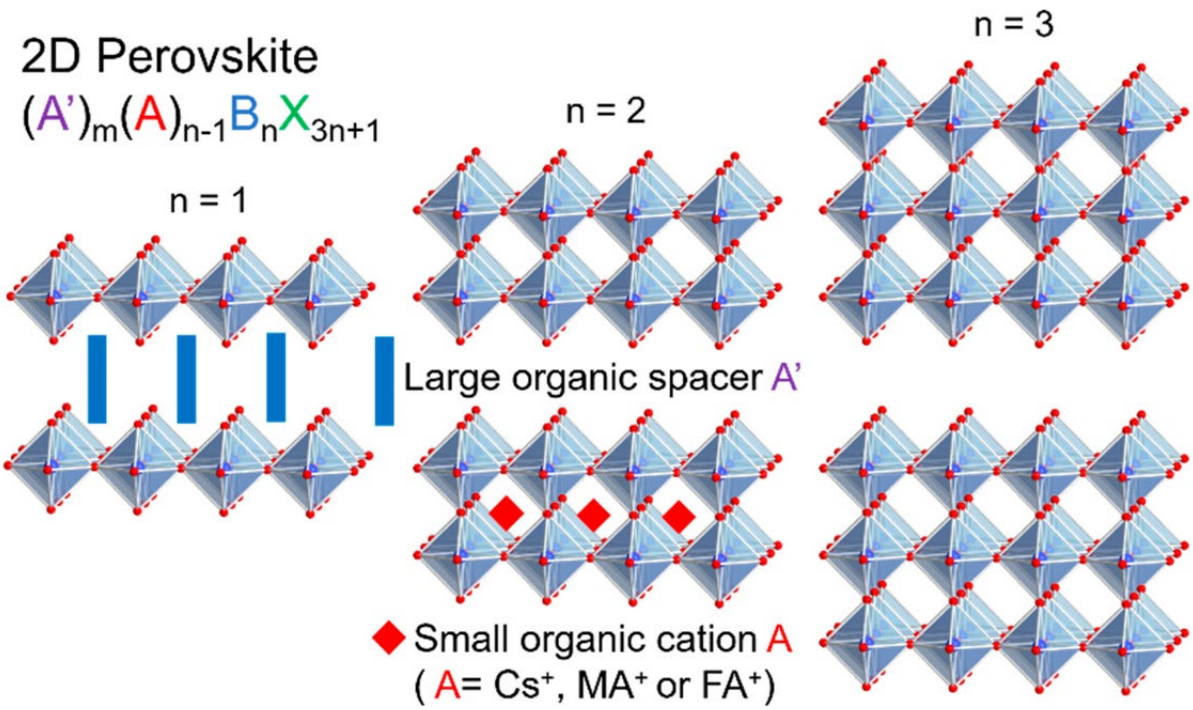

Figure 1.5. 2D HOIP structures for n = 1, n = 2, and n = 3, where A' is the organic spacer, A is the organic cation, B is the metal, and X is the halide.[11]

2D perovskites typically consist of layers that are obtained by making cuts along the crystallographic planes of the corresponding 3D perovskite, with the 3 most common orientations being the <100>, <110>, and <111> (i.e. cut along the <100>, <110>, or <111> plane).[19] The most common type of 2D halide perovskite for solar cell applications is the <100>-oriented one, which can further be classified into two further types, Ruddlesden-Popper (RP) and Dion-Jacobson (DJ) perovskites.[19,23] Hybrid RP perovskites stem from inorganic perovskites such as $Sr_3Ti_2O_7$, first synthesized and studied in 1957 by Ruddlesden and Popper.[19,24] RP perovskites are derived from the 3D structure by cutting inorganic layers of varying n value along the <100> plane, and placing them between bulky ammonium cation bilayers, whereas DJ perovskites are derived by cutting

inorganic layers from the 3D structure that stack directly on top of each other.[19] A major advantage of RP perovskites is the superior ability to control the n value (thickness), which is a highly valuable property in regards to photovoltaic applications, thus making them the most commonly studied 2D perovskite for solar cell applications.[19] Both RP and DJ perovskites typically have a $(A')_2A_{n-1}B_nX_{3n+1}$ formula, where A' for the RP phase is an ammonium cation (RNH_3), typically of alkyl or aryl type, such as butylammonium (BA) or phenylethylammonium (PEA).[19,25]

In 2D perovskites, the semiconducting inorganic octahedra in between the organic spacers allows for a 2D multiple quantum well (MQW) electronic structure, which forms from a natural bottom-up self-assembly, and where the wells are the perovskite layers and the barriers are the insulating organic spacers.[11,26] The organic spacer insulating barriers help restrict the charge carriers to 2D and the 2D MQWs help stabilize excitons, which can be observed at ambient temperatures.[11] In general, the length of the A' organic spacer dictates the width of the barrier, while the well width can vary depending on the value of n (i.e. the layer thickness or number of metal-halide octahedra).[26] The typical structure of this 2D MQW is shown in Figure 1.6.

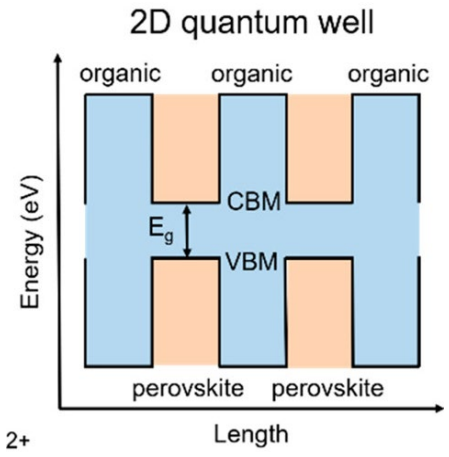

Figure 1.6. Structure of 2D Multiple Quantum Well.[11]

The presence of the bandgap often leads to the formation of excitons in 2D HOIPs.[27] 2D HOIPs experience both quantum and dielectric confinement, mainly due to the difference in permittivity between the inorganic layer and the bulky organic cation.[27] These confinements lead to increased correlations between the electrons and the electron holes, thus increasing the exciton binding energy (E_b) in 2D HOIPs compared to their 3D counterparts from tens of meV in $CH_3NH_3PbI_3$ to hundreds of meV.[27] The excitonic emission is often governed by the spacing between layers, which varies depending on the choice of the organic spacer (A').[11] In the RP phase, the presence of the bulky spacer bilayers leads to increased separation between the inorganic layers (around 1.5 times the length of the organic spacer), ultimately leading to no perovskite-perovskite interactions, which in turn results in an excitonic emission that depends solely on the spatial electronic confinement of the layers.[11] By contrast, in the DJ phase the inorganic layers are much closer together due to the stacking conformation, which produces weak perovskite-perovskite interactions, leading to an exciton energy redshift.[11]

There are many factors which influence the bandgap of 2D HOIPs, two of the most common being quantum and dielectric confinement.[11] In the case of lead halide perovskites (LHPs), quantum confinement present in 2D LHPs leads to greater exciton binding energies (190-400 meV for pure 2D LHPs) and bandgaps compared to their 3D counterparts.[28] The bandgap can also be effected by the dimensionality, where the lower the n value, the greater the bandgap, as seen in $(BA)_2(MA)_{n-1}Pb_nI_{3n+1}$ where the bandgap decreases from 2.35 eV for n = 1 to 1.6 eV for n = ∞ (i.e. the 3D case).[11] As the spacing between the inorganic layers has a major impact on the exciton emission, they also impact the bandgap where the greater the spacing, the greater the bandgap, meaning RP perovskites have greater bandgaps compared to DJ perovskites.[11] The bandgap can

also be affected by the metal-halide bond angle, where the greater the angle, the lower the bandgap, as a result of increased structural distortion.[11] Increasing the value of n leads to a further class of 2D HOIPs, namely high n-2D HOIPs.[22]

1.4 High n-2D Hybrid Organic-Inorganic Perovskites (n=2-5)

2D HOIPs can be separated into two classes based on the n value, n = 1 2D HOIPs which only have one metal halide octahedra, while high n-2D HOIPs often consist of greater n values (i.e. greater metal halide octahedra), typically values between 2-5.[22] In 1991 Calabrese et al. proved that for the RP phase, 2D (n = 1) and 3D perovskites were extreme cases by synthesizing n = 2 2D lead perovskite crystals, such as $(Me(CH_2)_8NH_3)_2Pb_2I_7$.[29] As discussed previously, varying the value of n allows for tuning of the bandgap, due to increasing quantum confinement, and it is this ability and the structural versatility that makes high n-2D HOIPs such a vigorously studied material class in regards to optoelectronic applications.[22] However, it has been shown that due to the similarity in structure between high n 2D HOIPs and 3D HOIPs, for n > 5, pure crystals and films are often difficult to synthesize.[22] Several studies have been done on high n-2D perovskites and the tuning of the bandgap through changing n. $(BA)_2(MA)_{n-1}Pb_nI_{3n+1}$ was studied by Stoumpos et al. at various n values with the bandgap decreasing as n increased.[30-31] Cao et al. also showed further tuning of the bandgap by switching the metal from Pb to Sn.[32]

In comparison to n = 1 2D HOIPs, for higher n-2D HOIPs the crystal orientation and phase distribution are significantly different.[22] Whilst the synthesis of pure high n-2D HOIP crystals is possible, films deposited via solution methods often contain various phases with varying n values.[22] For example, synthesized n = 4 2D HOIP films might also contain n = 1-5 2D HOIP

phases as well as 3D HOIP phases, with these often referred to as mixed states.[22] In regards to how the different phases are distributed across the thin films, the smaller n phases often dominate the substrate side (i.e. side on which the film is deposited) while the higher n and 3D phases often dominate the air side.[22] Due to the primary charge transport channels being located within the inorganic layers, the crystal orientation of 2D perovskite films is highly important for their performance in optoelectronic devices, with a vertical orientation of the inorganic layers, first achieved via a hot-casting method by Tsai et al., desirable for use in solar cells.[22,33] Increased efficiency has also been reported for high n-2D HOIP solar cells.[33-34]

High n-2D HOIPs exhibit several advantages in comparison to 3D and low n-2D HOIPs. It is understood that a major factor detrimental to the performance of solar cells is trap states, specifically charge carrier trapping.[35] These traps can often lead to defects, which are believed to be suppressed in high n-2D HOIPs, in turn leading to a decrease in the level of self-doping and providing incredibly high light detectivity of the photodetector.[36] High n-2D HOIPs are also believed to suppress ion migration, which can often lead to increased degradation of 3D perovskite solar cells.[22] High n-2D HOIPs have also shown to exhibit enhanced stability compared to their 3D counterparts, which is a major advantage in solar cell fabrication.[22] In particular, 3D perovskites like $MAPbI_3$ are unstable in the presence of moisture.[21] High n-2D HOIPs have exhibited enhanced stability in the presence of moisture and allow for device fabrication under humid conditions.[21,37] The improved stability under humid conditions is a result of the greater formation energies of low dimensional perovskites due to greater van der Waals interactions.[20]

1.5 Effects of High Pressure on 2D Hybrid Organic-Inorganic Perovskites

The application of high external pressure has been shown to result in modifications towards both the structural (i.e. phase transitions) and optoelectronic (i.e. bandgap tuning) properties of 2D HOIPs.[38-39, 40] The use of high external pressure is a clean and powerful method for tuning the optoelectronic properties of 2D HOIPs.[39,41] The primary experimental techniques used for analyzing the structural properties and pressure-induced phase transitions are Raman Spectroscopy, Fourier-Transform Infrared (FTIR) Spectroscopy, and X-ray Diffraction (XRD). The primary techniques for analyzing the optoelectronic properties include UV-Visible Absorption Spectroscopy (UV-Vis) and Photoluminescence (PL). Numerous high-pressure studies have been conducted, particularly on lead-iodide 2D HOIPs, to examine and understand its effects on the structural and optoelectronic properties. The observed bandgap transitions of such studies are summarized in Table 1.1.

Table 1.1. Bandgap transitions of high-pressure studies on lead-iodide 2D HOIPs

Organic Spacer	Perovskite formula	Bandgap transition (eV)	Pressure of smallest observed bandgap (GPa)	Maximum pressure achieved (GPa)	Experimental methods for characterization	Reference
PDMA	1	N/A	N/A	0.35	XRD, PL, UV-Vis	Muscarella et al.[42]
$(BzA)_2$	$(BzA)_2PbI_4$	N/A	N/A	0.35	XRD, PL, UV-Vis	Muscarella et al.[42]
$(PMA)_2$	$(PMA)_2PbI_4$	2.15-1.26	20.1	27.2	XRD, FTIR, UV-Vis	Tian et al.[41]
$(PEA)_2$	$(PEA)_2PbI_4$	2.26-1.83	5.8	10	XRD, PL, TRPL, UV-Vis	Gao et al.[43]
$(BA)_2$	$(BA)_2PbI_4$	1.97-1.7	5.3	10	XRD, PL, TRPL, Raman, UV-Vis	Yin et al.[44]
$(BA)_2$	$(BA)_2PbI_4$	2.28-0.95	35	40	XRD, PL, TRPL, UV-Vis	Yuan et al.[45]
$(BA)_2$	$(BA)_2PbI_4$	2.29-1.78	6.7	28.2	XRD, UV-Vis	Liu et al.[46]
$(BA)_2$	$(BA)_2(MA)_2Pb_3I_{10}$	1.94-1.79	1.9	26	XRD, UV-Vis	Liu et al.[46]
$(BA)_2$	$(BA)_2(MA)_3Pb_4I_{13}$	1.81-1.72	1.5	26	XRD, UV-Vis	Liu et al.[46]
$(ETA)_2$	$(ETA)_2PbI_4$	2.24-1.85	8.0	20.2	XRD, PL, Raman, UV-Vis	Fang et al.[47]
$(Gua)_2$	$(Gua)_2PbI_4$	2.55-2.32	5.5	13.8	Raman, UV-Vis, PL	Li et al.[48]
3AMP	$(3AMP)PbI_4$	2.10-1.63	20.1	134	XRD, FTIR, PL, UV-Vis,	Kong et al.[49]
3AMP	$(3AMP)(MA)Pb_2I_7$	1.85-1.78	20.3	72.2	XRD, FTIR, PL, UV-Vis,	Kong et al.[49]
3AMP	$(3AMP)(MA)_3Pb_4I_{13}$	1.74-1.52	22.1	76.6	XRD, FTIR, PL, UV-Vis,	Kong et al.[49]

The properties and band structure are often governed by the bond angle and bond length of the inorganic lattice, thus making them the key in regards to tuning the bandgap under high pressure.[50] Distortion of the crystal lattice is observed depending on the direction the external pressure is applied in, which in turn leads to octahedral tilting and shortening of the bond angle.[11] The buffer-

acting organic layers help to relieve the excess stress.[11] Structural changes can be observed upon compression, such as in lead-iodide 2D HOIPs where the change is a result of the narrowing of the Pb-I-Pb bond angle and the shortening of the Pb-I bond length, as seen in Figure 1.7.[46] The narrowing of the Pb-I-Pb bond angle leads to an increase in the bandgap, whilst the shortening of the Pb-I bond length leads to bandgap narrowing.[41,46]

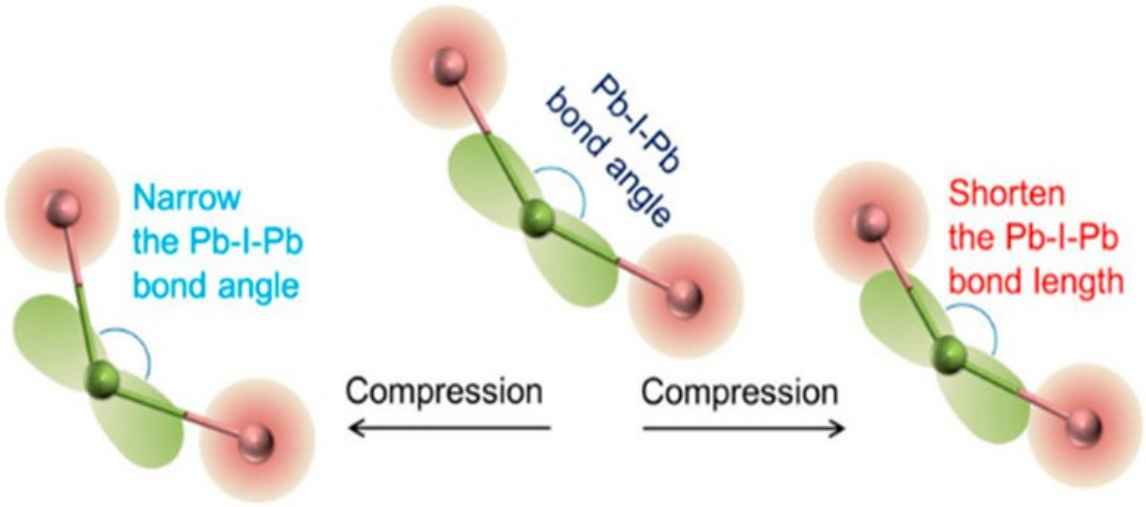

Figure 1.7. Effect of external pressure on Pb-I-Pb bond angle and Pb-I bond length.[46]

The interaction between the organic and inorganic layers of 2D HOIPs are governed by the H-X hydrogen bonding, where X is the halide anion.[41] In the case of lead-iodide 2D HOIPs, the hydrogen bonding occurs between the hydrogen of the NH_3^+ group and the I^- anions.[41] It has been shown that the application of external high pressure induces an enhancement of the hydrogen bonding, which in turn leads to the shortening of the Pb-I bond length and the subsequent narrowing of the bandgap.[41]

The bandgap is often governed by the alteration of the valence band maximum (VBM) and the conduction band minimum (CBM).[41] In Pb-I 2D HOIPs, different spacers can lead to different

VBM and CBM compositions and thus varying interactions. For example, in $(PMA)_2PbI_4$ the VBM is characterized by strong hybridization induced by antibonding interactions between the Pb 6s and I 5p orbitals in the $[PbI_6]^{2-}$ octahedral network, while the CBM is characterized by hybridization induced by Pb 6p and I 5p antibonding interactions.[41] For the VBM the major contribution comes from the I 5p orbital, and for the CBM the major contribution comes from the Pb 6p orbital.[41] The change in the bandgap is thought to originate from the VBM as the Pb 6p orbital is less sensitive to external pressure.[41] On the other hand, in $(ETA)_2PbI_4$ the main contribution for the VBM comes from the Pb 6s states, with some contribution from the I 5p states, while the main contribution for the CBM comes from the Pb 6p states, with some contribution from the I 5s states.[47]

Along with tuning of the bandgap, the application of high external pressure has also been shown to induce structural changes, most notably phase transitions, in 2D HOIPs.[38,40, 51] Observed phase transitions of high pressure studies on lead-iodide 2D HOIPs are summarized in Table 1.2.

Table 1.2. Phase transitions of high-pressure studies on lead-iodide 2D HOIPs
[a] Same crystal structure and space group as (b), but different *a* and *b* axis

Organic Spacer	Perovskite formula	Crystal structure, Space group	Observed phase transition	Pressure to achieve transition (GPa)	Reference
$(BA)_2$	$(BA)_2PbI_4$	Orthorhombic, *Pbca*	Orthorhombic *Pbca* → Triclinic $P\bar{1}$	1.12	Azeem et al.[52]
$(BzA)_2$	$(BzA)_2PbI_4$	Orthorhombic, *Pbca*	N/A	N/A	Muscarella et al.[42]
PDMA	$(PDMA)PbI_4$	Monoclinic, $P2_1/c$	N/A	N/A	Muscarella et al.[42]
$(PMA)_2$	$(PMA)_2PbI_4$	Orthorhombic, *Pbca*	Orthorhombic *Pbca* → Orthorhombic *Pccn*	4.6	Tian et al.[41]
$(BA)_2$	$(BA)_2PbI_4$	Orthorhombic, *Pbca*	(1) Orthorhombic *Pbca* (b) → Orthorhombic *Pbca* (a)[a] (2) Orthorhombic *Pbca* (a) → Monoclinic $P2_1/a$	(1) 0.1 (2) 1.6	Yin et al.[44]
$(Gua)_2$	$(Gua)_2PbI_4$	N/A	N/A	5.5	Li et al.[48]

In the case of lead-iodide 2D HOIPs, the phase transitions are often in correlation with the observed bandgap transitions.[41,45,52] Phase transitions are governed by the tilting and distortion of the PbI_6 octahedral network, which is also the result of changes to the Pb-I-Pb bond angle.[39] [52] Upon compression, the common pathways to induce inorganic lattice can relaxing include octahedral tilting and bond shortening, with octahedral tilting dominating at low pressures (typically < 5 GPa).[39] For example, the compression of $(BA)_2PbI_4$ results in a reduction of volume due to the

shortening of the Pb-I bond, thus resulting in a photoluminescence redshift, as observed by Azeem et al.[52]

Another key effect of applying 2D HOIPs to high external pressure is the amorphization of the material. Amorphization is the process where, under compression, the unique crystalline properties of the perovskite material are lost.[53] It is also important to note whether the such processes (compression, phase transition, amorphization) are reversible or irreversible. For example, Zhan et al. observed in their high-pressure study of $(PMA)_2CuBr_4$ that the compression process below 40 GPa was indeed reversible, due to the consistency of the Raman peaks, along with an observed irreversible pressure-induced amorphization process, due to the broadening of the Raman peaks.[54]

1.6 Thesis Objectives and Outline

The purpose of this thesis is to communicate the effects of high-pressure on the structures and optoelectronic properties of $DPDAPbI_4$, $CMA_2MAPb_2I_7$, and $CMA_2FAPb_2I_7$. 2D HOIPs were selected as a result of their enhanced stability in comparison to their 3D counterparts and the increased diversity of the organic spacer cations that can be used, thus allowing for more diverse properties.[11, 19] $DPDAPbI_4$ was selected due to the high rigidity of the DPDA spacer, believed to be at the limit for accepted rigidity in 2D perovskites.[55] $CMA_2MAPb_2I_7$ and $CMA_2FAPb_2I_7$ were selected due to the lower bandgaps of high-n CMA-based perovskites, thus decreasing the overall reduction required to achieve the desired Shockley-Queisser limit.[56,57]

This study represents the first time $DPDAPbI_4$, $CMA_2MAPb_2I_7$, and $CMA_2FAPb_2I_7$ have all been probed by HP through both experimental and computational methods. As reaching the Shockley-

Queisser limit is crucial for solar cell applications, the main objective is to permanently alter the bandgap using HP to achieve this limit. An increase in the photoluminescence intensity upon compression is also desirable for solar cell applications, as well as for other applications including light-emitting diodes. The insights and findings from this study not only help to understand and predict how similar 2D HOIPs may behave at HP, but they also help provide a basis for the design of future 2D HOIPs for practical applications. The results and findings of this study build upon previous studies conducted on the compounds of interest, in particular the results of $DPDAPbI_4$ build upon the previous temperature-based study by Hautzinger et al.[55] Vibrational spectroscopy, namely Raman and FTIR, and XRD measurements were used to examine the structural modifications. The excitonic behavior was examined using PL measurements and the bandgap behavior was examined through UV-Visible absorption.

This thesis comprises a total of 5 chapters, where chapter 2 discusses the theoretical background required for the study along with the experimental techniques used. Chapter 3 discusses the experimental findings of $DPDAPbI_4$ while chapter 4 highlights the findings of both $CMA_2MAPb_2I_7$ $CMA_2FAPb_2I_7$. Chapter 5 discusses the overall conclusions of this work along with the future work stemming from the results obtained in this study.

1.7 References

(1) Jerpoth, S. S.; Iannello, J.; Aboagye, E. A.; Yenkie, K. M. Computer-aided synthesis of cost-effective perovskite crystals: an emerging alternative to silicon solar cells. *Clean Technologies and Environmental Policy* **2020**, *22* (5), 1187-1198.

(2) Morab, S.; Sundaram, M. M.; Pivrikas, A. Review on Charge Carrier Transport in Inorganic and Organic Semiconductors. In *Coatings*, 2023; Vol. 13.

(3) Xu, Y.; Gong, T.; Munday, J. N. The generalized Shockley-Queisser limit for nanostructured solar cells. *Scientific Reports* **2015**, *5* (1), 13536.

(4) Shockley, W. and Queisser, H. J. Detailed Balance Limit of Efficiency of p-n Junction Solar Cells. *Journal of Applied Physics* **1961**, *32* (3), 510-519.

(5) Wang, K.; Zheng, L.; Hou, Y.; Nozariasbmarz, A.; Poudel, B.; Yoon, J.; Ye, T.; Yang, D.; Pogrebnyakov, A. V.; Gopalan, V.; Priya, S. Overcoming Shockley-Queisser limit using halide perovskite platform? *Joule* **2022**, *6* (4), 756-771.

(6) Rühle, S. Tabulated values of the Shockley–Queisser limit for single junction solar cells. *Solar Energy* **2016**, *130*, 139-147.

(7) Dubey, S.; Jadhav, N. Y.; Zakirova, B. Socio-Economic and Environmental Impacts of Silicon Based Photovoltaic (PV) Technologies. *Energy Procedia* **2013**, *33*, 322-334.

(8) Ehrler, B.; Alarcón-Lladó, E.; Tabernig, S. W.; Veeken, T.; Garnett, E. C.; Polman, A. Photovoltaics Reaching for the Shockley–Queisser Limit. *ACS Energy Letters* **2020**, *5* (9), 3029-3033.

(9) Liao, J. H.-H. Behind the Breakthrough of the ~30% Perovskite Solar Cell. *Joule* **2021**, *5* (2), 295-297.

(10) Narayanan, S.; Parikh, N.; Tavakoli, M. M.; Pandey, M.; Kumar, M.; Kalam, A.; Trivedi, S.; Prochowicz, D.; Yadav, P. Metal Halide Perovskites for Energy Storage Applications. *European Journal of Inorganic Chemistry* **2021**, *2021* (13), 1201-1212.

(11) Mao, L.; Stoumpos, C. C.; Kanatzidis, M. G. Two-Dimensional Hybrid Halide Perovskites: Principles and Promises. *Journal of the American Chemical Society* **2019**, *141* (3), 1171-1190.

(12) Chakhmouradian, A. R. and Woodward, P. M. Celebrating 175 years of perovskite research: a tribute to Roger H. Mitchell. *Physics and Chemistry of Minerals* **2014**, *41* (6), 387-391.

(13) Wei, L.; Yang, L.; Ju, W.; Cuncun, W.; Congyue, L.; Lixin, X.; Zhijian, C.; Shufeng, W.; Qihuang, G. Twin Domains in Organometallic Halide Perovskite Thin-Films. *Crystals* **2018**, *8* (5).

(14) Jena, A. K.; Kulkarni, A.; Miyasaka, T. Halide Perovskite Photovoltaics: Background, Status, and Future Prospects. *Chemical Reviews* **2019**, *119* (5), 3036-3103.

(15) Grundmann, M. *The Physics of Semiconductors: An Introduction Including Nanophysics and Applications*; Springer International Publishing, **2016**.

(16) Kojima, A.; Teshima, K.; Shirai, Y.; Miyasaka, T. Organometal Halide Perovskites as Visible-Light Sensitizers for Photovoltaic Cells. *Journal of the American Chemical Society* **2009**, *131* (17), 6050-6051.

(17) Kim, H.-S.; Lee, C.-R.; Im, J.-H.; Lee, K.-B.; Moehl, T.; Marchioro, A.; Moon, S.-J.; Humphry-Baker, R.; Yum, J.-H.; Moser, J. E.; Grätzel, M; Park, N.-G. Lead Iodide Perovskite Sensitized All-Solid-State Submicron Thin Film Mesoscopic Solar Cell with Efficiency Exceeding 9%. *Scientific Reports* **2012**, *2* (1), 591.

(18) Stoumpos, C. C. and Kanatzidis, M. G. The Renaissance of Halide Perovskites and Their Evolution as Emerging Semiconductors. *Accounts of Chemical Research* **2015**, *48* (10), 2791-2802.

(19) Ortiz-Cervantes, C.; Carmona-Monroy, P.; Solis-Ibarra, D. Two-Dimensional Halide Perovskites in Solar Cells: 2D or not 2D? *ChemSusChem* **2019**, *12* (8), 1560-1575.

(20) Quan, L. N.; Yuan, M.; Comin, R.; Voznyy, O.; Beauregard, E. M.; Hoogland, S.; Buin, A.; Kirmani, A. R.; Zhao, K.; Amassian, A.; Kim, D. H.; Sargent, E. H. Ligand-Stabilized Reduced-Dimensionality Perovskites. *Journal of the American Chemical Society* **2016**, *138* (8), 2649-2655.

(21) Smith, I. C.; Hoke, E. T.; Solis-Ibarra, D.; McGehee, M. D.; Karunadasa, H. I. A Layered Hybrid Perovskite Solar-Cell Absorber with Enhanced Moisture Stability. *Angewandte Chemie International Edition* **2014**, *53* (42), 11232-11235.

(22) Hu, J.; Yan, L.; You, W. Two-Dimensional Organic–Inorganic Hybrid Perovskites: A New Platform for Optoelectronic Applications. *Advanced Materials* **2018**, *30* (48), 1802041.

(23) Mao, L.; Ke, W.; Pedesseau, L.; Wu, Y.; Katan, C.; Even, J.; Wasielewski, M. R.; Stoumpos, C. C.; Kanatzidis, M. G. Hybrid Dion–Jacobson 2D Lead Iodide Perovskites. *Journal of the American Chemical Society* **2018**, *140* (10), 3775-3783.

(24) Ruddlesden, S. N. and Popper, P. The compound $Sr_3Ti_2O_7$ and its structure. *Acta Crystallographica* **1958**, *11* (1), 54-55.

(25) Saparov, B.; Mitzi, D. B. Organic–Inorganic Perovskites: Structural Versatility for Functional Materials Design. *Chemical Reviews* **2016**, *116* (7), 4558-4596.

(26) Soe, C. M. M.; Nagabhushana, G. P.; Shivaramaiah, R.; Tsai, H.; Nie, W.; Blancon, J.-C.; Melkonyan, F.; Cao, D. H.; Traoré, B.; Pedesseau, L.; Kepenekian, M.; Katan, C.; Even, J.; Marks, T. J.; Navrotsky, A.; Mohite, A. D.; Stoumpos, C. C.; Kanatzidis, M. G. Structural and

thermodynamic limits of layer thickness in 2D halide perovskites. *Proceedings of the National Academy of Sciences* **2019**, *116* (1), 58-66.

(27) Burgos-Caminal, A.; Socie, E.; Bouduban, M. E. F.; Moser, J.-E. Exciton and Carrier Dynamics in Two-Dimensional Perovskites. *The Journal of Physical Chemistry Letters* **2020**, *11* (18), 7692-7701.

(28) Hoye, R. L. Z.; Hidalgo, J.; Jagt, R. A.; Correa-Baena, J.-P.; Fix, T.; MacManus-Driscoll, J. L. The Role of Dimensionality on the Optoelectronic Properties of Oxide and Halide Perovskites, and their Halide Derivatives. *Advanced Energy Materials* **2022**, *12* (4), 2100499.

(29) Calabrese, J.; Jones, N. L.; Harlow, R. L.; Herron, N.; Thorn, D. L.; Wang, Y. Preparation and characterization of layered lead halide compounds. *Journal of the American Chemical Society* **1991**, *113* (6), 2328-2330.

(30) Stoumpos, C. C.; Cao, D. H.; Clark, D. J.; Young, J.; Rondinelli, J. M.; Jang, J. I.; Hupp, J. T.; Kanatzidis, M. G. Ruddlesden–Popper Hybrid Lead Iodide Perovskite 2D Homologous Semiconductors. *Chemistry of Materials* **2016**, *28* (8), 2852-2867.

(31) Stoumpos, C. C.; Soe, C. M. M.; Tsai, H.; Nie, W.; Blancon, J.-C.; Cao, D. H.; Liu, F.; Traoré, B.; Katan, C.; Even, J.; Mohite, A. D.; Kanatzidis, M. G. High Members of the 2D Ruddlesden-Popper Halide Perovskites: Synthesis, Optical Properties, and Solar Cells of $(CH_3(CH_2)_3NH_3)_2(CH_3NH_3)_4Pb_5I_{16}$. *Chem* **2017**, *2* (3), 427-440.

(32) Cao, D. H.; Stoumpos, C. C.; Yokoyama, T.; Logsdon, J. L.; Song, T.-B.; Farha, O. K.; Wasielewski, M. R.; Hupp, J. T.; Kanatzidis, M. G. Thin Films and Solar Cells Based on Semiconducting Two-Dimensional Ruddlesden–Popper $(CH_3(CH_2)_3NH_3)_2(CH_3NH_3)n-1SnnI3n+1$ Perovskites. *ACS Energy Letters* **2017**, *2* (5), 982-990.

(33) Tsai, H.; Nie, W.; Blancon, J.-C.; Stoumpos, C. C.; Asadpour, R.; Harutyunyan, B.; Neukirch, A. J.; Verduzco, R.; Crochet, J. J.; Tretiak, S.; Pedesseau, L.; Even, J.; Alam, M. A.; Gupta, G.; Lou, J.; Ajayan, P. M.; Bedzyk, M. J.; Kanatzidis, M. G.; Mohite, A. D. High-efficiency two-dimensional Ruddlesden–Popper perovskite solar cells. *Nature* **2016**, *536* (7616), 312-316.

(34) Zhou, N.; Shen, Y.; Li, L.; Tan, S.; Liu, N.; Zheng, G.; Chen, Q.; Zhou, H. Exploration of Crystallization Kinetics in Quasi Two-Dimensional Perovskite and High Performance Solar Cells. *Journal of the American Chemical Society* **2018**, *140* (1), 459-465.

(35) Wu, X.; Trinh, M. T.; Niesner, D.; Zhu, H.; Norman, Z.; Owen, J. S.; Yaffe, O.; Kudisch, B. J.; Zhu, X. Y. Trap States in Lead Iodide Perovskites. *Journal of the American Chemical Society* **2015**, *137* (5), 2089-2096.

(36) Peng, W.; Yin, J.; Ho, K.-T.; Ouellette, O.; De Bastiani, M.; Murali, B.; El Tall, O.; Shen, C.; Miao, X.; Pan, J.; Alarousu, E.; He, J.-H.; Ooi, B. S.; Mohammed, O. F.; Sargent, E.; Bakr, O. M. Ultralow Self-Doping in Two-dimensional Hybrid Perovskite Single Crystals. *Nano Letters* **2017**, *17* (8), 4759-4767.

(37) Cao, D. H.; Stoumpos, C. C.; Farha, O. K.; Hupp, J. T.; Kanatzidis, M. G. 2D Homologous Perovskites as Light-Absorbing Materials for Solar Cell Applications. *Journal of the American Chemical Society* **2015**, *137* (24), 7843-7850.

(38) Lü, X.; Yang, W.; Jia, Q.; Xu, H. Pressure-induced dramatic changes in organic–inorganic halide perovskites. *Chemical Science* **2017**, *8* (10), 6764-6776.

(39) Jaffe, A.; Lin, Y.; Karunadasa, H. I. Halide Perovskites under Pressure: Accessing New Properties through Lattice Compression. *ACS Energy Letters* **2017**, *2* (7), 1549-1555.

(40) Szafrański, M. and Katrusiak, A. Photovoltaic Hybrid Perovskites under Pressure. *The Journal of Physical Chemistry Letters* **2017**, *8* (11), 2496-2506.

(41) Tian, C.; Liang, Y.; Chen, W.; Huang, Y.; Huang, X.; Tian, F.; Yang, X. Hydrogen-bond enhancement triggered structural evolution and band gap engineering of hybrid perovskite $(C_6H_5CH_2NH_3)_2PbI_4$ under high pressure. *Physical Chemistry Chemical Physics* **2020**, *22* (4), 1841-1846.

(42) Muscarella, L. A.; Dučinskas, A.; Dankl, M.; Andrzejewski, M.; Casati, N. P. M.; Rothlisberger, U.; Maier, J.; Graetzel, M.; Ehrler, B.; Milić, J. V. Reversible Pressure-Dependent Mechanochromism of Dion–Jacobson and Ruddlesden–Popper Layered Hybrid Perovskites. *Advanced Materials* **2022**, *34* (17), 2108720.

(43) Gao, C.; Li, R.; Li, Y.; Wang, R.; Wang, M.; Gan, Z.; Bai, L.; Liu, Y.; Zhao, K.; Liu, S. F.; Cheng, Y.; Huang, W. Direct–Indirect Transition of Pressurized Two-Dimensional Halide Perovskite: Role of Benzene Ring Stack Ordering. *The Journal of Physical Chemistry Letters* **2019**, *10* (19), 5687-5693.

(44) Yin, T.; Liu, B.; Yan, J.; Fang, Y.; Chen, M.; Chong, W. K.; Jiang, S.; Kuo, J.-L.; Fang, J.; Liang, P.; Wei, S.; Loh, K. P.; Sum, T. C.; White, T. J.; Shen, Z. X. Pressure-Engineered Structural and Optical Properties of Two-Dimensional $(C_4H_9NH_3)_2PbI_4$ Perovskite Exfoliated nm-Thin Flakes. *Journal of the American Chemical Society* **2019**, *141* (3), 1235-1241.

(45) Yuan, Y.; Liu, X.-F.; Ma, X.; Wang, X.; Li, X.; Xiao, J.; Li, X.; Zhang, H.-L.; Wang, L. Large Band Gap Narrowing and Prolonged Carrier Lifetime of $(C_4H_9NH_3)_2PbI_4$ under High Pressure. *Advanced Science* **2019**, *6* (15), 1900240.

(46) Liu, G.; Gong, J.; Kong, L.; Schaller, R. D.; Hu, Q.; Liu, Z.; Yan, S.; Yang, W.; Stoumpos, C. C.; Kanatzidis, M. G.; Mao, H.-K.; Xu, T. Isothermal pressure-derived metastable states in 2D hybrid perovskites showing enduring bandgap narrowing. *Proceedings of the National Academy of Sciences* **2018**, *115* (32), 8076-8081.

(47) Fang, Y.; Zhang, L.; Yu, Y.; Yang, X.; Wang, K.; Zou, B. Manipulating Emission Enhancement and Piezochromism in Two-Dimensional Organic-Inorganic Halide Perovskite $[(HO)(CH_2)_2NH_3)]_2PbI_4$ by High Pressure. *CCS Chemistry* **2020**, *3* (8), 2203-2210.

(48) Li, H.; Wines, D.; Chen, B.; Yumigeta, K.; Sayyad, Y. M.; Kopaszek, J.; Yang, S.; Ataca, C.; Sargent, E. H.; Tongay, S. Abnormal Phase Transition and Band Renormalization of Guanidinium-Based Organic–Inorganic Hybrid Perovskite. *ACS Applied Materials & Interfaces* **2021**, *13* (37), 44964-44971.

(49) Kong, L.; Liu, G.; Gong, J.; Mao, L.; Chen, M.; Hu, Q.; Lü, X.; Yang, W.; Kanatzidis, M. G.; Mao, H.-k. Highly tunable properties in pressure-treated two-dimensional Dion–Jacobson perovskites. *Proceedings of the National Academy of Sciences* **2020**, *117* (28), 16121-16126.

(50) Zhang, L.; Wang, K.; Lin, Y.; Zou, B. Pressure Effects on the Electronic and Optical Properties in Low-Dimensional Metal Halide Perovskites. *The Journal of Physical Chemistry Letters* **2020**, *11* (12), 4693-4701.

(51) Capitani, F.; Marini, C.; Caramazza, S.; Postorino, P.; Garbarino, G.; Hanfland, M.; Pisanu, A.; Quadrelli, P.; Malavasi, L. High-pressure behavior of methylammonium lead iodide (MAPbI3) hybrid perovskite. *Journal of Applied Physics* **2016**, *119* (18), 185901.

(52) Azeem, M.; Qin, Y.; Li, Z.-G.; Li, W. Cooperative B-site octahedral tilting, distortion and A-site conformational change induced phase transitions of a 2D lead halide perovskite. *Materials Chemistry Frontiers* **2021**, *5* (20), 7587-7594.

(53) Attique, S.; Ali, N.; Imran, T.; Rauf, S.; Khesro, A.; Ali, S.; Wang, W.; Khatoon, R.; Abbas, A.; Ullah khan, E.; Yang, S.; Wu, H. An overview of the pressure- and strain-induced changes in the structural and optoelectronic properties of organometal halide perovskites. *Solar Energy* **2022**, *239*, 198-220.

(54) Zhan, X.; Jiang, X.; Lv, P.; Xu, J.; Li, F.; Chen, Z.; Liu, X. Enhanced Structural Stability and Pressure-Induced Photoconductivity in Two-Dimensional Hybrid Perovskite $(C_6H_5CH_2NH_3)_2CuBr_4$. *Angewandte Chemie International Edition* **2022**, *61* (28).

(55) Hautzinger, M. P.; Dai, J.; Ji, Y.; Fu, Y.; Chen, J.; Guzei, I. A.; Wright, J. C.; Li, Y.; Jin, S. Two-Dimensional Lead Halide Perovskites Templated by a Conjugated Asymmetric Diammonium. *Inorganic Chemistry* **2017**, *56* (24), 14991-14998.

(56) Wei, Y.; Chu, H.; Chen, B.; Tian, Y.; Yang, X.; Cai, B.; Zhang, Y.; Zhao, J. Two-dimensional cyclohexane methylamine based perovskites as stable light absorbers for solar cells. *Solar Energy* **2020**, *201*, 13-20.

(57) Wei, Y.; Chu, H.; Tian, Y.; Chen, B.; Wu, K.; Wang, J.; Yang, X.; Cai, B.; Zhang, Y.; Zhao, J. Reverse-Graded 2D Ruddlesden–Popper Perovskites for Efficient Air-Stable Solar Cells. *Advanced Energy Materials* **2019**, *9* (21), 1900612.

2. Experimental Theory and Methodology

2.1 High Pressure Theory

2.1.1 Thermodynamics of High Pressure

It is well known that pressure is described by equation 2.1, where $F_{\perp}$ is the force applied perpendicular to the surface and A is the area of the surface. According to statistical mechanics, pressure can be defined using equation 2.2 as the change in the Helmholtz free energy with respect to volume at constant temperature and N, where N is the number of particles.[1]

$$P = \frac{F_{\perp}}{A} \tag{2.1}$$

$$P = -\left(\frac{\partial F}{\partial V}\right)_{T,N} \tag{2.2}$$

The phase of a material depends heavily on the pressure and temperature, and the most stable phase is often achieved when the Gibbs free energy (G) is at a minimum. A phase transition is said to occur when the changes in G are associated with changes in the structural details of the phase. A phase transition is usually either first or second order. A first order phase transition occurs when the first derivative of G with respect to any thermodynamic variable is discontinuous at the phase boundary, for example volume in equation 2.3. The phase boundary between two phases is defined as the temperature-pressure conditions at which G is the same for both phases. The energy barrier for changing phases for first order transitions is known as the latent heat. If the first derivative is continuous but the second derivative is discontinuous, a second order phase transition is said to occur. Second order transitions are both smooth and have no energy barriers at the phase boundary.

$$(\frac{\partial G}{\partial P})_T = V \tag{2.3}$$

An equation that relates the volume, pressure, and temperature of a certain phase is known as an equation of state (EOS). For example, the EOS for an ideal gas is commonly known as the ideal gas law. Several EOS have been proposed for high-pressure studies, with the most common one being the Birch-Murnaghan (B-M) EOS.[1,2] Typically, the third order B-M EOS is used and is shown by equation 2.4, where V_0 and B_0 are the volume and bulk modulus at 0 GPa, respectively.[1] The third order B-M EOS can be simplified to the second order B-M EOS by simply setting $B_0' = 4$.

$$P = \frac{3}{2}B_0\left[\left(\frac{V_0}{V}\right)^{\frac{7}{3}} - \left(\frac{V_0}{V}\right)^{\frac{5}{3}}\right]\left[1 - \frac{3}{4}(4 - B_0')\left[\left(\frac{V_0}{V}\right)^{\frac{2}{3}} - 1\right]\right] \tag{2.4}$$

A crucial factor of the B-M EOS is the bulk modulus, which is a measure of the resistance towards compression in a material. Coincidently, the compressibility is inversely proportional to the bulk modulus. The bulk modulus at P = 0 GPa can be seen in equation 2.5, while for an isothermal compression computing the derivative of the bulk modulus is also important, as seen at P = 0 GPa in equation 2.6.[2]

$$B_0 = -V\left(\frac{\partial P}{\partial V}\right) \tag{2.5}$$

$$B_0' = \left(\frac{\partial B_0}{\partial P}\right) \tag{2.6}$$

2.1.2 Crystallography

A crystal is a solid that is formed through the infinite repetition of identical groups of atoms/ions/molecules (known as a basis), which are attached by a set of mathematical points known as the lattice.[3] The smallest volume that contains the characteristics of the lattice is called the unit cell and the infinite repetition of this cell in 3D forms the crystal lattice. The crystal structure of a compound can be described using the six lattice parameters (*a*, *b*, and *c* for the dimensions made by the edges and α, β, λ for the angles made by the edges at the vertex). Furthermore, the spacing between the planes in the crystal is known as the d-spacing (d_{hkl}). In this work, the $DPDAPbI_4$ sample exhibits a monoclinic crystal structure with a primitive (P) lattice where $a \neq b \neq c$ and $\alpha = \gamma = 90^{\circ} \neq \beta$. The $CMA_2MAPb_2I_7$ and $CMA_2FAPb_2I_7$ compounds exhibit an orthorhombic crystal structure with a primitive lattice where $a \neq b \neq c$ and $\alpha = \gamma = \beta = 90^{\circ}$. The equations for the d-spacings are given by equations 2.7 (monoclinic) and 2.8 (orthorhombic).

$$\frac{1}{d_{hkl}^2} = \frac{1}{sin^2\beta}\left(\frac{h^2}{a^2} + \frac{k^2 sin^2\beta}{b^2} + \frac{l^2}{c^2} - \frac{2hl\cos\beta}{ac}\right) \tag{2.7}$$

$$\frac{1}{d_{hkl}^2} = \frac{h^2}{a^2} + \frac{k^2}{b^2} + \frac{l^2}{c^2} \tag{2.8}$$

2.1.3 Phonons

Similar to how a photon is a quantum of electromagnetic/light energy, a phonon is classified as a quantum of vibrational energy in the crystal lattice, whose energy can be described by equation 2.9.[3]

$$\epsilon = \left(n + \frac{1}{2}\right)\hbar\omega \tag{2.9}$$

Crystals contain both acoustic (longitudinal and transverse) and optical (longitudinal and transverse) phonons.[3] The primitive cell (smallest possible unit cell) with n atoms contains $3n$ vibrational modes, 3 acoustic modes (one longitudinal and two transverse) and $3n - 3$ optical modes.[3]

Phonons can be thought of as harmonic oscillators, which can be described using Hooke's Law whereby the greater the spring constant (k), the greater the vibrational frequency and thus the greater the energy. As high pressure tends to push atoms and molecules closer together, which in turn decreases the bond length and thus increases the bond strength. Such stronger bonds lead to greater spring constants and thus high-pressure results in greater vibrational energy modes.

2.1.4 Bandgap

As previously discussed, 2D hybrid organic-inorganic perovskites (HOIPs) are semiconducting materials, consisting of the valence and conduction bands, separated by the bandgap. The bandgap can be described as the difference in energy between the conduction band minimum (conduction band edge) and the valence band maximum (valence band edge), with thermal excitation of electrons upon increasing the temperature.[3]

The electronic structure of crystalline semiconductors can be described using band theory. The crystal momentum (k-vector) plays a key role in determining the type of bandgap present. If the k values of the CBM and VBM are the same, then the bandgap is considered direct, meaning a direct transfer of electrons upon absorption of energy equivalent to the energy difference is permitted. If the k values of the CBM and VBM are different, then the bandgap is considered indirect, meaning

the electrons must absorb energy from a phonon that is equivalent to the wavevector (k_c) separating the electrons and the holes in the band structure.[3] Figure 2.1 illustrates the schematics of direct and indirect bandgaps. and the holes in the band structure.[3] and the holes in the band structure.[3] Figure 2.1 illustrates the schematics of direct and indirect bandgaps. and the holes in the band structure.[3]

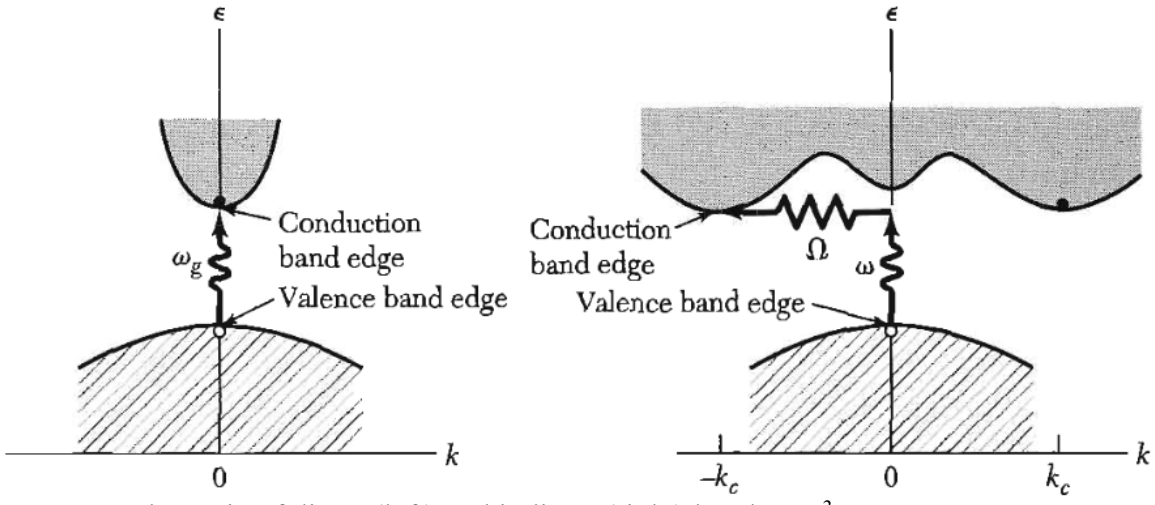

Figure 2.1. Schematic of direct (left) and indirect (right) bandgaps.[3]

2.1.5 Excitons

Upon the absorption of energy equivalent to the bandgap, the subsequent excited electron leaves a positively charged hole in the valence band, which can in turn interact with free electrons in the conduction band via Coulombic attraction, thus forming electron-hole pairs known as excitons.[4] Excitons can be classified as either free, excitons that move freely through the crystal, or self-trapped (STE), excitons that are surrounded by a dense cloud of phonons, thus deforming the lattice making it difficult for the excitons to move. STEs are more stable than free excitons, meaning electrons and holes will self-trap immediately upon photogeneration.[5]

2.2 Diamond Anvil Cell

2.2.1 DAC & Components

High pressure in this study was achieved using a diamond anvil cell (DAC), one of the most common tools used for high pressure studies. As a result of being the hardest material on earth capable of withstanding very high pressure, along with its transparency to both visible light and x-rays, diamond is ideal for the achievement of high pressure.[6,7] A DAC consists of two diamond anvils, a piston and cylinder, 2 seats, 4 screws with washers, a metal gasket, pressure gauge, and occasionally a pressure transmitting medium (PTM). Each diamond is placed in separate seats with one on the piston and the other on the cylinder, as seen in Figure 2.2. A small amount of sample is placed into the gasket which is then placed between the two diamond anvils and pressure is applied by turning the screws, compressing the cell. The two main types of diamonds used in DACs are type I and type II, while the size of the culet is often 400 or 600 microns, depending on the type used.

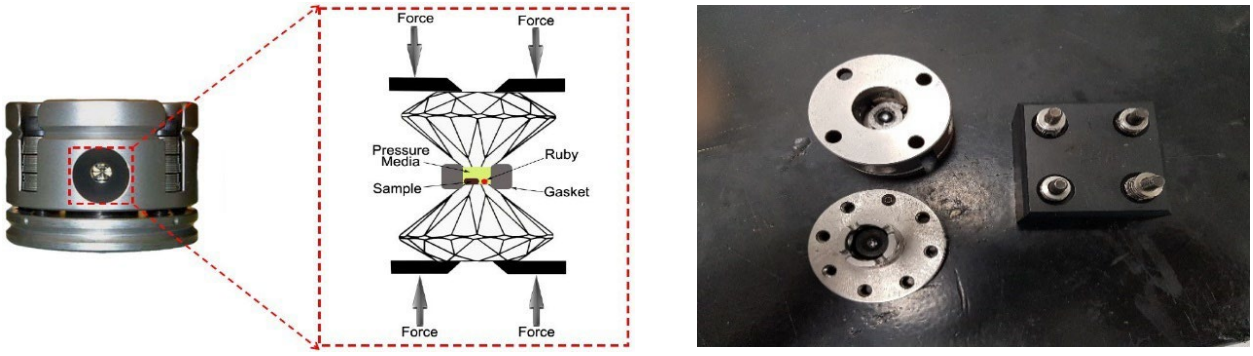

Figure 2.2. Schematic of DAC.[8]

The screws are prepared such that two are right-handed and the other two are left-handed, thus allowing for a more symmetrical application of pressure. Turning both sets of screws in the same direction by the same distance allows for the increase of pressure, whilst also ensuring the diamonds do not crack or get damaged. The washers are stacked on the screws in an up-down

configuration to again allow for better control when applying pressure. For this study, washers were stacked in groups of 8, with 4 up followed by 4 down.

The gaskets are generally made of stainless steel due to its hardness and relatively low cost. Preparation involves first pre-indenting the metal gasket by applying pressure using the DAC, for this study pre-indentation was done up to 8 GPa. Afterwards the sample chamber is created by drilling a hole into the gasket using an electronic discharge machine, while the size depends on the size of the culet used. For this study 210-micron needles were used to drill the holes for the Raman, FTIR, and PL measurements, while 260-micron needles were used to drill the holes for the UV-Vis measurements.

2.2.2 Pressure Gauges

Pressure calibration was a significant obstacle during the early years of the DAC, an issue eventually eliminated with the introduction of the ruby fluorescence method in 1972 by Forman et al., which uses rubies (Cr^{3+} doped Al_2O_3, $Al_2O_3 : Cr^{3+}$) to measure the pressure.[6,7] Ruby fluorescence consists of a doublet emission at ambient pressure, denoted R_1 ($\lambda = 692.7$ nm) and R_2 ($\lambda = 694.2$ nm), which redshift linearly as pressure is increased.[6] A wavelength-pressure relationship for the R_1 was obtained by comparing the observed redshift to fixed pressure points of well-known freezing points of various liquids and certain solid-solid phase transitions.[6] Forman et al. determined that the R lines experience broadening if the ruby is subjected to non-hydrostatic pressure, along with the linear shift when the ruby is subjected to hydrostatic pressure in the 1-22 kbar range.[6] The pressure-induced ruby fluorescence peaks along with the observed redshift can be seen in Figure 2.3.[9] The pressure-wavelength relationship can be described by equation 2.10,

where $\Delta\lambda$ is the change in wavelength, λ_0 is the wavelength at ambient pressure, and A and B are constants which are determined through empirical fitting, for this study we use A = 1904 and B = 7.665.[10]

$$P(GPa) = \frac{A}{B}\left[\left(1 + \frac{\Delta\lambda}{\lambda_0}\right)^B - 1\right] \tag{2.10}$$

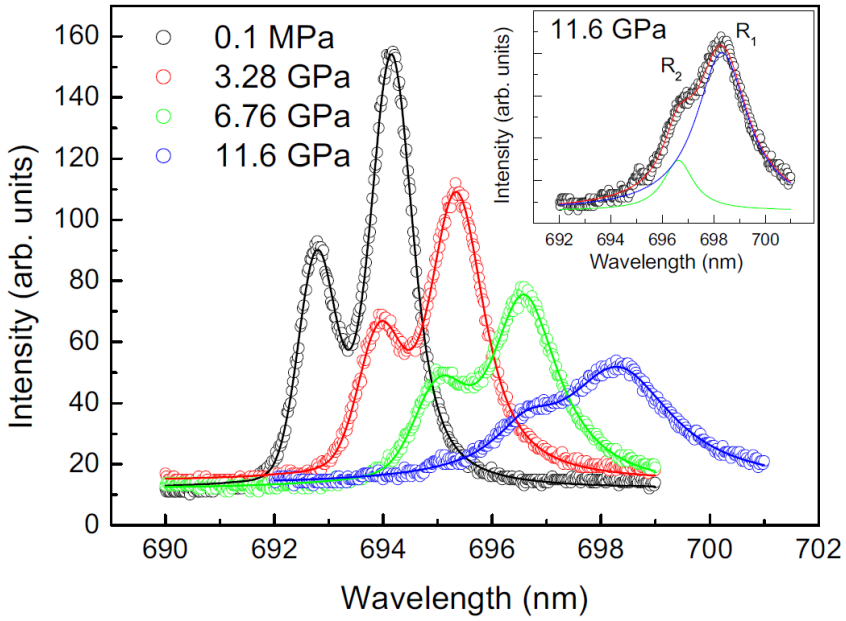

Figure 2.3. Ruby fluorescence peaks under pressure.[9]

In this study, ruby balls were loaded into the gasket chamber along with the samples for the Raman, FTIR, Photoluminescence (PL), and UV-Visible Absorption measurements. Whilst most measurements in this study made use of the ruby fluorescence method, pressure measurements for XRD measurements pressure were achieved using the XRD patterns of gold flakes in the sample and the equation of state for gold. Gold was used as XRD measurements were performed remotely, and thus in-person handing was not required, as opposed to the ruby fluorescence method. Ruby fluorescence measurements require taking the pressure readings using another system, thus the DAC must be manually moved.

2.2.3 Pressure Transmitting Media

The broadening of the R lines due to nonhydrostatic pressure can lead to a poor transmission of pressure in solids, thus resulting in a pressure gradient across the sample.[6,11] This gradient can cause the sample to experience different bulk modulus and shear-induced phase transitions, which are inconsistent and unreliable.[12,13] A pressure transmitting media (PTM), which are typically liquids that remain in the liquid phase in the low pressure range along with being very soft in the solid phase, thus allowing for the PTM to deform, resulting in a uniform transmission of pressure, reducing the pressure gradient. Complex fluids such as a 4:1 methanol-ethanol mixture remains hydrostatic up to 104 kbar at ambient temperature, while adding a small amount of water to create a 16:3:1 methanol-ethanol-water mixture provides a hydrostatic range up to 145 kbar.[6] Inert gases such as helium, neon, argon, and other liquids like silicone oil and N_2 are also commonly used.[6,11]

In this study, KBr was used as the PTM for the Fourier-transform infrared (FTIR) measurements due to its transparency to mid-infrared light. Silicone oil was used as the PTM for the X-ray diffraction (XRD), Photoluminescence (PL), and UV-Vis absorption measurements. KBr was obtained from PIKE Technologies as a solid under ambient conditions and silicone oil (5 cSt viscosity) was obtained from Sigma-Aldrich.

2.2.4 Sample Preparation

All three samples examined in this study: $DPDAPbI_4$, $CMA_2MAPb_2I_7$, and $CMA_2FAPb_2I_7$ were synthesized by Matthew Hautzinger from Prof. Song Jin's group at the University of Wisconsin-Madison. Powder samples were used for Raman and FTIR measurements by packing the ground power into the gasket chamber. For XRD measurements, the ground powder was packed into the

DAC without the gasket to increase the density order, thus providing higher diffraction intensities. KBr was loaded along with the powder samples in the gasket for the FTIR measurements to help reduce laser damage. Raman measurements did not require any PTM as the highest achieved pressure was relatively low and minimal laser damage was observed. Silicone oil was used as the PTM for XRD, PL, and UV-Vis absorption measurements. PL and UV-Vis measurements were done using single crystals as they were found to give more accurate results, with both the crystals and silicone oil being loaded into the gasket chamber.

2.3 Experimental Techniques

Structural and optoelectronic properties of all three samples were studied through Raman, FTIR, XRD, PL, and UV-Vis measurements. Vibrational spectroscopy like Raman and FTIR help to examine the changes in vibrational frequencies as pressure increases, which can in turn provide useful information on the structural properties. Splitting/merging of peaks, appearance/disappearance of new/old peaks, and sudden changes in the Raman shift as pressure changes can help identify possible phase changes. The broadening and gradual disappearance of peaks as pressure increases can help identify amorphization. Phase changes can also be observed in XRD measurements through peak splitting, peak appearance/disappearance, and sudden changes in peak shifts which can help identify the crystal structure of the compound in the low and high-pressure phases. Optoelectronic properties, such as photoluminescence and bandgap can be determined through PL and UV-Vis measurements.

2.3.1 Raman Spectroscopy

There are two forms of scattering that occur when monochromatic light is used to illuminate a material, elastic, and inelastic scattering. Elastic scattering, known as Rayleigh scattering, is the most common and occurs when the scattered photons have the same frequency as the incident beam (v_0) and is strong.[14] Inelastic scattering, known as Raman scattering, occurs when the photons are scattered with a very weak intensity (around 10^{-5} times v_0) and frequency of $v_0 \pm v_m$, where v_m is the vibrational frequency of the molecule.[14] The Raman scattering of a photon follows either the emission or absorption of a phonon and can be described using a Feynman diagram (Figure 2.4).[3] The shifts in frequency are classified as either Stokes ($v_0 - v_m$) where a photon of lower energy is emitted and is subsequently shifted downfield to a lower frequency and excited to a higher vibrational energy level (phonon emission), or Anti-Stokes ($v_0 + v_m$) where a photon of higher energy is emitted and is subsequently shifted upfield to a higher frequency and relaxed to a lower vibrational energy level (phonon absorption).[14] The processes of Stokes and Anti-Stokes scattering can be seen in Figure 2.4, where ω, k correspond to the incident photon, ω', k correspond to the scattered photon, and Ω, K correspond to the emitted/absorbed phonon.[3]

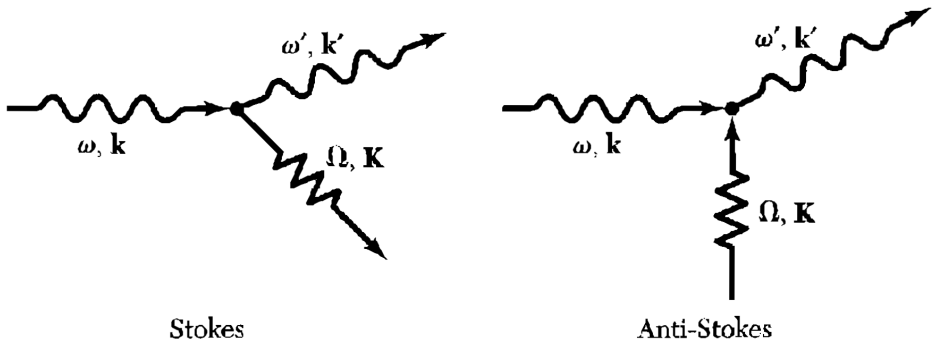

Figure 2.4. Schematic of Raman shifts: Stokes (left) and Anti-Stokes (right).[3]

Classical theory can be used to explain Raman scattering as shown in equation 2.11, where α is the polarizability, q is the nuclear displacement, α_0 is the polarizability at equilibrium, and q_0 is the displacement at equilibrium.[14] For Raman scattering to be possible, the rate of change of α with respect to the change in q evaluated at equilibrium must not equal zero (Raman active).[14]

$$\alpha = \alpha_0 + (\frac{\partial \alpha}{\partial q})_0 q_0 \ + \ \ldots \tag{2.11}$$

$$(\frac{\partial \alpha}{\partial q})_0 \neq 0$$

Quantum mechanically, during Raman scattering a phonon is either created or destroyed, where the energy ($h\nu$) is stated by equation 2.12, where ν_{photon} is the frequency of the scattered photon and ν_{phonon} is the frequency of the created/destroyed phonon.[3]

$$h\nu_{photon} = h\nu_0 \pm h\nu_{phonon} \tag{2.12}$$

For this study, an Acton SpectraPro 2500i spectrometer was used for the Raman measurements, which includes a charged coupled device detector that is cooled by liquid nitrogen. The grating used was 1200 l/mm and calibration was done using neon emission lines. Manual adjustment of the DAC was performed once mounted on the stage. A schematic of the system can be seen in Figure 2.5. The laser used was a class 3B diode red laser (λ = 780 nm) with a maximum power < 500 mW due to the PL of the samples studied, in particular *DPDAPbI*$_4$.

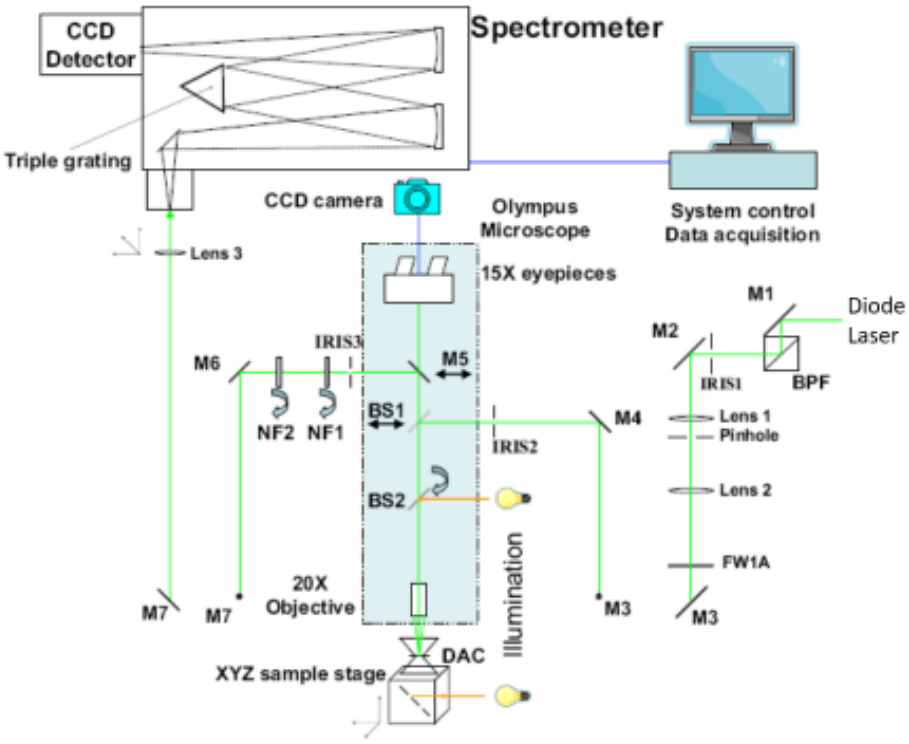

Figure 2.5. Schematic of Raman system.[15]

2.3.2 FTIR Spectroscopy

In contrast to Raman spectroscopy, FTIR spectroscopy involves the absorption of photons. The absorbance is obtained by taking a reference spectrum (I_0) in addition to the sample spectrum (I) and is then calculated along with the transmission using the Beer-Lambert law, as seen in equation 2.13, where α is the absorbance and T is the transmittance.

$$\alpha = \log_{10}(\frac{I_0}{I}) \tag{2.13}$$

$$T = \frac{I}{I_0}$$

While in Raman spectroscopy monochromatic is used as the beam, in FTIR spectroscopy the beam is formed from broadband light that is passed through a Michelson interferometer, which helps to

collimate the incoming light and controls the wavelengths of light emitted towards the sample. Once collimated, the light is then sent to a beam splitter, a fraction of the original light is sent through the sample and then refocused towards the detector.

For this study a VERTEX 80V FTIR spectrometer from Bruker with a mercury cadmium telluride midband detector that was cooled with liquid nitrogen was used. The detector allowed for measurements between 600 cm^{-1} and 5000 cm^{-1}, with manual adjustment of the DAC being performed once mounted on the stage. A schematic of the system can be seen in Figure 2.6. A background was taken by first loading an empty gasket into the DAC and adjusting the iris to the same size as the gasket hole, which is left unchanged for the duration of the background measurement. The gasket was then removed, the DAC is closed ensuring the diamonds do not touch, the edge is located and focused, and finally the position is readjusted, and the background is taken and used as the reference spectrum taken and used as the reference spectrum touch, the edge is located and focused, and finally the position is readjusted, and the background is taken and used as the reference spectrum.

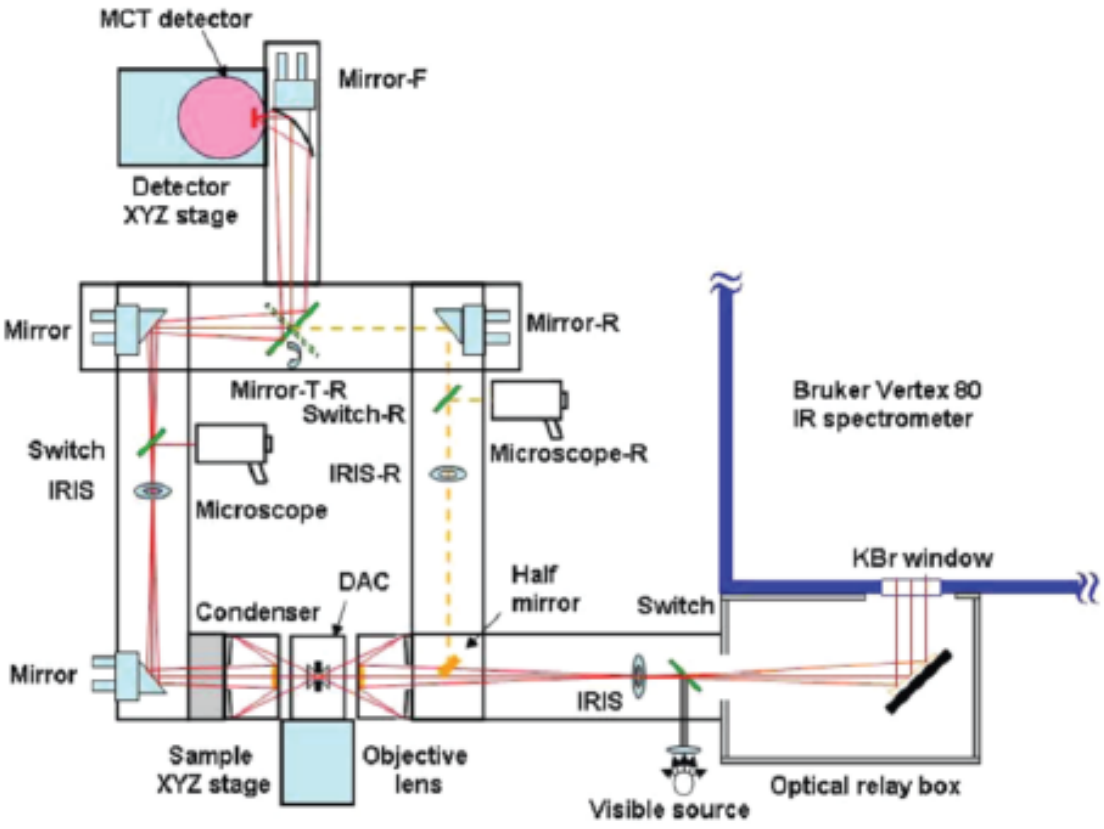

Figure 2.6. Schematic of FTIR system.[16]

2.3.3 X-Ray Diffraction

In regards to determining the structure of crystalline materials, diffraction is the most common method, with the three main techniques using x-rays, electrons, and neutrons. However, as diamond is unable to effectively transmit electrons and neutrons, X-ray diffraction (XRD) is the most convenient diffraction technique for DACs. X-ray diffraction involves subjecting the material to a beam of collimated monochromatic hard x-rays (on the order of angstroms). Upon contact with the crystal, the x-rays are diffracted, producing patterns resulting from both constructive and deconstructive inferences, and thus the intensities and angles can be measured. As crystalline substances consist of parallel rows of atoms separated by a "unique" distance known as the d-spacing, XRD patterns follow Bragg's Law, as seen in equation 2.14 and Figure 2.7, where n is

the order of diffraction, λ is the wavelength, d is the d-spacing, θ is the diffraction angle, and d and θ are dependent on the Miller indices (hkl).[17]

$$n\lambda = 2d_{hkl}sin\theta_{hkl} \tag{2.14}$$

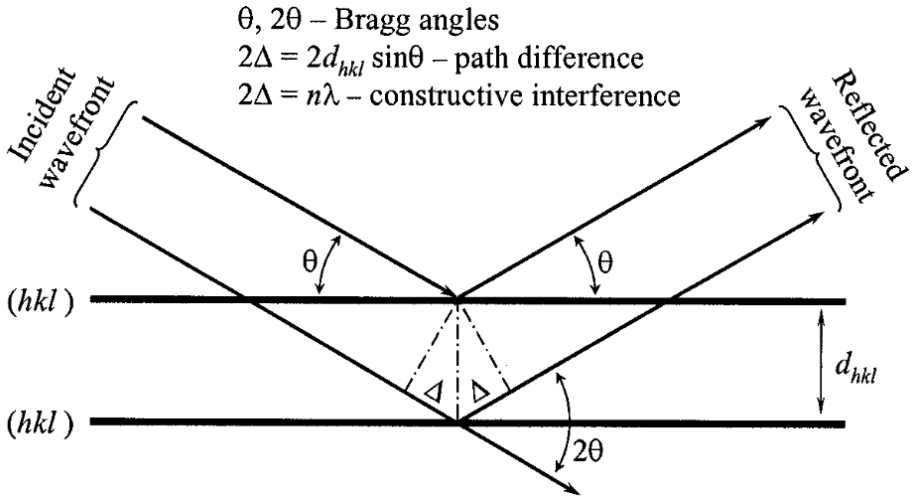

Figure 2.7. Schematic of Bragg's Law.[17]

While XRD measurements of a sample can be conducted in either single crystal or powder form, all measurements in this study were performed with powder samples. Single crystal diffraction uses crystals to reflect the x-ray beam to measure the angles and intensities. However, while all information about the structure can be obtained, single crystals are difficult and sometimes impossible to prepare, orienting the crystal is time-consuming, and data analysis is often complicated if more than one phase is present. Powder diffraction involves using a crushed powder sample to diffract the x-ray beam. In comparison to its single crystal counterpart, some key advantages to powder diffraction are that powder samples are easier to prepare, observation of all reflections are guaranteed, and is the best way to monitor phase changes as a function of temperature and pressure. Thus, it is crucial to crush the sample into a fine powder.

XRD measurements can be done in the lab, however poor XRD quality is common given the relatively low intensity of x-ray emission from in-lab sources. Thus, for experiments using a DAC, synchrotron XRD is preferred due to their much greater emission intensities and ability to choose the wavelength. Synchrotron x-ray sources also provide more intense peaks due to the high emission intensity, thus leading to a better signal-to-noise ratio.

Refinement of the 1D XRD powder patterns allows for structural analysis at high pressure. The most effective refinement method is Rietveld refinement, which can provide the lattice parameters, which can in turn be used to determine potential phase changes and obtain the bulk modulus of a particular phase. The lattice parameters can also be used to determine any anisotropic compression present upon compression. The subsequent crystal structures at high-pressure can be used to determine the bond lengths and bond angles. This allows for the analysis of potential distortion of the lead-halide octahedra, further providing a better understanding of the connection between the structural modifications and the pressure-tuned optoelectronic properties. Furthermore, amorphization of the sample can also been identified through broadening of the XRD peaks upon compression.

For this study, the high pressure XRD measurements were performed remotely at the 16-BMD and 16-IDB HPCAT beamlines at the Advanced Photon Source (APS). Samples were prepared and pre-loaded in-lab before being shipped directly to the APS. DACs were mounted with a membrane on the stage, both of which were controlled manually. NoMachine, a remote desktop software, was used to remotely align the DAC and collect the diffractograms, with very fine *CeO2* used as the calibration for both beamlines. Dioptas was used to mask and integrate the diffractograms. For the

DPDA sample, the 1D XRD powder patterns were refined first through LeBail refinements and then further through Rietveld refinements to obtain both the cell parameters and unit cell volumes using GSAS-II (General Structure Analysis System II).[18] For the CMA samples, only LeBail refinements were performed.

2.3.4 Photoluminescence

Photoluminescence occurs upon the emission of light following the absorption of photons. In semiconducting materials, photons are emitted upon radiative recombination of electron-hole pairs. In 2D HOIPs, this recombination often occurs through exciton emission, generally either free (FE), self-trapped (STE), and at times both.[19,20,21,22] The total energy of an exciton is given by equation 2.15, where E_g is the bandgap energy, E_x is the exciton binding energy, and E_{kin} is the kinetic energy.

$$E_n = E_g - E_x + E_{kin} \tag{2.15}$$

Photoluminescence measurements were performed using the same Acton SpectraPro 2500i spectrometer and LN2-cooled charged-coupled device detector as the Raman system. A beam splitter was used to direct the laser towards the sample. Excitation was achieved using a Laserglow Technologies continuous-wave diode-pumped solid-state laser emitting at a 360 nm wavelength with maximum laser power of 0.25 mW to ensure no laser-induced damage. The DAC was manually adjusted once mounted on the xyz stage, and a 300 l/mm grating was used to allow for a larger wavelength band to be measured. A schematic of the system can be seen in Figure 2.8.

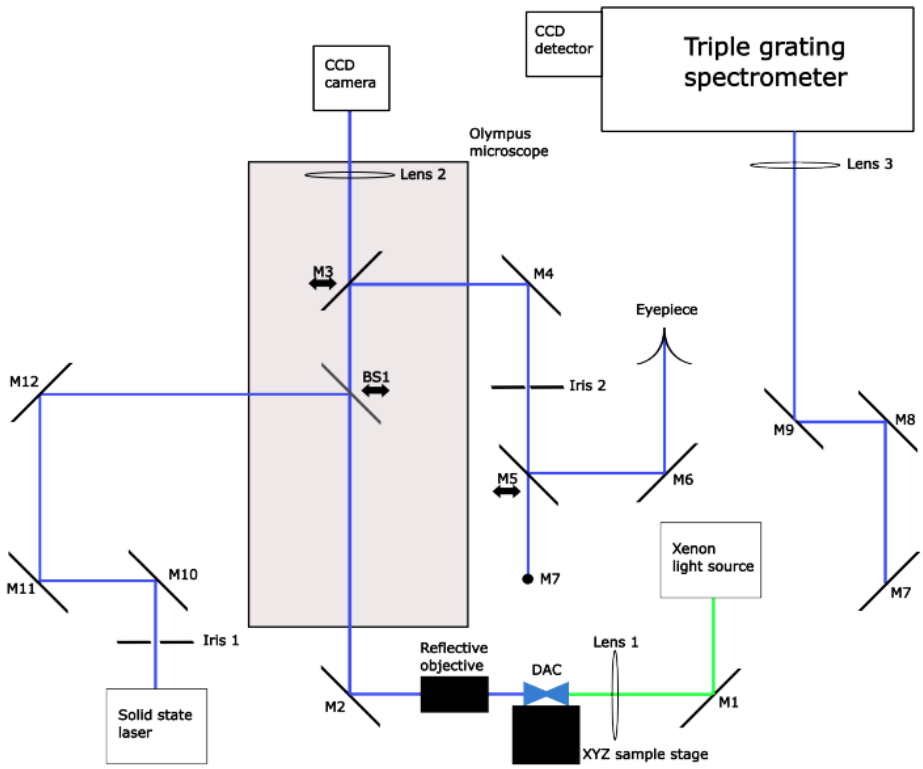

Figure 2.8. Schematic of PL and UV-Vis system.[23]

2.3.5 UV-Visible Absorption

UV-Visible absorption spectroscopy is a common technique used to measure the amount of light a sample absorbs in both the UV and visible parts of the electromagnetic spectrum. Semiconducting materials will absorb light with greater energy than its bandgap and in turn transmit light with lower energy than the bandgap. In order to obtain an accurate measurement, a background must be taken first with the empty gasket to determine the transmission through the diamond anvils, which in this case acts as the sample holder. For all UV-Vis measurements in this study a background measurement was taken at the beginning and used for all pressure points. Silicone oil was used as the PTM, with a single crystal being loaded such that it only covers part

of the gasket with the other part covered by the silicone oil. After the background is taken the transmission is measured and the subsequent absorbance can be calculated.

The absorbance was calculated using equation 2.16, where T is the transmittance. The bandgap can then be calculated using the absorbance and equation 2.17, where α is the absorption coefficient, E_g is the bandgap, and A is a proportionality constant.[24] The value of n is determined by the nature of the electronic transition, either allowed or forbidden and direct or indirect, summarized in Table 2.1.[24]

$$A = -\log_{10} T \tag{2.16}$$

$$(\alpha h\nu)^{\frac{1}{n}} = A\left(h\nu - E_g\right) \tag{2.17}$$

Table 2.1. Values for n for electronic transitions

Type of Transition	Allowed/Forbidden	n
direct	allowed	1/2
direct	forbidden	3/2
indirect	allowed	2
indirect	forbidden	3

Upon plotting $\alpha h\nu \; vs. \; h\nu$ (known as a Tauc plot), the bandgap can then be extrapolated by fitting the linear portion of the plot with the bandgap being the x-intercept.[24] The Tauc method has been used as an effective method for estimating the bandgap of materials, such as for ZnO shown in Figure 2.9 below.[24]

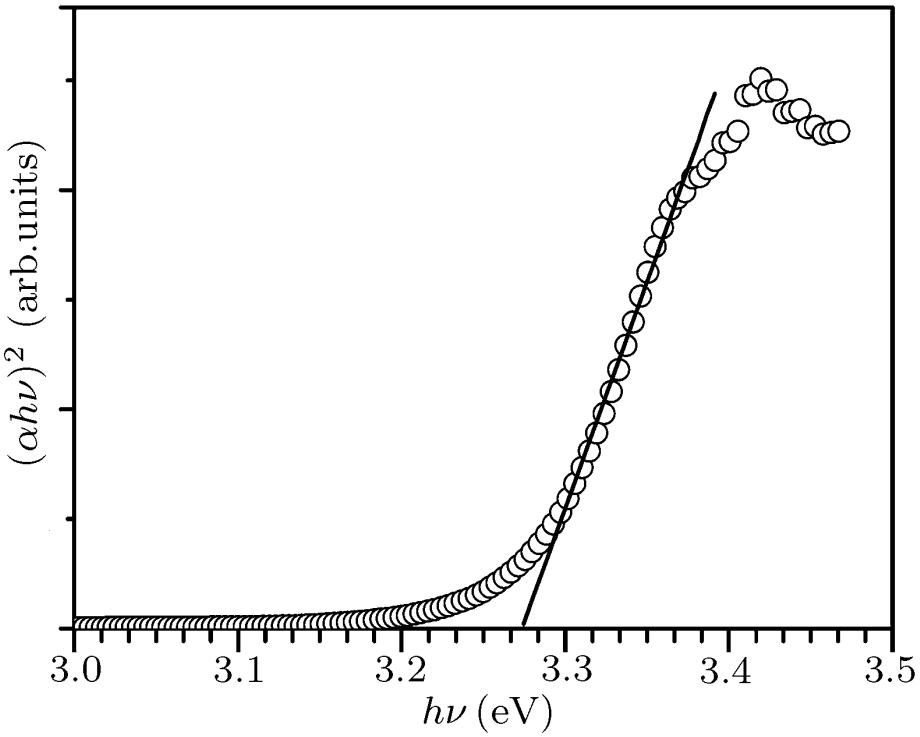

Figure 2.9. Tauc plot of ZnO thin film with bandgap of 3.27 eV.[24]

Monitoring the bandgap change, either a reduction or increase, upon compression can help further the understanding of the potential PL changes. The structural modifications can then be used to determine the mechanisms behind the bandgap change, thus providing valuable insights into the effects at high-pressure on the studied materials.

UV-Vis measurements in this study were performed using an Ocean High-Resolution spectrometer from Ocean Insight, employing a setup similar to the PL measurements (Figure 2.8). The beam splitter was pulled out as laser excitation is not required for UV-Vis measurements. A 75 W xenon light source from ThorLabs with an emission wavelength range of 240-1200 nm was used, and an optical fiber was employed to direct the light to the sample. The DAC was manually adjusted once mounted on the xyz stage. Similar to the FTIR measurements, an iris was used to select a region

of sample chamber, which remained unchanged once selected. A reference spectrum was obtained using an empty portion of the chamber, followed by a dark background measurement by blocking the light source in the same empty section. Once both spectrums were saved, a portion of the sample was moved into place and the measurement was taken.

2.4 References

(1) Katsura, T. and Tange, Y. A Simple Derivation of the Birch–Murnaghan Equations of State (EOSs) and Comparison with EOSs Derived from Other Definitions of Finite Strain. In *Minerals*, **2019**; Vol. 9.

(2) Kholiya, K.; Chandra, J.; Verma, S. Analysis of Equation of States for the Suitability at High Pressure: MgO as an Example. *The Scientific World Journal* **2014**, *2014*.

(3) Kittel, C. *Introduction to Solid State Physics*; Wiley, **2005**.

(4) Hoye, R. L. Z.; Hidalgo, J.; Jagt, R. A.; Correa-Baena, J.-P.; Fix, T.; MacManus-Driscoll, J. L. The Role of Dimensionality on the Optoelectronic Properties of Oxide and Halide Perovskites, and their Halide Derivatives. *Advanced Energy Materials* **2022**, *12* (4), 2100499.

(5) Li, S.; Luo, J.; Liu, J.; Tang, J. Self-Trapped Excitons in All-Inorganic Halide Perovskites: Fundamentals, Status, and Potential Applications. *The Journal of Physical Chemistry Letters* **2019**, *10* (8), 1999-2007.

(6) Jayaraman, A. Diamond anvil cell and high-pressure physical investigations. *Reviews of Modern Physics* **1983**, *55* (1), 65-108.

(7) Bassett, W. A. Diamond anvil cell, 50th birthday. *High Pressure Research* **2009**, *29* (2), 163-186.

(8) Zhaohui, D.; Yang, S. Novel Pressure-Induced Structural Transformations of Inorganic Nanowires. In *Nanowires*, Abbass, H. Ed.; IntechOpen, 2011; p Ch. 23.

(9) Jeong, M.-S.; Kim, J. H.; Ko, J.-H.; Ko, Y. H.; Kim, K. J. Pressure dependence of acoustic behaviors and refractive index of amorphous Kel F-800 copolymer studied by Brillouin spectroscopy. *Current Applied Physics* **2013**, *13* (8), 1774-1777.

(10) Mao, H. K.; Bell, P. M.; Shaner, J. W.; Steinberg, D. J. Specific volume measurements of Cu, Mo, Pd, and Ag and calibration of the ruby R1 fluorescence pressure gauge from 0.06 to 1 Mbar. *Journal of Applied Physics* **1978**, *49* (6), 3276-3283.

(11) Klotz, S.; Chervin, J. C.; Munsch, P.; Le Marchand, G. Hydrostatic limits of 11 pressure transmitting media. *Journal of Physics D: Applied Physics* **2009**, *42* (7), 075413.

(12) Takemura, K. and Dewaele, A. Isothermal equation of state for gold with a He-pressure medium. *Physical Review B* **2008**, *78* (10), 104119.

(13) Duwal, S. and Yoo, C.-S. Shear-Induced Isostructural Phase Transition and Metallization of Layered Tungsten Disulfide under Nonhydrostatic Compression. *The Journal of Physical Chemistry C* **2016**, *120* (9), 5101-5107.

(14) Ferraro, J. R.; Nakamoto, K.; Brown, C. W. *Introductory Raman Spectroscopy*; Academic Press, 2003.

(15) Dong, Z. High-Pressure Study of Molecular Solid and 1D Nanostructures by Vibrational Spectroscopy and Synchrotron X-ray Diffraction. University of Western Ontario, 2012.

(16) Dong, Z. and Song, Y. Transformations of Cold-Compressed Multiwalled Boron Nitride Nanotubes Probed by Infrared Spectroscopy. *The Journal of Physical Chemistry C* **2010**, *114* (4), 1782-1788.

(17) Pecharsky, V. K.; Zavalij, P. Y. *Fundamentals of Powder Diffraction and Structural Characterization of Materials, Second Edition*; Springer, **2009**.

(18) Toby, B. H. and Von Dreele, R. B. GSAS-II: the genesis of a modern open-source all purpose crystallography software package. *Journal of Applied Crystallography* **2013**, *46*, 544-549.

(19) Kong, L.; Liu, G.; Gong, J.; Mao, L.; Chen, M.; Hu, Q.; Lü, X.; Yang, W.; Kanatzidis, M. G.; Mao, H.-k. Highly tunable properties in pressure-treated two-dimensional Dion–Jacobson perovskites. *Proceedings of the National Academy of Sciences* **2020**, *117* (28), 16121-16126.

(20) Zhang, L.; Wang, K.; Lin, Y.; Zou, B. Pressure Effects on the Electronic and Optical Properties in Low-Dimensional Metal Halide Perovskites. *The Journal of Physical Chemistry Letters* **2020**, *11* (12), 4693-4701.

(21) Fang, Y.; Zhang, L.; Yu, Y.; Yang, X.; Wang, K.; Zou, B. Manipulating Emission Enhancement and Piezochromism in Two-Dimensional Organic-Inorganic Halide Perovskite [(HO)(CH2)2NH3)]2PbI4 by High Pressure. *CCS Chemistry* **2020**, *3* (8), 2203-2210.

(22) Fang, Y.; Wang, J.; Zhang, L.; Niu, G.; Sui, L.; Wu, G.; Yuan, K.; Wang, K.; Zou, B. Tailoring the high-brightness “warm” white light emission of two-dimensional perovskite crystals via a pressure-inhibited nonradiative transition. *Chemical Science* **2023**, *14* (10), 2652-2658.

(23) Ratte, J. Pressure-Induced Modifications to the Structural and Optoelectronic Properties of 2D Hybrid Organic-Inorganic Perovskites. University of Western Ontario, 2022.

(24) Viezbicke, B. D.; Patel, S.; Davis, B. E.; Birnie Iii, D. P. Evaluation of the Tauc method for optical absorption edge determination: ZnO thin films as a model system. *physica status solidi (b)* **2015**, *252* (8), 1700-1710.

3. Effects of High Pressure on the Structures and Optoelectronic Properties of *DPDAPbI$_4$*

3.1 Introduction

The organic spacer is of particular interest in regards to the structural and optical properties of 2D HOIPs.[1,2,3] The selection of the organic spacer is highly important in regards to maintaining structural stability in the 2D structure, with several factors governing the selection.[1,3] One such factor is the charge of the spacer, with 1+ (monovalent) and 2+ (divalent) spacers the most common for 2D HOIPs, while trivalent (3+) and higher charge spacers are not ideal due to their inability to achieve charge balance.[3] Another important factor is the shape of the spacer, with considerations required for both the amino head and the organic tail.[3] Primary ammonium cations are preferred for 2D HOIPs as they are much easier to insert between the inorganic layers.[3] The organic tail can adopt 1 of 3 shapes: linear, branched, or cyclic, with linear tails the most flexible and most common for 2D HOIPs whilst cyclic tails are the least flexible due to restricted position of the ring.[3] The size of the spacer is also of importance, for example it was reported that the linear spacers for n = 1 2D HOIPs contain 18 carbons.[3] On the other hand, cyclic spacers with 3-6 carbons were the only one found to form 2D HOIPs, with greater member rings only able to form 1D structures.[3,4]

The <100> orientation is the most common for 2D HOIPs, with the major classes being Ruddlesden-Popper (RP) and Dion-Jacobson (DJ) perovskites.[2,5] While the RP type has been more extensively studied, DJ-type perovskites have been gaining interest in recent years. In particular, focus has been shifted towards 2-dimensional network (2DN) lead halide perovskites which are

templated by alkylammonium dications, (NRN)PbX_4 (NRN = alkyldiammonium).[6,7,8,9,10,11] One such example is *$DPDAPbI_4$*, a DJ 2D HOIP where the N,N-dimethylphenylene-*p*-diammonium (DPDA) spacer is divalent (m = 1) and thus has a 2+ charge. Furthermore, the DPDA spacer is both rigid and asymmetrically substituted into the spaces formed by the *PbI_6* octahedra, as seen in Figure 3.1b, thus leading to greater distortion in the lead halide octadehra.[6] 2D metal halide perovskites are of particular interest due to their effective light emission and non-linear electronic properties.[6,12,13,14]

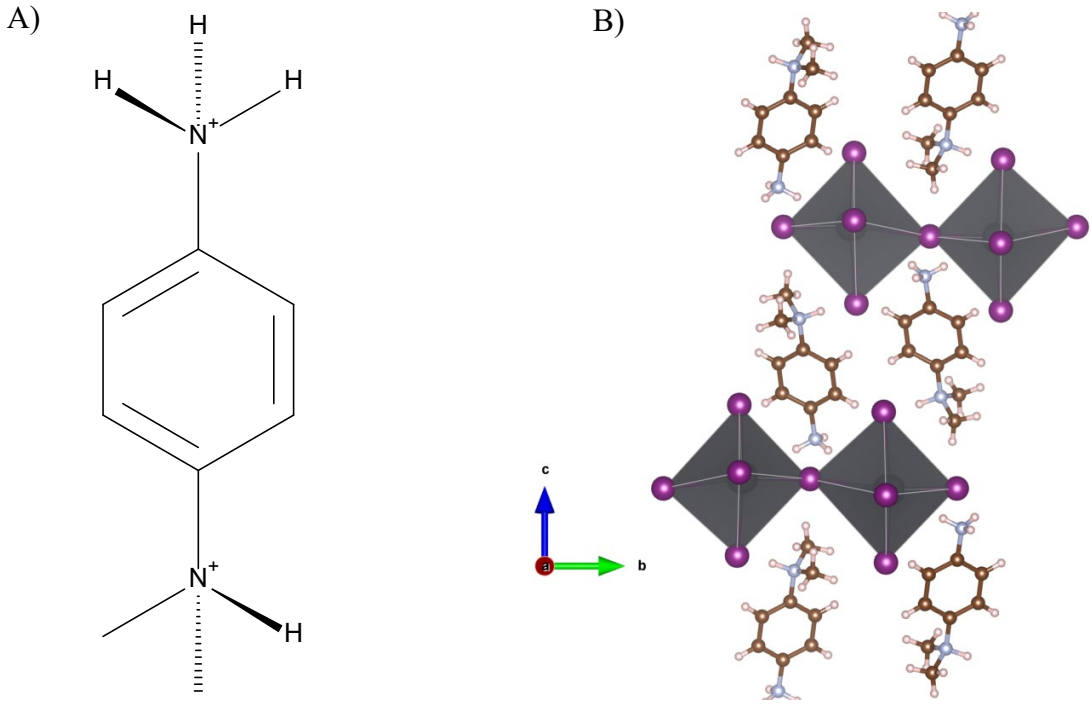

Figure 3.1. Structure of *$DPDAPbI_4$*. (A) Schematic of *DPDA* spacer and (B) Crystal structure at ambient pressure.

As detailed in Table 3.1, *$DPDAPbI_4$* has a monoclinic crystal structure with a $P2_1/n$ space group at ambient pressure and was first synthesized in 2017 by Hautzinger et al.[6] The *PbI_6* octahedra exhibit a corner-sharing octahedra mode (Figure 3.1b) and this particular HOIP is isostructural.[6] As seen by the structure (Figure 3.1a), the *DPDA* spacer consists of a phenyl ring with two

ammonium ligands (NH^+ and NH_3^+) attached in the *para* position, where NH^+ has two additional methyl groups attached.[6]

Table 3.1. Crystallographic parameters of *DPDAPbI₄* under ambient conditions.[6]

Parameter	***DPDAPbI₄***
Crystal Structure	Monoclinic
Space Group	$P2_1/n$
T (K)	100(1)
a (Å)	6.417(2)
b (Å)	12.601(3)
c (Å)	21.734(5)
β (°)	96.832(7)
V (Å^3)	1744.9(8)

The two Pb-I-Pb bond angles of 167° and 177° (Figure 3.2) are both close to the ideal angle of 180° and greater than the values of 166° and 177° for the $PbBr_4$ analogue, whilst the Pb-I bond distances of 3.0158(8) (Å) and 3.3873(8) (Å) are much closer in range than those of the $PbBr_4$ analogue. These larger angles are a result of the deep penetration of the *DPDA* cations into the PbI_6^{2-} octahedra spaces (Figure 3.1b). In particular, the NH_3^+ plane distance from the iodide plane is -1.110(2) (Å), a much greater penetration compared to the typical range of -0.7-0.7 (Å) for 2DN lead-iodide perovskites studied by Du et al.[6,13] Du et al. observed that the Pb-X-Pb ($X = I^-, Br^-, Cl^-$) bond angle decreases for penetration between -0.7-0.4 (Å), whilst penetration beyond 0.7 (Å) increases the Pb-X-Pb bond angle.[13] In the case of *DPDAPbI₄*, the greater penetration results in an increase in the H-I distance, thus weakening the hydrogen bond interaction and increasing Pb-I-Pb bond angles.[6,13]

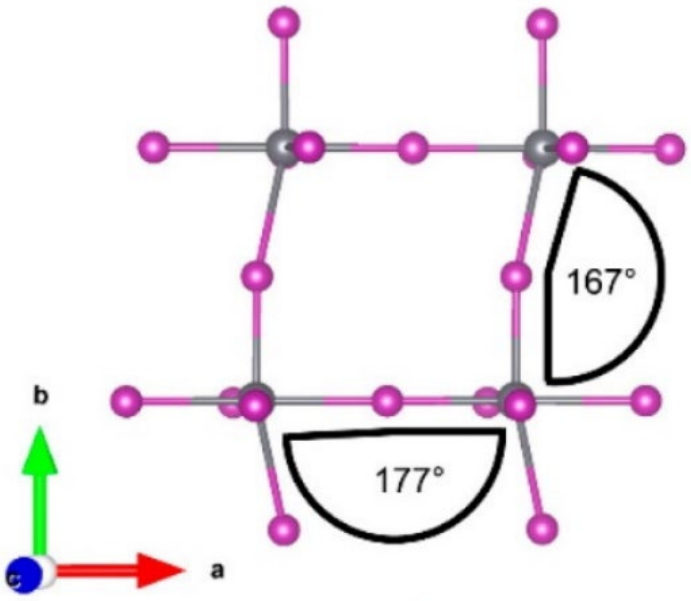

Figure 3.2. *DPDAPbI₄* Pb-I-Pb bond angles along *c* axis where grey balls represent Pb, and pink balls represent I.[6]

As seen by the UV-Vis absorption spectrum of *DPDAPbI₄* (Figure 3.3A), the main excitonic peak occurs around 2.37 eV and is significantly redshifted in comparison to previously studied 2DN lead-iodide perovskites.[6] This redshift is a result of the increased Pb-I-Pb bond angles in the lead-iodide octahedra, which leads to increased orbital overlap in the lead and iodide LUMO, thus leading to a conduction band of lower energy and decreasing the exciton energy, as previously shown by Amat et al. in 2017 during their study on band gap tuning of *MAPbI₃* and *FAPbI₃*.[6,15] The PL spectrum of *DPDAPbI₄* (Figure 3.3A) also shows a broad peak at around 537 nm under ambient conditions attributed to the emission of free excitons (FE), as indicated by the relatively weak shift of the emission relative to the excitonic absorption peak.[6] Temperature-dependent PL spectrum (Figure 3.3B) showed that the intensity of the free exciton peak increased as the temperature decreased, along with the onset of a new broad redshifted low energy peak.[6] This new peak is attributed to the low-temperature emission of self-trapped excitons (STE), and has previously been reported in 2DN lead-bromide perovskites but not in 2DN lead-iodide

perovskites.[6,16] A strong correlation between octahedral distortions and the emission of STEs has been previously shown, and thus it is not surprising that *DPDAPbI₄* exhibits this broad emission at low temperatures.[6,16]

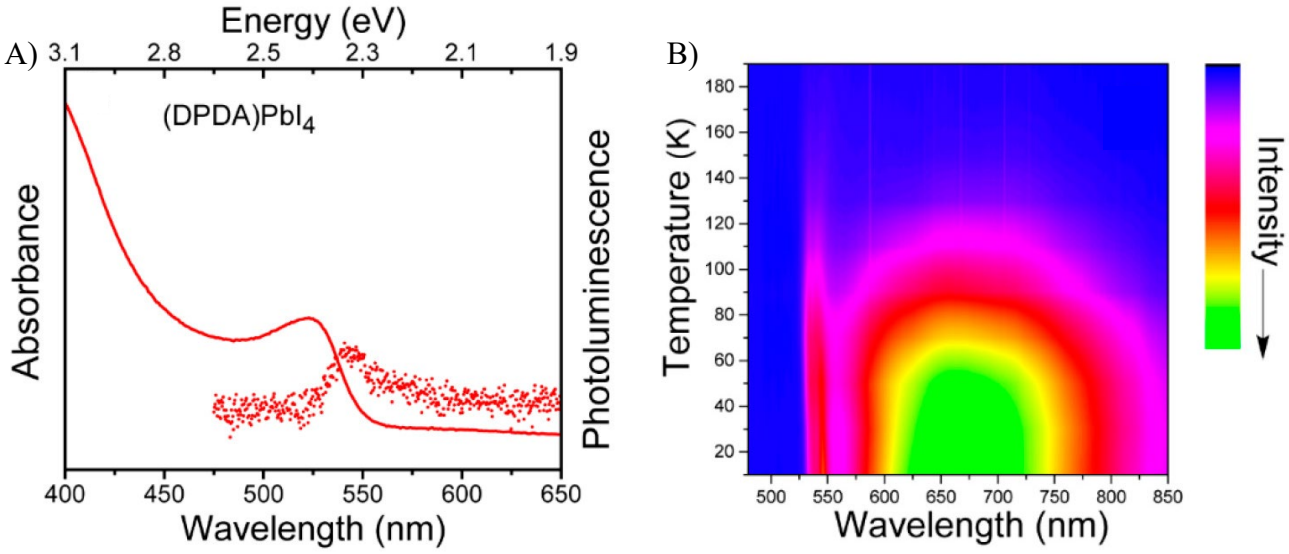

Figure 3.3. (A) Absorbance (line) and PL (scatter) spectra of *DPDAPbI₄* under ambient conditions. (B) Temperature-dependent PL spectrum of *DPDAPbI₄*.[6]

The density functional theory (DFT) calculated partial density of states (PDOS) of *DPDAPbI₄* (Figure 3.4) indicates that the major contribution to the valence band maximum (VBM) comes from iodide and the major contribution to the conduction band minimum (CBM) comes from the lead-iodide bonds.[6] Contributions from the DPDA spacer are observed for the near-edge conduction band, suggesting that the properties of DPDA might contribute to the electronic structure of *DPDAPbI₄*.[6]

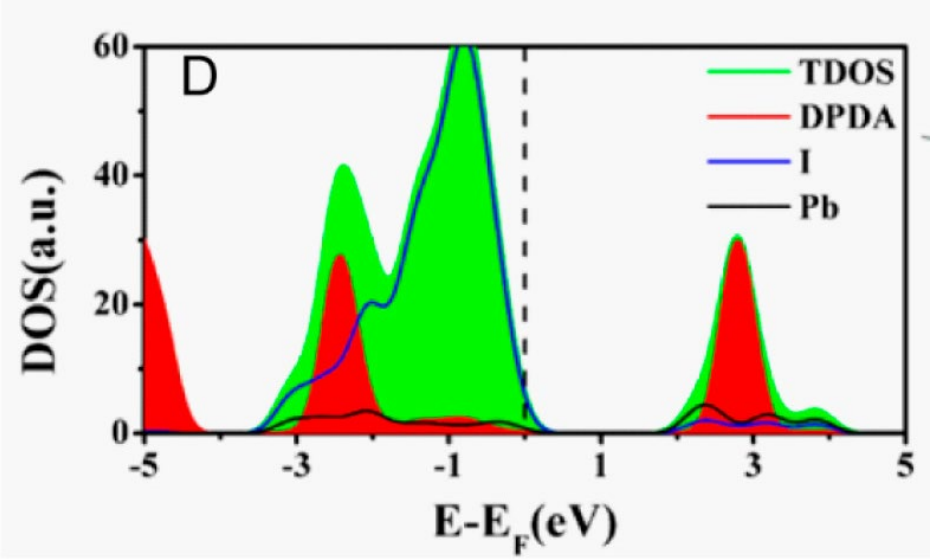

Figure 3.4. Partial Density of States (PDOS) of *DPDAPbI₄*.[6]

The rigidity of the organic spacer in 2D HOIPs can play a significant role in optimizing the optoelectronic properties for use in various applications, including solar cells. The DPDA dication spacer is of particular interest given its high rigidity and deep insertion into the lead-halide octahedral spaces, leading to enhanced octahedra distortions. These results coupled with the intriguing photoluminescent properties at ambient pressure make *DPDAPbI₄* a highly promising candidate for HP studies, with the ideal goal of permanently changing the optoelectronic properties, particularly the bandgap, by achieving irreversible pressure-induced modifications. Studying the changes to both the structure and optoelectronic properties at HP of *DPDAPbI₄* can provide valuable insights into the impact of rigid spacers in inducing modifications to the *PbI₆* octahedra and how the deep insertion of the spacer can modify the hydrogen bonds between the NH_3^+ groups and the iodine. Furthermore, understanding the behavior of *DPDAPbI₄* at HP can also provide a basis for the study of other 2D lead-iodide perovskites with highly rigid organic spacers.

In this chapter, the behavior of $DPDAPbI_4$ was probed at HP. Vibrational spectroscopy was used to provide a preliminary characterization of a possible phase transition and the hydrogen bonding between the NH_3^+ group of the *DPDA* organic spacer and the iodide of the PbI_6 octahedra. X-ray diffraction measurements at HP provide confirmation of the phase transition and help to characterize the compressibility upon compression. Furthermore, analysis of the Rietveld refinement of the 1D powder patterns provides further evidence of the phase transition and also offers valuable insights into the octahedral distortion enhancement at HP. The optoelectronic properties were probed at HP through photoluminescence, used to examine the excitonic and bandgap behavior upon compression, and UV-Vis Absorption measurements, used to provide a direct measurement of the bandgap change at HP. This work represents the first HP study on $DPDAPbI_4$ and builds upon the previous temperature-based study conducted by Hautzinger et al.[6]

3.2 Synthesis and Experimental Details

The synthesis of $DPDAPbI_4$ was performed by Matthew Hautzinger from Dr. Song Jin's group at the University of Wisconsin-Madison. The high sensitivity of $DPDAPbI_4$ to light resulted in slight modifications for the sample loading for the Raman measurements. $DPDAPbI_4$ powder was loaded into the gasket along with the ruby and KBr to help avoid laser damage due to the high fluorescence of the ruby ball. No pressure transmitting medium (PTM) was required for Raman measurements due to the softness of the sample. Calibration was achieved using neon emission lines and a 1200 l/mm grating was used. A red excitation wavelength (λ = 780 nm) was used due to the large luminescence from the sample. For FTIR measurements, $DPDAPbI_4$ powder was loaded into the gasket along with the ruby and KBr to reduce laser damage and no PTM. *In-situ* synchrotron X-ray diffraction (XRD) were performed remotely at the 16-BMD and 16-IDB HPCAT beamlines

at the Advanced Photon Source (APS). Calibration was done using a 20 keV (λ = 0.6199 Å) X-ray beam along with CeO_2 powder. The packed *DPDAPbI₄* powder sample was loaded into the gasket chamber along with ruby balls for initial pressure gauging, fine gold powder for *in-situ* measurements, and silicone oil as the PTM. The Photoluminescence and UV-Vis absorption measurements were performed using single crystals with silicone oil as the PTM. To avoid laser damage of the sample, the ruby was loaded near the edge of the gasket to separate it from the single crystal.

3.3 Results and Discussion

3.3.1 Vibrational Spectroscopy

Raman and FTIR Spectroscopy were employed to measure and identify various vibrational modes within the DPDA spacer. This allowed for the characterization of structural changes and possible phase transitions in *DPDAPbI4*. Among the numerous vibrational modes observed, this work primarily delves into those that offer significant insight into intriguing pressure-induced structural modifications and phase transitions. The Raman and FTIR spectra at ambient pressure can be seen in Figure 3.5.

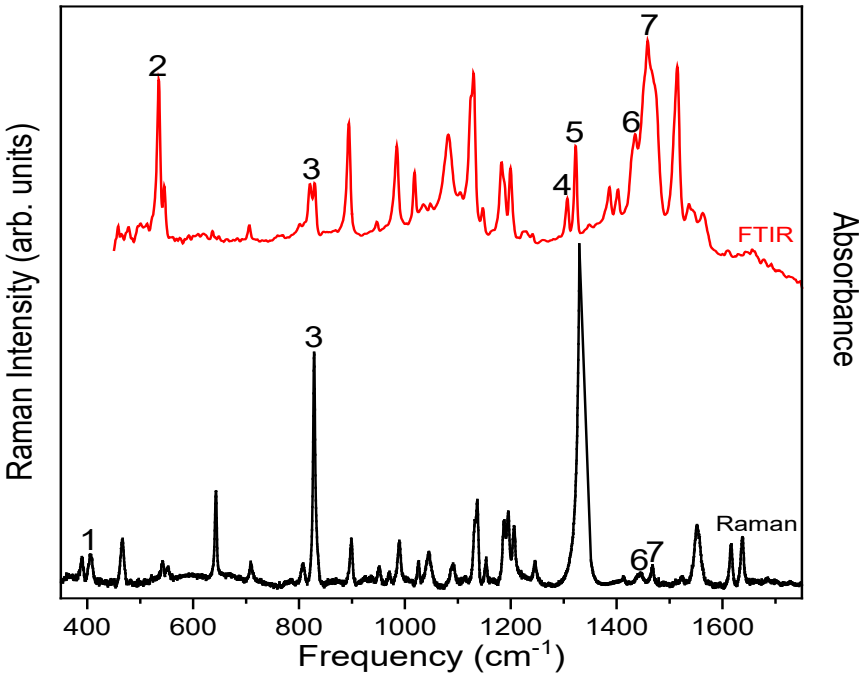

Figure 3.5. Ambient pressure vibrational spectra of *DPDAPbI₄*.

The observed vibrational modes for both the Raman and FTIR measurements were assigned using DPDA calculations in its vapor phase in vacuum compared with the ambient pressure spectra (0 GPa). Table 3.2 and Figure 3.6 display the assignment of the characteristic peaks and schematics of the modes, respectively.

Table 3.2. Characteristic Peak Assignment for DPDA Spacer.

Peak	Calculated (cm^{-1})	Raman (cm^{-1})	FTIR (cm^{-1})	Assignment
1	450	405		N-CH_3 scissoring
2	551		535	Ring bending
3	845	828	834	Ring CH puckering
4	1329		1318	Ring breathing I
5	1353		1335	Ring breathing II
6	1509	1440	1430	CH_3-NH rocking
7	1535	1465	1459	NH_3 bending

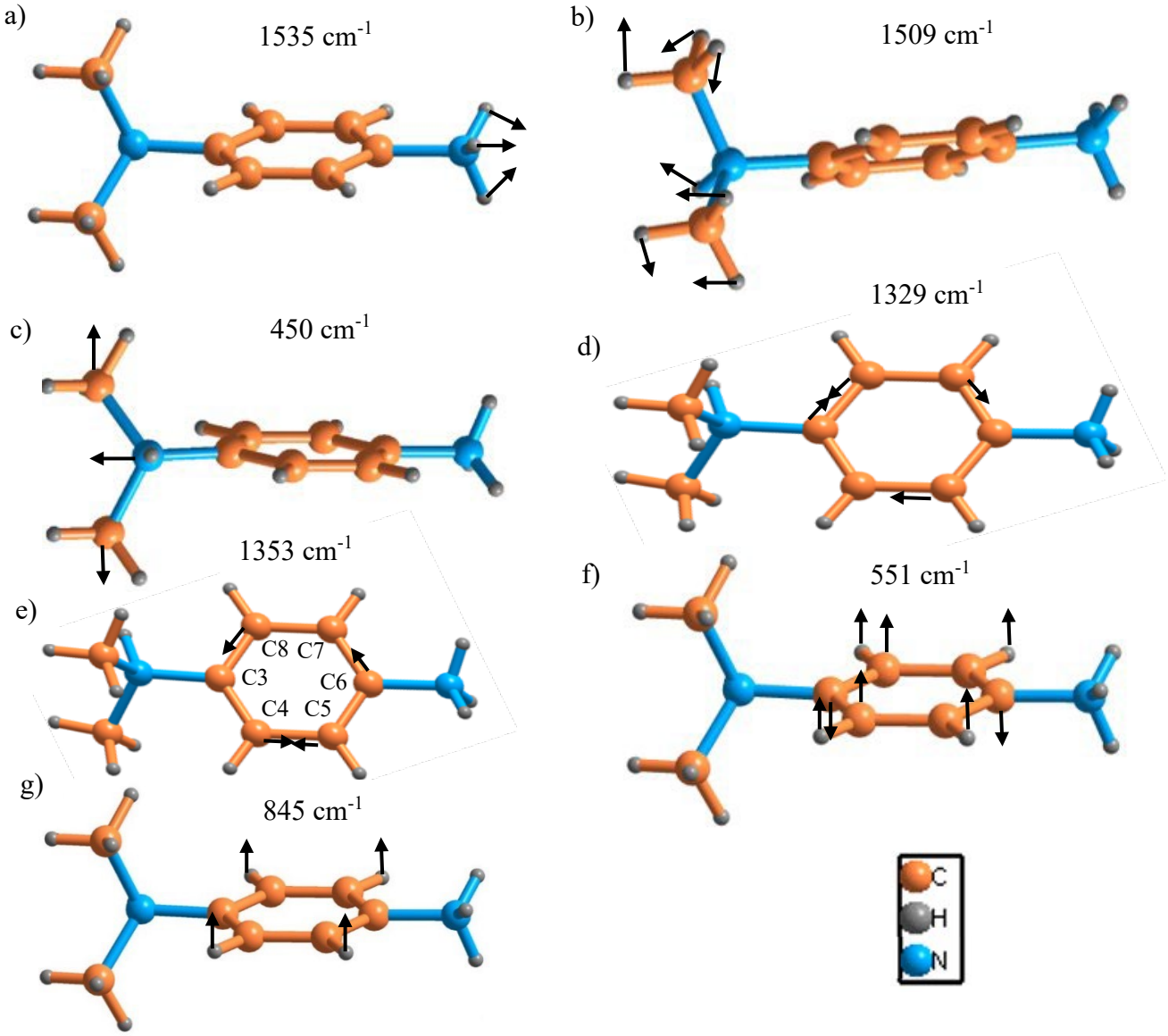

Figure 3.6. DPDA Spacer Vibrational Mode Schematics. a) *NH_3* bending, b) *CH_3 – NH* rocking, c) *N – CH_3* scissoring, d) ring breathing I, e) ring breathing II, f) ring bending, and g) *CH* ring puckering.

A peak splitting in the Raman spectra of the N-*CH_3* scissoring mode (Figure 3.7) is observed, indicating a possible phase transition around 1.5 GPa. Initial broadening is observed up to 2.64 GPa with the two peaks being unresolvable, followed by a resolvable doublet upon further compression beyond 2.64 GPa. Furthermore, the observed blueshift of the ring bending mode (Figure 3.8) provides further evidence of the phase transition with a greater shift experience

beyond 1.5 GPa. The observed splitting likely indicates a pressure-induced enhancement in both the octahedral distortion and the N–H···I hydrogen bonding interactions, with the latter most likely leading to shortening of the Pb-I bond lengths upon compression, which in turn would further suggest a bandgap reduction.

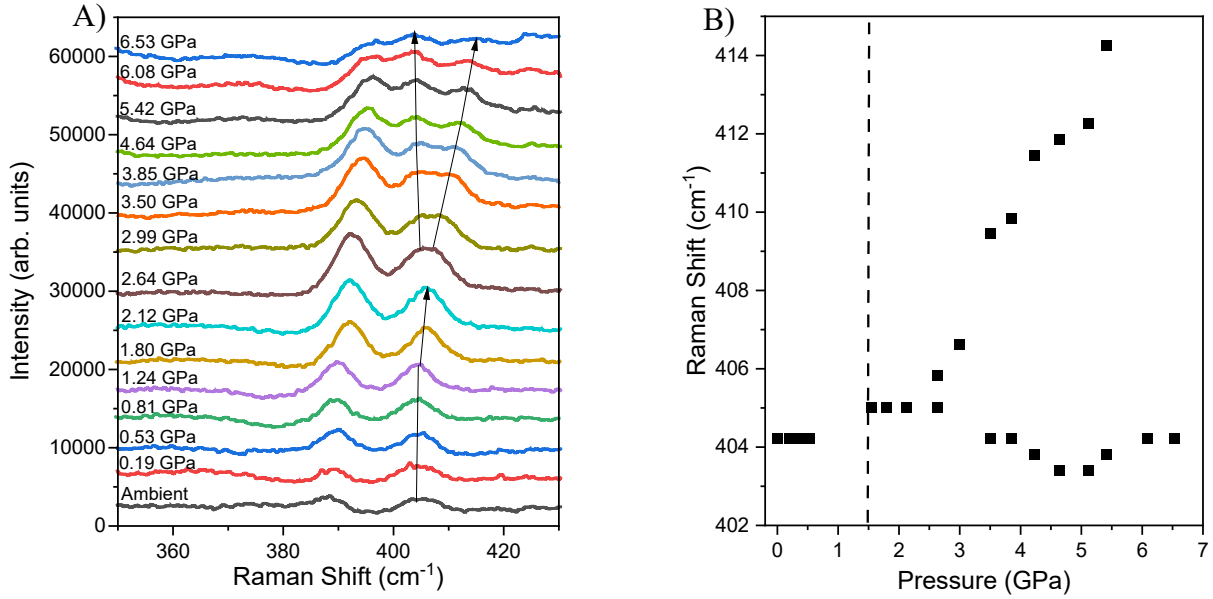

Figure 3.7. Raman spectra of N-CH_3 scissoring mode. (A) spectra upon compression and (B) Raman shift as a function of pressure.

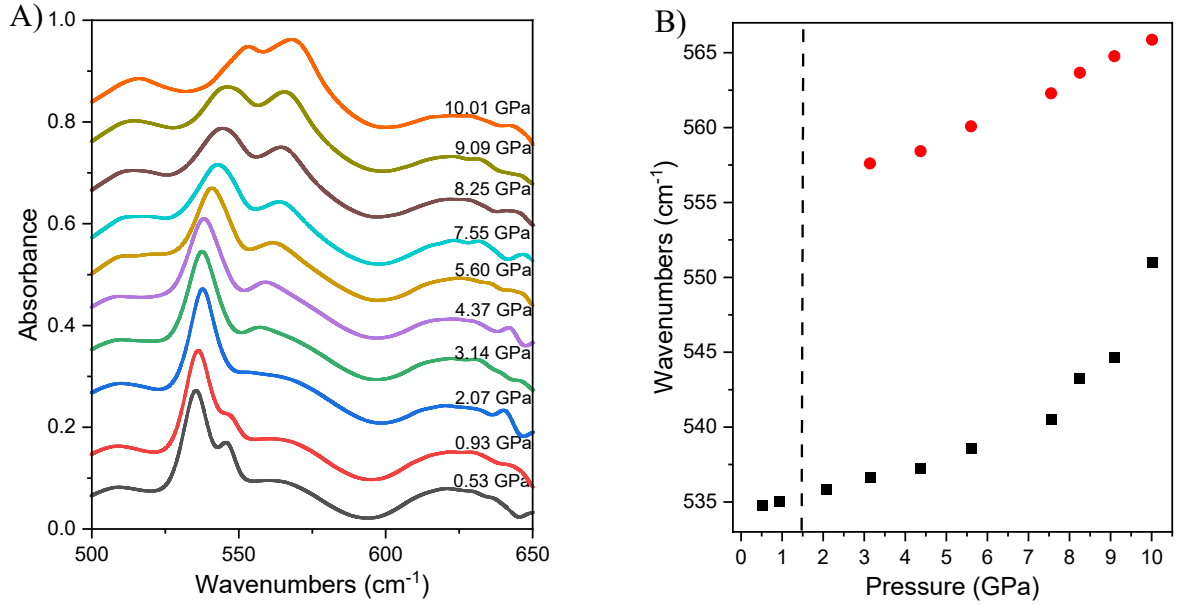

Figure 3.8. FTIR spectra of the ring bending mode. (A) spectra upon compression and (B) wavenumbers as a function of pressure.

The IR and Raman spectra of the NH_3 bending and CH_3-NH rocking modes all exhibit a redshift upon compression (Figure 3.9), thus providing evidence of the N–H···I hydrogen bonding interactions. These interactions are believed to be H_N---I bonding occurring between the organic *DPDA* spacer cations (NH_3^+) and the iodide in the inorganic PbI_6 octahedra, with similar interactions having been previously observed in PMA_2PbI_4.[17] Furthermore, the more significant shift beyond 1.5 GPa provides further evidence of the proposed phase transition and indicates an enhancement in the hydrogen bonding interactions upon compression.

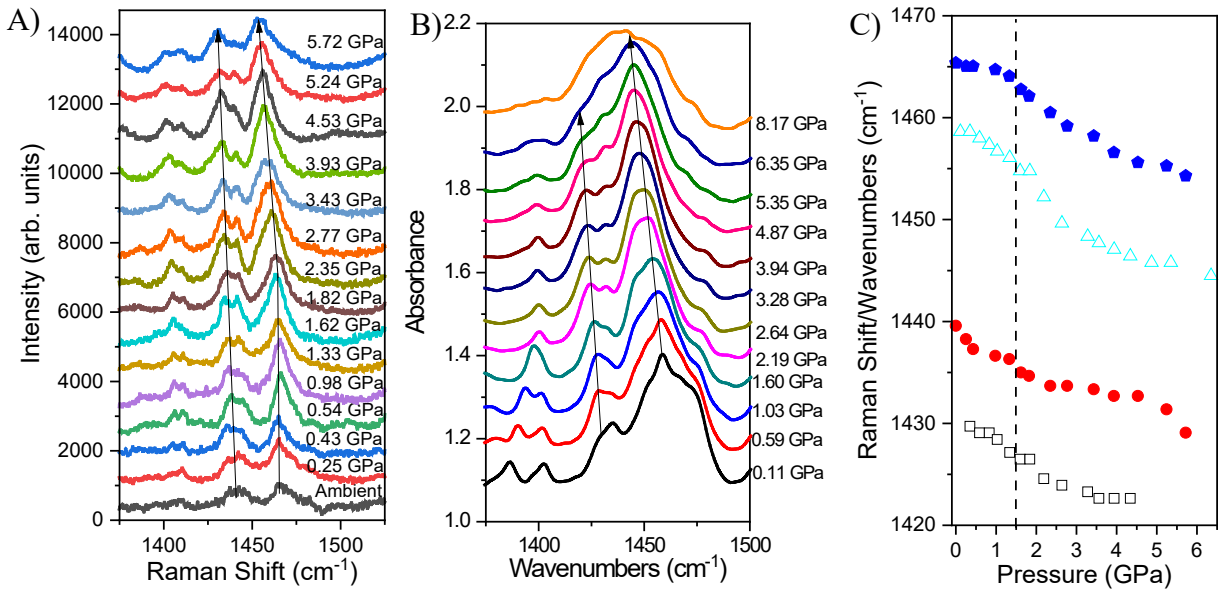

Figure 3.9. Raman and FTIR spectra of the NH_3 bending and CH_3-NH rocking modes. (A) Raman spectra upon compression, (B) FTIR spectra upon compression, and (C) Raman shift of NH_3 bending (blue pentagons), CH_3-NH rocking modes (red circles) and frequency of NH_3 bending (open blue triangles), CH_3-NH rocking modes (open black squares) as functions of pressure.

The ring CH puckering mode also experienced a redshift upon compression with a more significant shift observed in the low-pressure region (>1.5 GPa) followed by a more constant shift upon further compression beyond 1.5 GPa (Figure 3.10). Interestingly, the ring breathing mode I exhibits a blueshift upon compression following a similar pattern to the ring CH puckering mode with a more significant shift observed in the low-pressure region followed by a constant shift

beyond 1.5 GPa (Figure 3.10). These results provide yet further evidence of the proposed phase transition around 1.5 GPa.

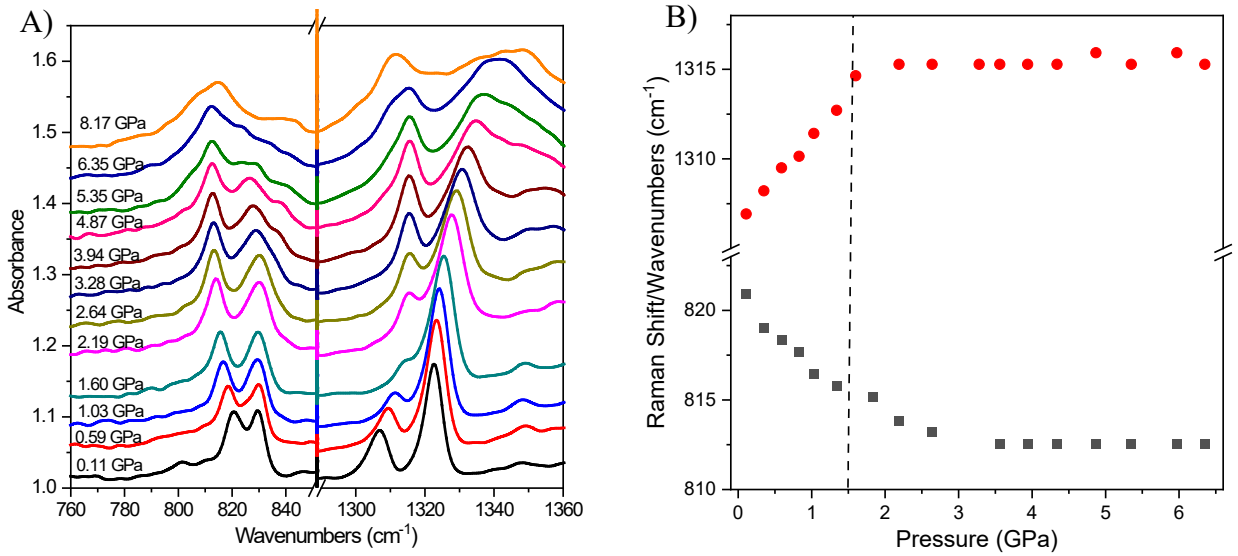

Figure 3.10. FTIR spectra of the ring CH puckering and ring breathing I modes. (A) spectra upon compression and (B) frequency of ring CH puckering (black squares) and ring breathing I (red circles) modes as functions of pressure.

Upon further compression beyond 5 GPa amorphization of the *DPDA* spacer becomes apparent evidenced by the broadening of the peaks in both the Raman and IR spectra. Furthermore, upon decompression both the Raman and IR spectra were found to be identical to the pre-compression state, suggesting reversible structural modifications and no metastable changes occurred.

3.3.2 X-Ray Diffraction

To help confirm and provide further evidence of the pressure-induced structural modifications in *DPDAPbI₄ in-situ* synchrotron XRD measurements were performed at HP. At ambient pressure, *DPDAPbI₄* was identified as having a monoclinic crystal structure with a $P2_1/n$ space group. The refined lattice parameters are shown in Table 3.3 in comparison to the previous values obtained by

Hautzinger et al.[6] *DPDAPbI₄* was also determined to have a slightly distorted PbI_6 octahedra where the *c* parameter is nearly 3 times the length of the *a* parameter and twice as long as the *b* parameter.

Table 3.3. Refined unit cell parameters of *DPDAPbI₄* at ambient pressure for study in comparison with previous work by our collaborators.

Parameter	This study	Collaborators
T (K)	300	100(1)
a (Å)	6.452	6.417(2)
b (Å)	12.671	12.601(3)
c (Å)	21.897	21.734(5)
β (°)	97.012	96.832(7)
V (Å^3)	1776.6	1744.9(8)

As shown in Figure 3.11, majority of the diffraction peaks were found to shift to higher 2θ angles upon compression, indicating a lattice contraction. Furthermore, the lack of significant changes suggests that the proposed phase transition is likely isostructural. The broadening of the peaks above 5.5 GPa indicates the onset of amorphization, in good agreement with the vibrational spectroscopy measurements.

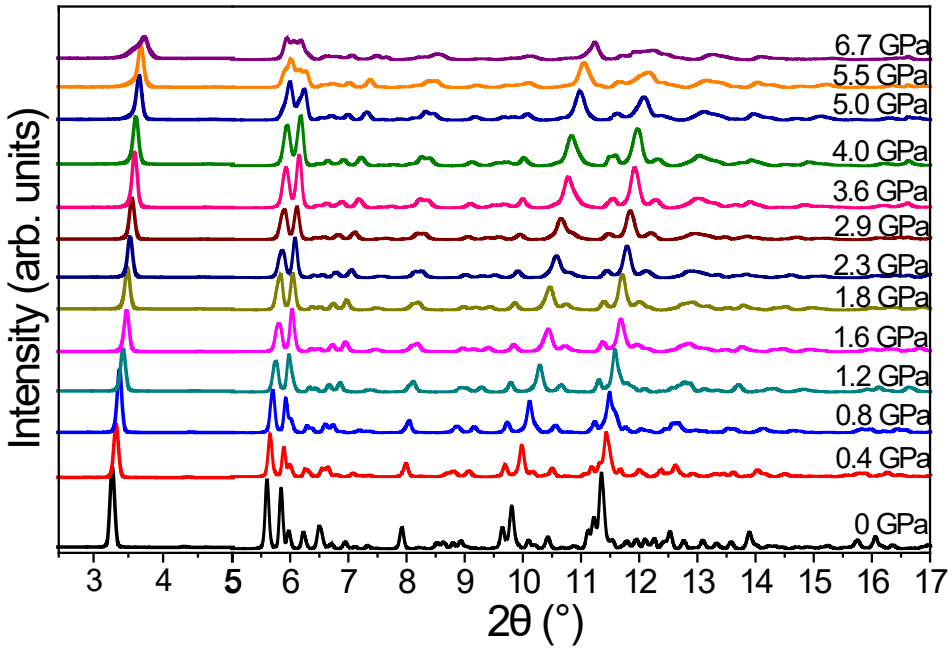

Figure 3.11. XRD patterns of *DPDAPbI₄* upon compression.

Rietveld refinements of the 1D XRD patterns were performed using the initial $P2_1/n$ crystal structure upon compression to around 5.5 GPa. Upon further compression the onset of amorphization made refinement much more challenging. The Rietveld refinement at 3.59 GPa can be seen in Figure 3.12. Upon decompression the recovered state was found to be identical to the pre-compression, thus once again indicating reversibility consistent with the vibrational spectroscopy measurements.

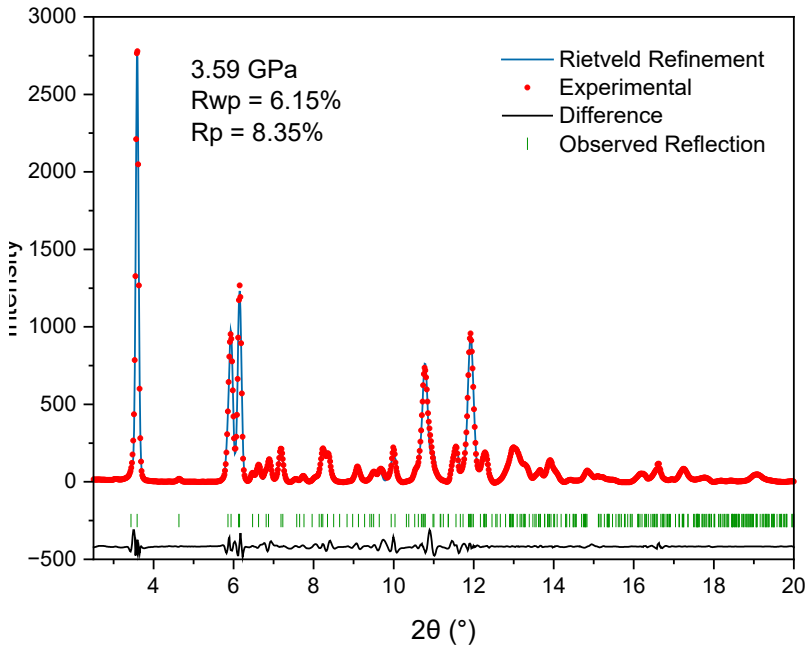

Figure 3.12. Rietveld refinement for 3.59 GPa.

Upon plotting the refined lattice parameters as functions of pressure (Figure 3.13 and Table 3.4), an anisotropic compression along the *c* direction was determined evidenced by the greater compressibility in comparison to the *a* and *b* parameters. This was likely a result of the sandwich structure resulting from the rigid organic spacers and the inorganic octahedra. Furthermore, all parameters were found to slow slight discontinuities at around 1.5 GPa, providing confirmation of the phase transition. The space group was also found to be unchanged for all refinements, thus also confirming the phase transition as isostructural.

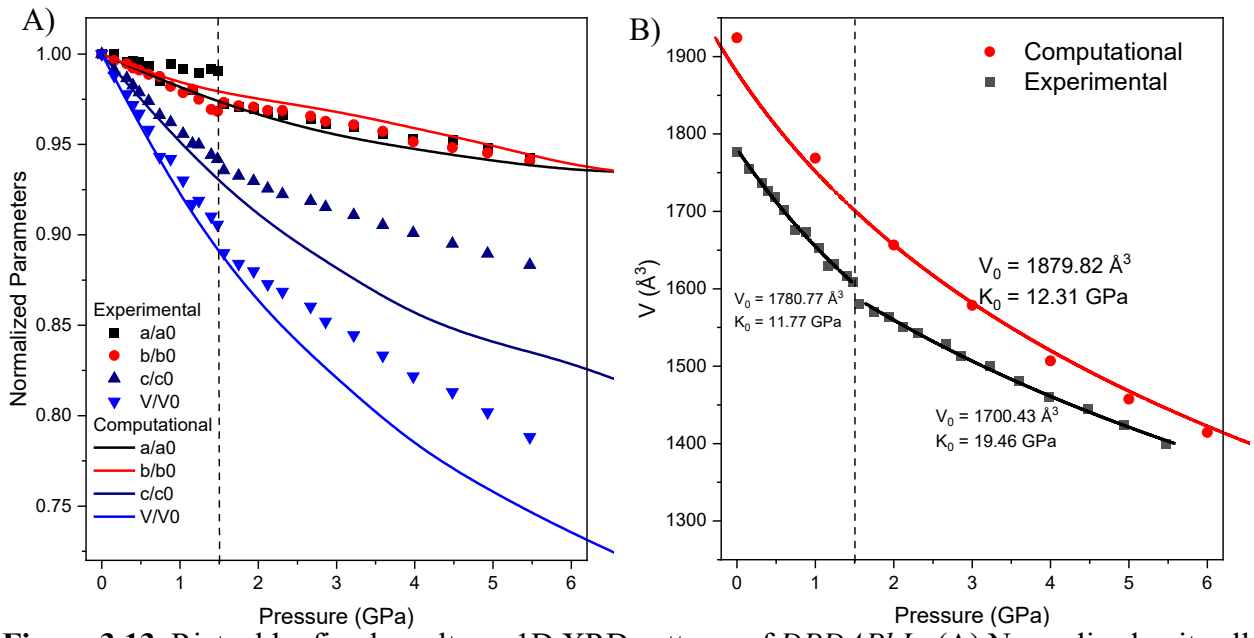

Figure 3.13. Rietveld refined results on 1D XRD patterns of *DPDAPbI₄*. (A) Normalized unit cell parameters as functions of pressure and (B) unit cell volume as a function of pressure fitted with the 2nd order Birch-Murnaghan equation of state (solid black line).

Table 3.4. Refined lattice parameters of *DPDAPbI₄* at HP.

Pressure (GPa)	a (Å)	b (Å)	c (Å)	β (°)	V (Å³)
0	6.4519	12.6705	21.8965	97.012	1776.6243
0.4	6.4267	12.5715	21.5148	96.6164	1726.6737
0.74	6.3573	12.5142	21.1571	95.4403	1675.6035
1.16	6.3224	12.4232	20.8121	94.5832	1629.4476
1.56	6.2722	12.3308	20.4878	93.8124	1581.0456
1.75	6.2618	12.3082	20.4221	93.7903	1570.5188
2.31	6.2361	12.2743	20.1997	93.6549	1543.0163
2.86	6.2027	12.1992	20.042	93.5566	1513.6167
3.59	6.1681	12.1289	19.8255	93.5528	1480.3401
3.98	6.1492	12.0556	19.7288	93.4807	1459.8433
4.93	6.1153	11.9776	19.4789	93.1579	1424.5971
5.47	6.0804	11.9209	19.342	92.8536	1400.244

Upon fitting the unit cell volumes with the 2nd order Birch-Murnaghan equation of state (Figure 3.13) for both phases, once again a slight discontinuity was observed around 1.5 GPa providing further evidence of the phase transition. It was determined that V_0 = 1780.77 Å³ and K_0 = 11.77 GPa for phase I and V_0 = 1700.43 Å³ and K_0 = 19.46 GPa for phase II. These results suggest a

greater bulk modulus for phase I, thus indicating greater compressibility in phase I compared to phase II.

3.3.3 Photoluminescence

To probe the effects of HP on the excitonic structure within *DPDAPbI₄*, HP PL measurements were conducted using 360 nm UV excitation. The PL spectra upon compression along with the optical images is shown in Figure 3.14. *DPDAPbI₄* was found to have a slightly asymmetric emission profile at ambient pressure with a peak at around 538 nm, attributed to the emission from free excitons (FE), which have been frequently observed is previously studied 2D HOIPs.[6] Upon compression the peak is found to broaden, attributed to the emission from self-trapped excitons (STE), which have been observed previously in (3AMPY)GeI_4.[18,19] Furthermore, the intensity of the FE peak is found to increase upon compression to 1.49 GPa at which point the intensity is around 3-4 times greater than that at ambient pressure. This is subsequently followed by a gradual decrease in intensity until eventual quenching at 5.56 GPa. These changes are further evidenced by the optical images showing a clear change from bright green emission at low-pressure to even greenish-red and eventual black upon compression to 5.70 GPa.

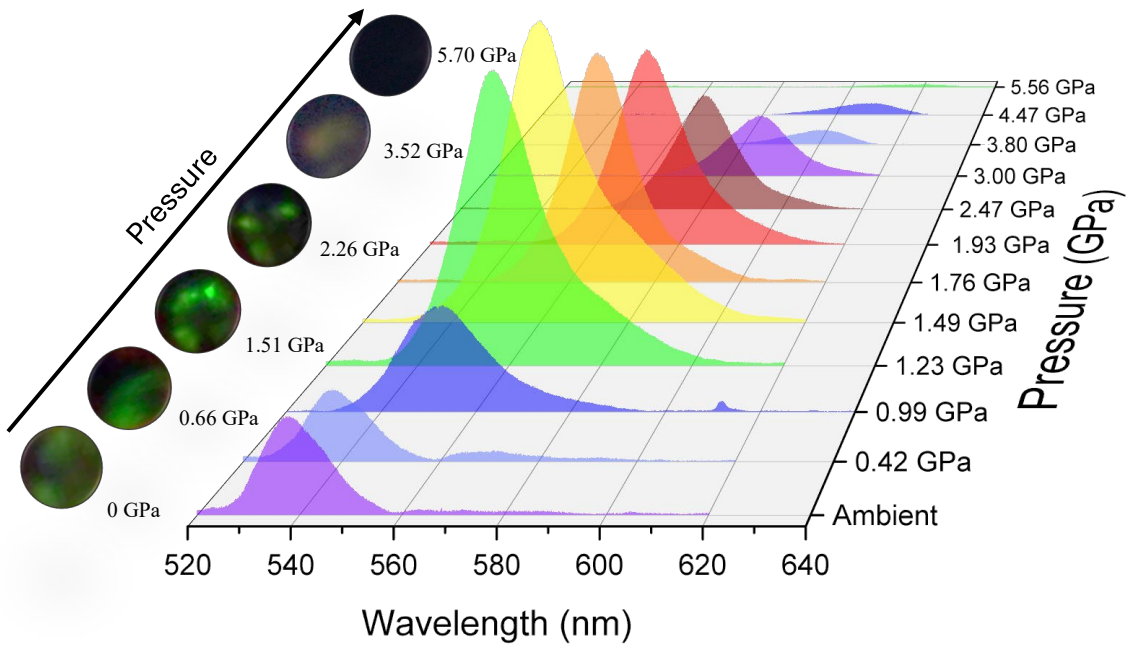

Figure 3.14. PL measurements of *DPDAPbI₄* at selected pressures with optical images.

A broadening of the STE peak was observed upon compression to 1.23 GPa followed by a narrowing of the STE peak and increased domination of the FE peak until eventual full dominance beyond 3.29 GPa. The schematics of the emission profiles at 1.49 and 3.29 GPa can be seen in Figure 3.15. This broad STE emission at low-pressure has also been previously reported at low-temperature by our collaborators, thus indicating strong correlation between the pressure and temperature-based measurements. The observed changes in the STE and FE peaks likely result from changes in the octahedral distortion upon compression, which have previously reported in other 2D HOIPs.[6,16]

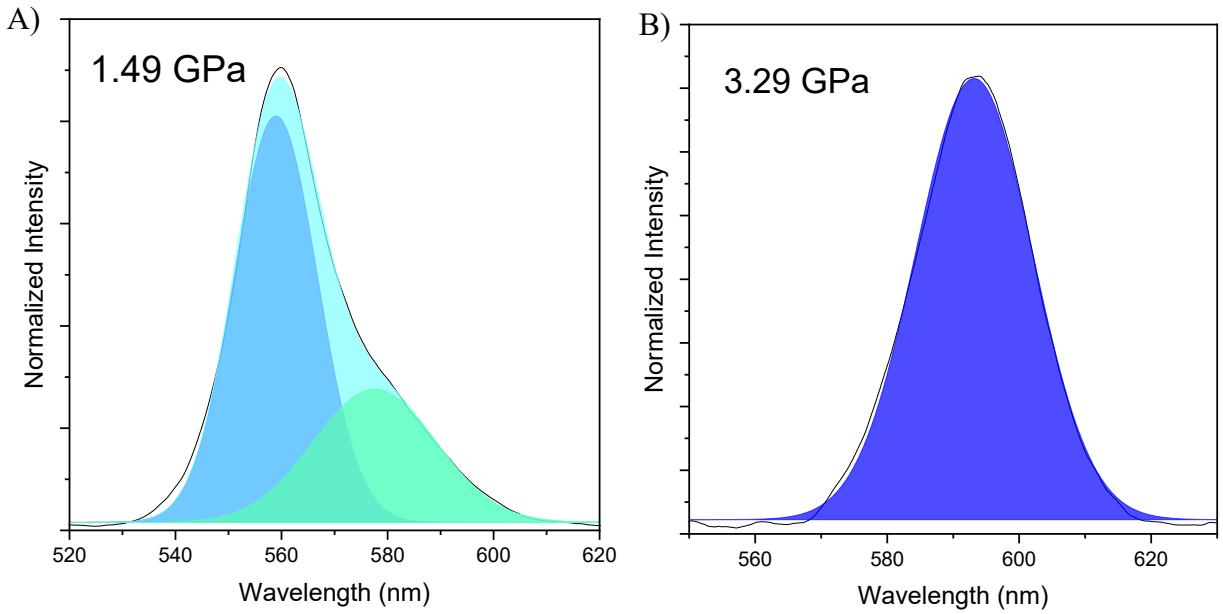

Figure 3.15. PL emission profiles showing both free (blue) and self-trapped (green) excitons in *DPDAPbI₄* at (A) 1.49 GPa and (B) 3.29 GPa.

A continuous redshift of the prominent FE peak is observed upon compression at a rate of 15.71 nm/GPa (Figure 3.16). This observed redshift likely indicates a bandgap reduction, which would suggest a shortening of the Pb-I bond lengths upon compression. Furthermore, the maximum PL intensity observed at 1.49 GPa in phase I provides further evidence of the phase transition at 1.5 GPa. These results are once again evidenced by the optical images shown in Figure 3.14.

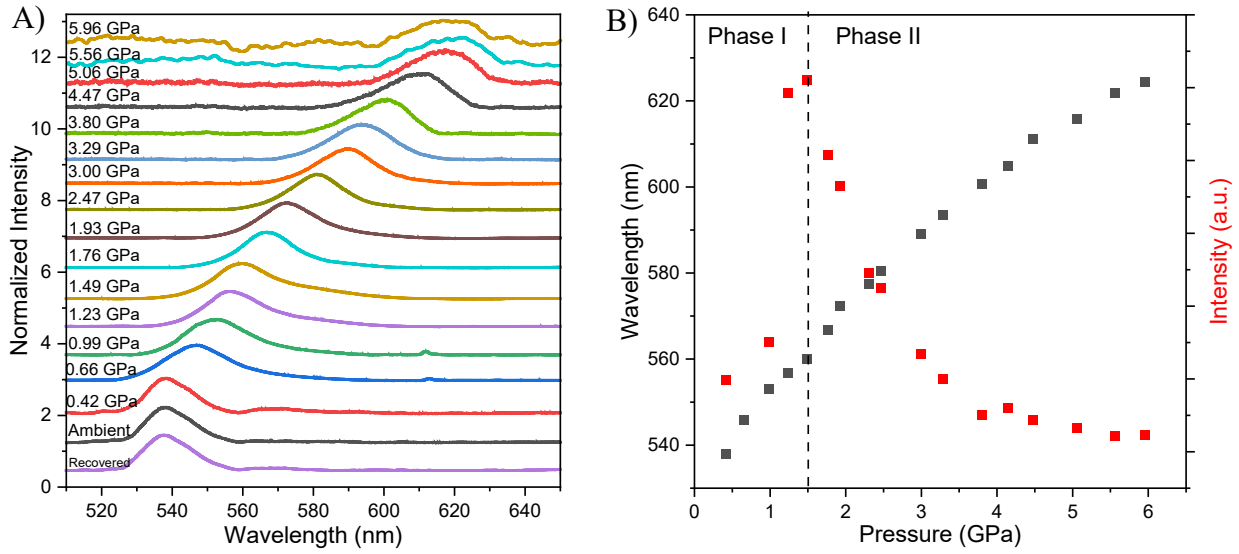

Figure 3.16. PL of *DPDAPbI₄* at HP. (A) normalized spectra upon compression and (B) emission wavelength and peak intensity as functions of pressure.

Furthermore, upon decompression the PL peak profile and position were found to return to that of the pre-compression state (Figure 3.17), thus indicating reversible excitonic changes consistent with the reversible structural modifications highlighted by both the vibrational spectroscopy and XRD measurements.

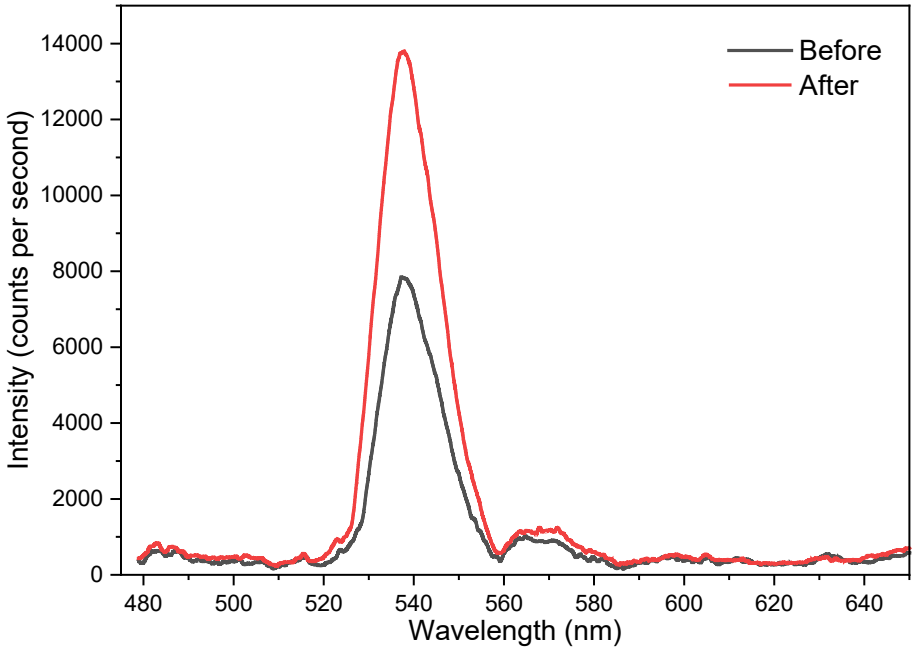

Figure 3.17. PL spectra of *DPDAPbI₄* before and after compression.

3.3.4 UV-Vis Absorption

To probe the effects of HP on the electronic structure of *DPDAPbI₄* and provide direct measurements of the bandgap behavior, UV-Vis absorption measurements were conducted at HP. As seen in Figure 3.18, a continuous redshift of the absorption edge is observed upon compression, indicating a bandgap reduction in good agreement with the HP PL measurements. This is further evidenced by the optical images which shows a yellow-orange crystal near ambient pressure. This is followed by a change to orange-red upon compression to around 2.5 GPa. Further compression results in a change to red around 6 GPa and eventual dark reddish-purple around 8 GPa. Furthermore, upon decompression the crystal was found to blueshift and eventually return to the pre-compression bright yellow color.

Upon performing Tauc analysis at ambient pressure, *DPDAPbI₄* was determined to have a direct bandgap of 2.26 eV, in good agreement with computational value of 2.103 eV and the previous value of 2.37 eV reported by Hautzinger et al.[6] One possible reason for the difference between the experimental value and the previously reported value is the use of thin films by Hautzinger et al, while this study used a slightly thicker single crystal.[6] Upon plotting the bandgap as a function of pressure (Figure 3.18) a bandgap reduction was confirmed from 2.26 to 1.87 eV upon compression to 8.84 GPa, once again in excellent agreement with the PL measurements. Furthermore, the bandgap was determined to be direct for all pressure points and upon decompression the bandgap was found to return to 2.25 eV. This result coupled with the optical images indicates reversible bandgap behavior, once again consistent with the vibrational spectroscopy, XRD, and PL measurements.

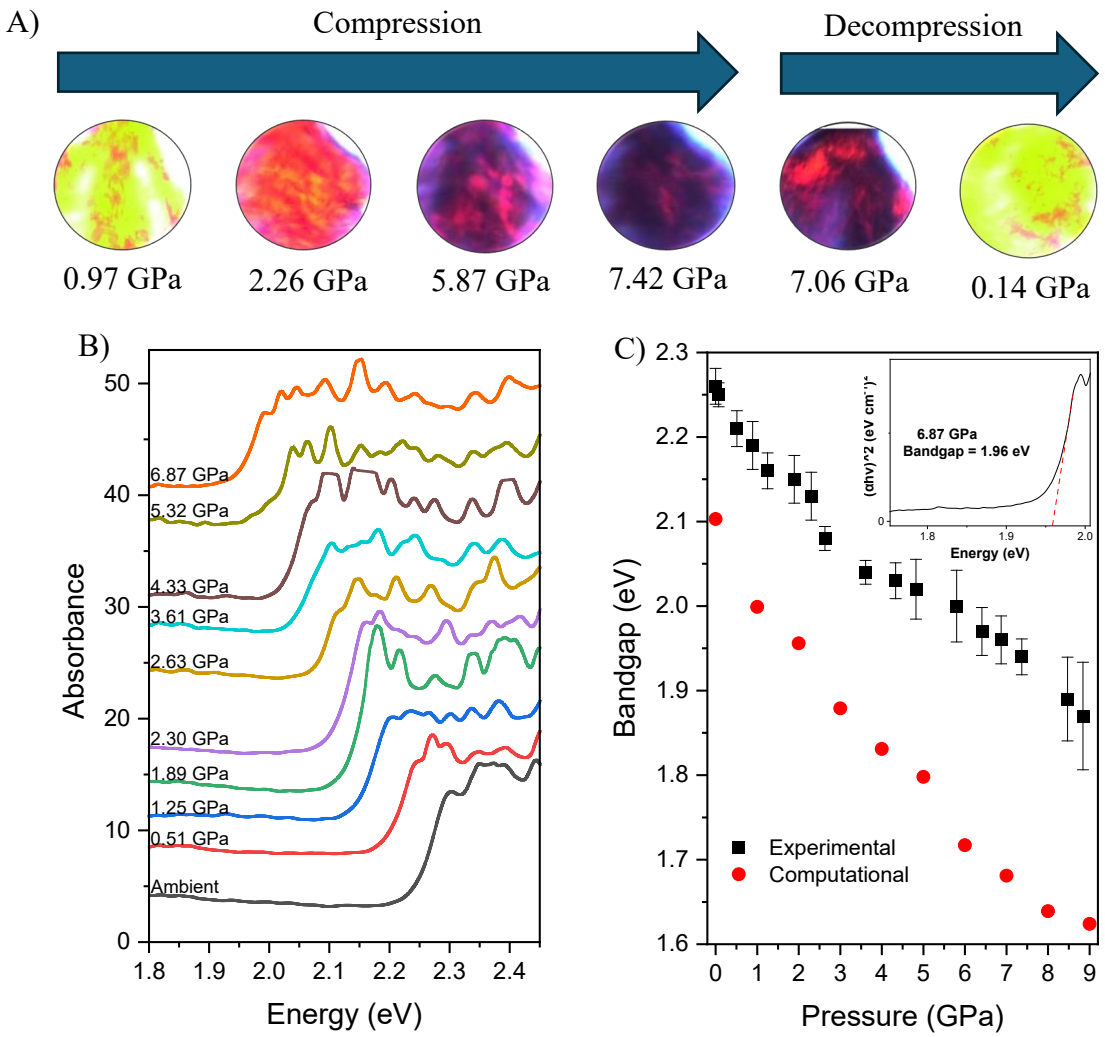

Figure 3.18. UV-Visible absorption of *DPDAPbI₄* at HP. (A) optical images at selected pressures for both compression and decompression, (B) absorbance spectra upon compression, and (C) bandgap as a function of pressure in comparison with computational values with Tauc plot at 6.87 eV in inset.

3.3.5 Comparison of Experimental and Computational Results

To develop a deeper understanding of the pressure-induced structural modifications on *DPDAPbI₄*, computations were performed on unit cell parameters and the unit cell volume (Figure 3.19). All parameters were found to decrease monotonically, an expected result as a single crystal structure and space group were assumed. Once again, the *c* parameter was found to exhibit the greatest compressibility, confirming the anisotropic compression along the *c* direction. Furthermore, the

computed bulk modulus of 12.31 GPa is around 4.59% greater than that of phase I and around 36.74% smaller than that of phase II. Given this, it can be confirmed that the greatest compressibility does indeed occur in phase I.

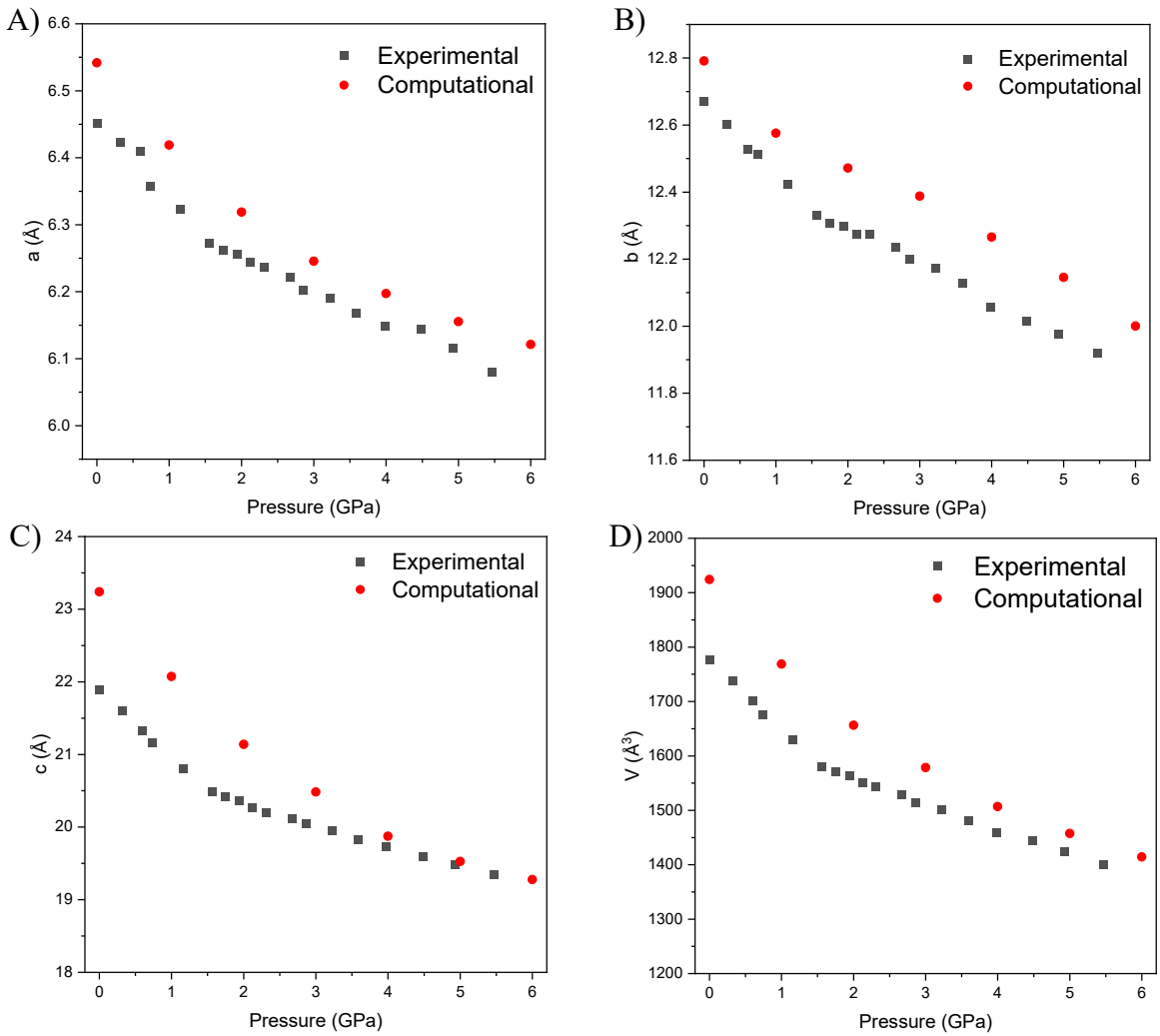

Figure 3.19. Experimental lattice parameters and cell volume in comparison to computational results as functions of pressure. (A) a parameter, (B) b parameter, (C) c parameter, and (D) unit cell volume.

Computational work was also performed to obtain the theoretical band structures and density of states (DOS) (Figure 3.20) to better understand the pressure-induced changes in the optoelectronic properties of *DPDAPbI₄*. As mentioned earlier, the computational bandgap value of 2.103 eV is in good agreement with the experimental value of 2.26 eV. As evidenced by the DOS calculations,

the valence band minimum (VBM) is mainly contributed by the I 5p orbitals while the conduction band maximum (CBM) is mainly contributed by the Pb 6p orbitals and the carbon of the DPDA spacer cations. While the experimental bandgap is greater than the computed bandgap at all pressures (Figure 3.18), they are good agreement at low-pressure. Furthermore, the VBM energy was found to increase at a slightly greater rate compared to the CBM energy (0.3335 eV/GPa vs. 0.2936 eV/GPa), thus indicating a faster reduction of the CBM and confirming the bandgap reduction upon compression. Continuous changes for the contributions at all pressures confirm the direct bandgap was maintained with no transition to an indirect bandgap, consistent with the experimental results.

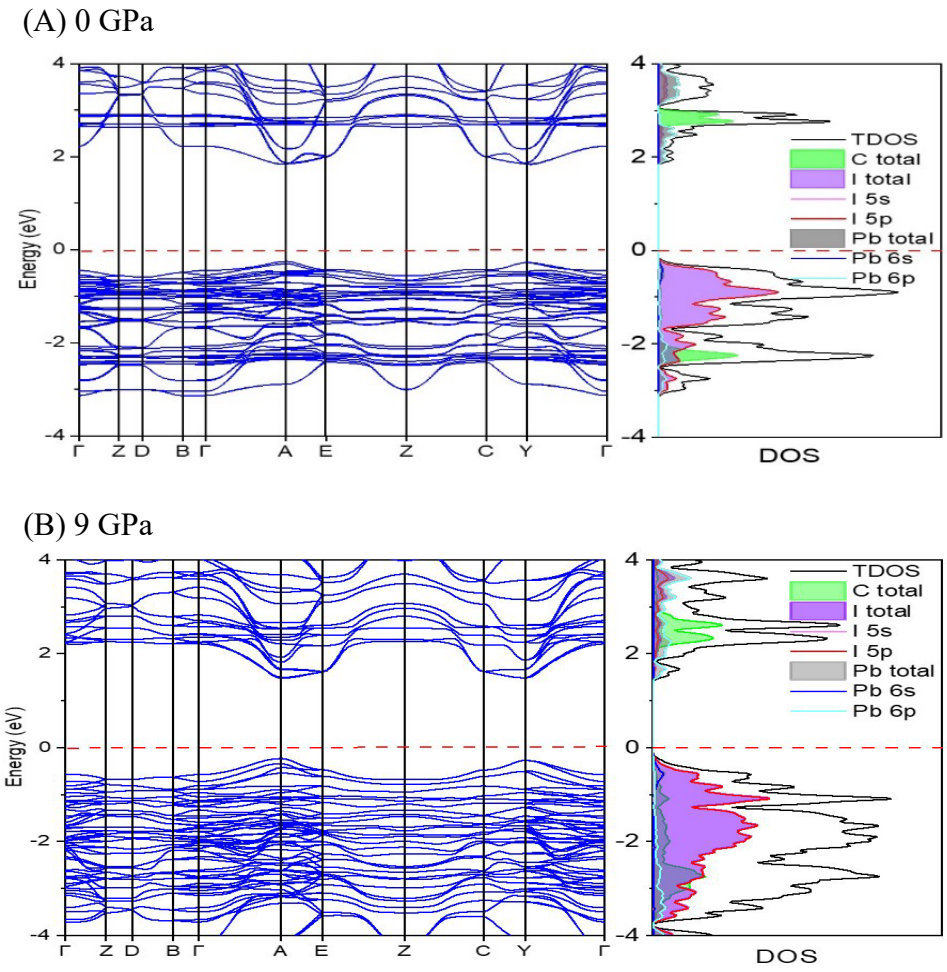

Figure 3.20. Computed band structures and DOS for *DPDAPbI₄* at (A) 0 GPa and (B) 9 GPa.

3.3.6 Significance of Results

Structural modifications have been identified by the vibrational spectroscopy measurements and the diffraction analysis. Furthermore, the PL measurements indicate these changes are likely influenced by changes in the octahedral distortion. Therefore, it is crucial to examine the distortion upon compression and in turn determine the structural origins behind the modifications and the mechanisms behind the pressure-induced optoelectronic properties of *DPDAPbI₄*.

To understand the effect of HP on the distortion of the PbI_6 octahedra computational distortion analysis was performed for both the bond length distortion (Δd) and the bond angle variance (σ) based on the methods used in previous studies.[8,20] The bond length distortion was calculated using equation 3.1, where d_i is the six individual Pb–I bond lengths and d is the average Pb–I bond length. The bond angle variance was calculated using equation 3.2, where θ_i is the individual I–Pb–I bond angles.

$$\Delta d = \sqrt{\frac{1}{6}\sum[\frac{d_i - d}{d}]^2} \tag{3.1}$$

$$\sigma = \sqrt{\sum_{n=12}^{i=1} \frac{(\theta_i - 90)^2}{11}} \tag{3.2}$$

As seen in Figure 3.21, an initial decrease in Δd is observed upon compression to around 1 GPa, indicating relaxation of the octahedral distortion at low-pressure. This initial decrease is in good agreement with the broadening of the STE PL peak at low-pressure, an intriguing result given that previous HP studies on other 2D HOIPs suggest an enhancement of the octahedral distortion leads

to broadening of the STE peak.[16, 18-20,21] While the factors contributing to the initial decrease in Δd remain to be fully understood, the penetration depth of the DPDA spacer cations into the PbI_6 octahedral spaces is a possible factor. The penetration depth was determined as the distance between the N atoms and the plane of the axial iodide atoms[21], and the computational results indicate a decrease in the penetration depth upon compression (Figure 3.22). These results suggest a pressure-induced relaxation of the organic-inorganic interactions between the DPDA spacers and the lead-iodide octahedra, thus possibly influencing the octahedral distortion at low-pressure. Furthermore, upon further compression, a prominent increase in Δd is observed between 1-2 GPa, indicating a significant enhancement in octahedral distortion, in good agreement with both the broadening of the STE PL peak (Figure 3.15) and the isostructural phase transition at 1.5 GPa. Upon even further compression, a general decreasing trend in Δd beyond 2 GPa indicates a return to a less distorted octahedra, in good agreement with the narrowing of the STE and subsequent full dominance of the FE PL peak beyond 3.29 GPa (Figure 3.15). Furthermore, σ also exhibits an initial decrease at low-pressure, however the magnitude of the decrease likely indicates that Δd is the most significant factor behind the overall pressure-induced octahedral distortion.

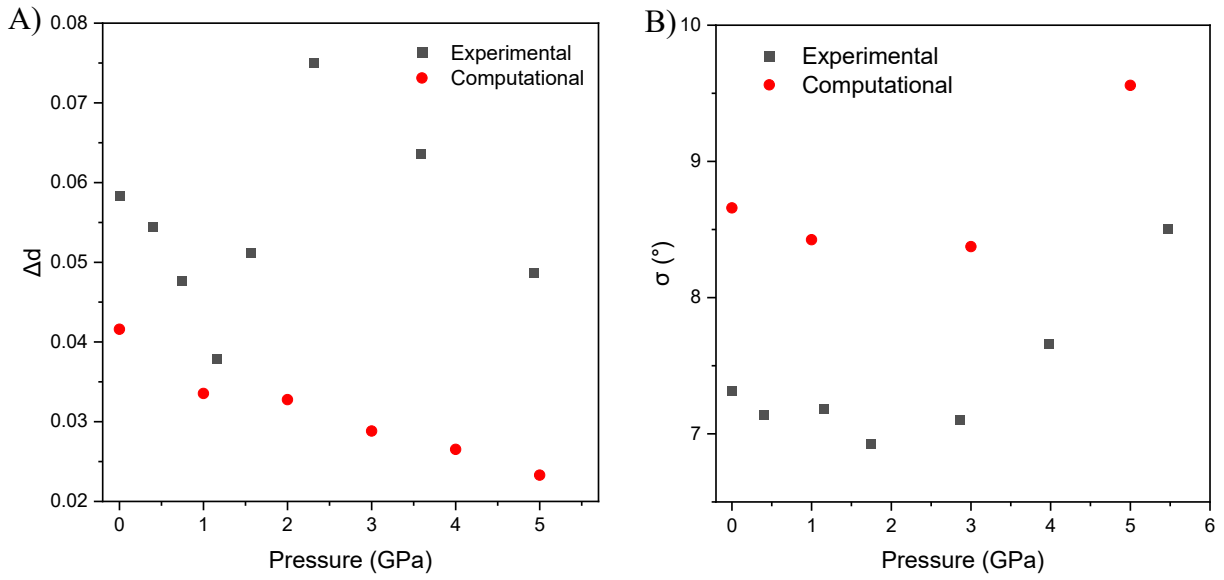

Figure 3.21. Computational distortion analysis of *DPDAPbI₄*. (A) bond length distortion and (B) bond angle variance as functions of pressure.

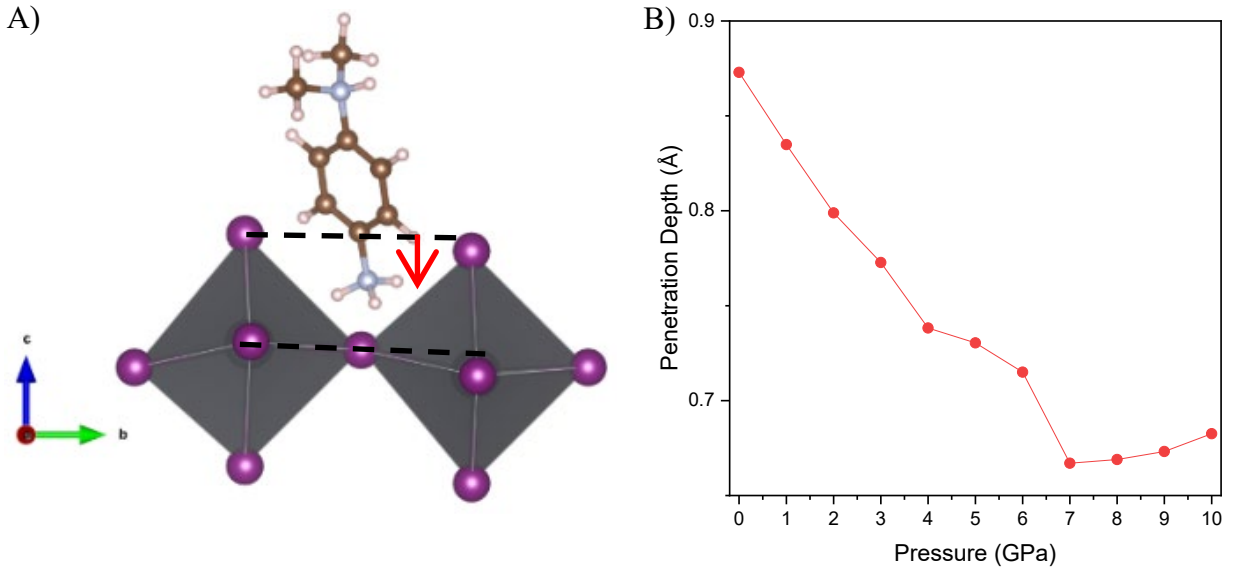

Figure 3.22. Penetration depth of *DPDAPbI₄*. (A) Schematic of penetration depth and (B) computational penetration depth as a function of pressure.

Furthermore, understanding the structure-property relationships can help determine the structural origins behind the observed structural modifications, in particular the phase transition at 1.5 GPa. A shortening of all the Pb-I bond lengths was observed upon performing the diffraction analysis. The equatorial bonds on average were found to contract from 3.22 to 3.14 Å upon compression to

1.56 GPa, in good agreement with the observed increase in Δ*d* between 1-2 GPa. The axial bonds, intriguingly, exhibited a slight increase from 3.27 to 3.33 Å upon compression to 1.56 GPa. These results also correlate strongly with the confirmed isostructural phase transition at 1.5 GPa, thus the pressure-induced enhancement of the octahedral distortion constitutes a crucial factor behind the phase transition. Furthermore, computational work conducted on the N–H···I hydrogen bond lengths (Figure 3.23) indicates, on average, a shortening of these bonds from 2.96 to 2.85 Å upon compression to 2 GPa, confirming the enhancement in the hydrogen bonding interactions previously proposed by the vibrational spectroscopy measurements and once again in good agreement with the observed phase transition. Thus, it can be concluded that the pressure-induced enhancement of both the octahedral distortion and hydrogen bonding interactions constitute the structural origins behind the observed phase transition at 1.5 GPa.

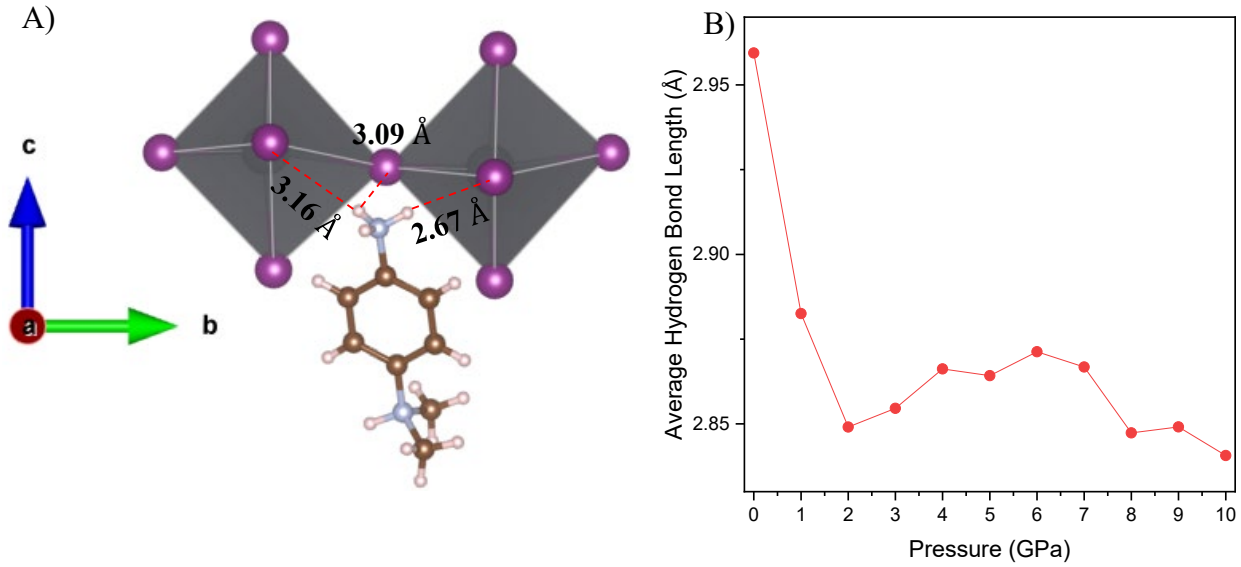

Figure 3.23. Hydrogen bonding in *DPDAPbI₄*. (A) N–H···I hydrogen formation at ambient pressure and (B) average computational N–H···I hydrogen bond length as a function of pressure.

Understanding the mechanisms behind the pressure-induced optoelectronic properties is a crucial factor for the design of new 2D HOIPs for various optoelectronic applications, in particular solar cells. Previous studies conducted on other 2D HOIPs indicate a strong correlation between the

enhancement in the hydrogen bonding interactions and the subsequent bandgap reduction.[17,22] In *(PMA)$_2$PbI$_4$* a pressure-induced enhancement in the hydrogen bonding interactions was found to lead to a significant bandgap reduction from 2.15 eV to 1.26 eV whilst also inducing PbI_6 octahedral distortion.[17] Another recently studied DJ 2D HOIP, *(3AMP)PbI$_4$* also showed a substantial bandgap reduction from 2.10 eV to 1.63 eV resulting from the Pb-I bond length shortening.[23] As discussed above, enhancement of the N–H···I hydrogen bonding interactions between the DPDA spacer cations and the inorganic octahedra is confirmed by the observed shortening of the calculated N–H···I hydrogen bond lengths from 2.96 to 2.84 Å upon compression to 10 GPa (Figure 3.23). Furthermore, the computations also indicate a shortening of the average Pb-I bond lengths from 3.27 to 3.02 Å for the equatorial bonds and from 3.30 to 3.05 Å for the axial bonds, in good agreement with the experimental results. A reduction of the computed Pb-I-Pb bond angle from 165 to 150° is also observed upon compression. These results are consistent with the previous studies conducted on *(PMA)$_2$PbI$_4$* and other 2D HOIPs, and the enhancement in the N–H···I hydrogen bonding interactions induces shortening of the Pb-I bond lengths and in turn leads to the overall bandgap reduction of *DPDAPbI$_4$* upon compression. Additionally, the enhancement of the N–H···I hydrogen bonding interactions upon compression to 2 GPa (Figure 3.23) is also in excellent agreement with the observed pressure-induced enhancement in the octahedral distortion, thus it is possible that the octahedral distortions might also play a crucial role in the bandgap reduction. These observations provide a solid understanding of the interplay between a highly rigid organic spacer and the inorganic octahedra leading to the pressure-induced optoelectronic properties at high-pressure.

3.4 Conclusions

We report the first ever high-pressure study on *DPDAPbI$_4$*, a DJ type 2D HOIP with a highly rigid and asymmetrically inserted DPDA organic spacer. A phase transition at 1.5 GPa was identified through the vibrational spectroscopy measurements and later confirmed by the XRD and PL measurements along with the subsequent distortion analysis. XRD analysis also confirmed anisotropic compression along the *c* direction. The PL measurements indicate a 3-4-fold increase in the intensity of the prominent FE peak upon compression to 1.49 GPa followed by a gradual decrease and eventual quenching upon further compression. The UV-Vis absorption measurements indicate a direct bandgap throughout compression and a bandgap reduction from 2.26 eV to 1.87 eV upon compression to 8.84 GPa. The distortion analysis indicates a significant enhancement in the bond length distortion between 1-2 GPa, consistent with the enhanced PL intensity of the FE peak and the subsequent broadening of the STE peak upon compression to 1.23 GPa. An enhancement in the hydrogen bonding interactions is proposed through the vibrational spectroscopy measurements and is later confirmed by the computational work, with the enhancement leading to the shortening of the Pb-I bond lengths upon compression, thus constituting the mechanism behind the overall bandgap reduction. Furthermore, the pressure-induced enhancement in the hydrogen bonding interactions in tandem with the enhanced octahedral distortion constitute the major structural origins behind the observed phase transition. Overall, these results help deepen the understanding of the impact of HP on the structural modifications and the optoelectronic properties of *DPDAPbI$_4$*, thus providing a basis for the design of future 2D HOIPs for practical applications like solar cells.

3.5 References

(1) Mao, L.; Stoumpos, C. C.; Kanatzidis, M. G. Two-Dimensional Hybrid Halide Perovskites: Principles and Promises. *Journal of the American Chemical Society* **2019**, *141* (3), 1171-1190.

(2) Mao, L.; Ke, W.; Pedesseau, L.; Wu, Y.; Katan, C.; Even, J.; Wasielewski, M. R.; Stoumpos, C. C.; Kanatzidis, M. G. Hybrid Dion–Jacobson 2D Lead Iodide Perovskites. *Journal of the American Chemical Society* **2018**, *140* (10), 3775-3783.

(3) Li, X.; Hoffman, J. M.; Kanatzidis, M. G. The 2D Halide Perovskite Rulebook: How the Spacer Influences Everything from the Structure to Optoelectronic Device Efficiency. *Chemical Reviews* **2021**, *121* (4), 2230-2291.

(4) Billing, D. G. and Lemmerer, A. Inorganic–organic hybrid materials incorporating primary cyclic ammonium cations: The lead iodide series. *CrystEngComm* **2007**, *9* (3), 236-244.

(5) Ortiz-Cervantes, C.; Carmona-Monroy, P.; Solis-Ibarra, D. Two-Dimensional Halide Perovskites in Solar Cells: 2D or not 2D? *ChemSusChem* **2019**, *12* (8), 1560-1575.

(6) Hautzinger, M. P.; Dai, J.; Ji, Y.; Fu, Y.; Chen, J.; Guzei, I. A.; Wright, J. C.; Li, Y.; Jin, S. Two-Dimensional Lead Halide Perovskites Templated by a Conjugated Asymmetric Diammonium. *Inorganic Chemistry* **2017**, *56* (24), 14991-14998.

(7) Dohner, E. R.; Hoke, E. T.; Karunadasa, H. I. Self-Assembly of Broadband White-Light Emitters. *Journal of the American Chemical Society* **2014**, *136* (5), 1718-1721.

(8) Mao, L.; Wu, Y.; Stoumpos, C. C.; Wasielewski, M. R.; Kanatzidis, M. G. White-Light Emission and Structural Distortion in New Corrugated Two-Dimensional Lead Bromide Perovskites. *Journal of the American Chemical Society* **2017**, *139* (14), 5210-5215.

(9) Li, Y. Y.; Lin, C. K.; Zheng, G. L.; Cheng, Z. Y.; You, H.; Wang, W. D.; Lin, J. Novel〈110〉-Oriented Organic−Inorganic Perovskite Compound Stabilized by N-(3-Aminopropyl)imidazole with Improved Optical Properties. *Chemistry of Materials* **2006**, *18* (15), 3463-3469.

(10) Dobrzycki, L. and Woźniak, K. Inorganic–organic hybrid salts of diaminobenzenes and related cations. *CrystEngComm* **2008**, *10* (5), 577-589.

(11) Rayner, M. K. and Billing, D. G. Poly[1,4-bis-(ammonio-meth-yl)cyclo-hexane [di-μ-bromido-dibromido-plumbate(II)]]. *Acta Crystallogr Sect E Struct Rep Online* **2010**, *66* (Pt 6), m658.

(12) Cortecchia, D.; Neutzner, S.; Srimath Kandada, A. R.; Mosconi, E.; Meggiolaro, D.; De Angelis, F.; Soci, C.; Petrozza, A. Broadband Emission in Two-Dimensional Hybrid Perovskites: The Role of Structural Deformation. *Journal of the American Chemical Society* **2017**, *139* (1), 39-42.

(13) Du, K.-z.; Tu, Q.; Zhang, X.; Han, Q.; Liu, J.; Zauscher, S.; Mitzi, D. B. Two-Dimensional Lead(II) Halide-Based Hybrid Perovskites Templated by Acene Alkylamines: Crystal Structures, Optical Properties, and Piezoelectricity. *Inorganic Chemistry* **2017**, *56* (15), 9291-9302.

(14) Peng, W.; Yin, J.; Ho, K.-T.; Ouellette, O.; De Bastiani, M.; Murali, B.; El Tall, O.; Shen, C.; Miao, X.; Pan, J.; Alarousu, E.; He, J-H.; Ooi, B. S.; Mohammed, O. F.; Sargent, E.; Bakr, O, M. Ultralow Self-Doping in Two-dimensional Hybrid Perovskite Single Crystals. *Nano Letters* **2017**, *17* (8), 4759-4767.

(15) Amat, A.; Mosconi, E.; Ronca, E.; Quarti, C.; Umari, P.; Nazeeruddin, M. K.; Grätzel, M.; De Angelis, F. Cation-Induced Band-Gap Tuning in Organohalide Perovskites: Interplay of Spin–Orbit Coupling and Octahedra Tilting. *Nano Letters* **2014**, *14* (6), 3608-3616.

(16) Smith, M. D.; Jaffe, A.; Dohner, E. R.; Lindenberg, A. M.; Karunadasa, H. I. Structural origins of broadband emission from layered Pb–Br hybrid perovskites. *Chemical Science* **2017**, *8* (6), 4497-4504.

(17) Tian, C.; Liang, Y.; Chen, W.; Huang, Y.; Huang, X.; Tian, F.; Yang, X. Hydrogen-bond enhancement triggered structural evolution and band gap engineering of hybrid perovskite (C6H5CH2NH3)2PbI4 under high pressure. *Physical Chemistry Chemical Physics* **2020**, *22* (4), 1841-1846.

(18) Chen, C.; Zhao, X.; Gong, Y.; Liu, Y.; Chen, Z.; Zhang, L.; Chen, J.; Deng, Z.; Lu, H.; Luo, M.; Canepa, P.; Mao, L. Two-Dimensional Hybrid Dion–Jacobson Germanium Halide Perovskites. *Chemistry of Materials* **2023**, *35* (8), 3265-3275.

(19) Spanopoulos, I.; Hadar, I.; Ke, W.; Guo, P.; Mozur, E. M.; Morgan, E.; Wang, S.; Zheng, D.; Padgaonkar, S.; Manjunatha Reddy, G. N.; Weiss, E. A.; Hersam, M. C.; Seshadri, R.; Schaller, R. D.; Kanatzidis, M. G. Tunable Broad Light Emission from 3D "Hollow" Bromide Perovskites through Defect Engineering. *Journal of the American Chemical Society* **2021**, *143* (18), 7069-7080.

(20) Mączka, M.; Sobczak, S.; Ratajczyk, P.; Leite, F. F.; Paraguassu, W.; Dybała, F.; Herman, A. P.; Kudrawiec, R.; Katrusiak, A. Pressure-Driven Phase Transition in Two-Dimensional Perovskite MHy2PbBr4. *Chemistry of Materials* **2022**, *34* (17), 7867-7877.

(21) Gao, F.-F.; Song, H.; Li, Z.-G.; Qin, Y.; Li, X.; Yao, Z.-Q.; Fan, J.-H.; Wu, X.; Li, W.; Bu, X.-H. Pressure-Tuned Multicolor Emission of 2D Lead Halide Perovskites with Ultrahigh Color Purity. *Angewandte Chemie International Edition* **2023**, *62* (12), e202218675.

(22) Liu, G.; Gong, J.; Kong, L.; Schaller, R. D.; Hu, Q.; Liu, Z.; Yan, S.; Yang, W.; Stoumpos, C. C.; Kanatzidis, M. G.; Mao, H.; Xu, T. Isothermal pressure-derived metastable states in 2D hybrid perovskites showing enduring bandgap narrowing. *Proceedings of the National Academy of Sciences* **2018**, *115* (32), 8076-8081.

(23) Kong, L.; Liu, G.; Gong, J.; Mao, L.; Chen, M.; Hu, Q.; Lü, X.; Yang, W.; Kanatzidis, M. G.; Mao, H.-k. Highly tunable properties in pressure-treated two-dimensional Dion–Jacobson perovskites. *Proceedings of the National Academy of Sciences* **2020**, *117* (28), 16121-16126.

4. Effects of High Pressure on the Structures and Optoelectronic Properties of $CMA_2MAPb_2I_7$ and $CMA_2FAPb_2I_7$

4.1 Introduction

Among the various applications of both 3D and 2D hybrid organic-inorganic perovskites (HOIPs), their use in solar cell fabrication has been extensively studied in recent years.[1,2] In particular, the efficiency of perovskite solar cells have significantly improved over the years, reaching a record 25.6% in 2020, very close to the 26.7% achieved for Si-based solar cells.[3] Furthermore, in 2020 Al-Ashouri et al. reported a perovskite-silicon tandem solar cell through self-assembly with a certified efficiency of 29.15%.[3,4,5] However, 3D perovskites exhibit significant disadvantages including poor stability against humidity and light, restricted chemical composition, and the use of toxic and volatile cations.[1,6,7,8,9] As a result, a transition to the use of 2D hybrid organic-inorganic perovskites (HOIPs) in solar cell applications has been made, in particular CMA-based 2D HOIPs (CMA = cyclohexane methylamine) largely due to their enhanced stability under humid conditions and favorable optoelectronic properties.[10,11] Additionally, as the optoelectronic properties, in particular the bandgap, can be easily modified using high pressure, the ability to achieve the desired Shockley-Queisser limit of 1.34 eV for the bandgap is greatly increased, thus further making 2D HOIPs a highly promising candidate for solar cell fabrication.[12,13] In particular, high n-2D HOIPs have generated significant interest in solar cell applications over the years.

High n-2D HOIPs consist of a greater number of metal-halide octahedra, typically for n = 2-5.[14] High n-2D HOIPs also exhibit enhanced stability against moisture in comparison to their 3D counterparts, thus allowing for solar cell fabrication under humid conditions.[15,16] Another significant advantage of high n-2D HOIPs in comparison to 3D and low n-2D HOIPs is the suppression of trap states, which can lead to defects thus compromising the performance of the solar cell.[17,18] Amongst the numerous previously studied 2D HOIPs, CMA-based 2D HOIPs have garnered significant interest for solar cell applications due to their favorable properties.[10,11] In particular, $(CMA)_2(MA)_{n-1}Pb_nI_{3n+1}$ high n-2D HOIPs where CMA is cyclohexane methylamine and MA is methylamine exhibit lower bandgap values at ambient pressure, thus providing greater potential for achieving the Shockley-Quiesser limit.[10,11] Wei et al. showed such perovskites exhibit enhanced efficiency, with the best efficiency of 15.05% achieved when n = 9.[11] $(CMA)_2(MA)_{n-1}Pb_nI_{3n+1}$ high n-2D HOIP solar cells have also been shown to exhibit improved stability under humid conditions, with the n = 4 perovskite solar cell maintaining 95% of its initial efficiency upon exposure to ambient air with 60% relative humidity for 1500 hours in comparison to only 30% for the $MAPbI_3$ 3D counterpart.[10] Moreover, Wei et al. showed that the n = 9 perovskite solar cell also retained 95% of its initial efficiency upon exposure to ambient air with 40-70% relative humidity for 4600 hours.[11] In comparison, the efficiency of the $MAPbI_3$ 3D counterpart solar cell rapidly declined after 500 hours followed by becoming completely damaged after 2160 hours.[11]

In addition to the enhanced stability under humid conditions, $(CMA)_2(MA)_{n-1}Pb_nI_{3n+1}$ perovskites also exhibit excellent optoelectronic properties. In particular, Wei et al. reported that the n = 1 perovskite (CMA_2PbI_4) exhibited PL emission at 536 nm with intensity much greater

compared to most lead-based n = 1 perovskites.[10] Furthermore, Jia et al. reported a surprisingly high photoluminescence quantum yield of 16.3% for CMA_2PbI_4, which is rarely observed in previously studied 2D lead-halide perovskites.[19] CMA is also a highly soft organic spacer, thus making high-pressure (HP) studies highly intriguing, especially given the greater expected compressibility. Thus, this along with the improved stability and promising optoelectronic properties under ambient conditions make $(CMA)_2(MA)_{n-1}Pb_nI_{3n+1}$ perovskites ideal candidates for high-pressure (HP) studies as the modifications to achieve the desired properties for implementation in solar cell applications are greatly reduced. Additionally, understanding of the behavior of high n CMA-based 2D lead-iodide perovskites can provide valuable insights into the impact of greater lead-halide octahedra in achieving the desired properties for solar cell applications.

Among the several organic cations used for perovskites, in particular 3D perovskites, methylammonium (MA) and formamidinium (FA) are two of the most common.[1] Unfortunately, MA-based perovskites tend to exhibit greater bandgaps values along with poor thermal stability.[13] For example, Wei et al. reported bandgap values at ambient pressure of $(CMA)_2(MA)_{n-1}Pb_nI_{3n+1}$ perovskites of 2.36, 2.13, 1.96, and 1.86 for n = 1, 2, 3, and 4.[10] In comparison, $FAPbI_3$-based PSCs have exhibited improved thermal stability and resistance to evaporation along with a more ideal bandgap of 1.48 eV, thus providing a better ability to achieve the desired Shockley-Quiesser limit and ideal bandgap of 1.34 eV.[20,21] Moreover, $FAPbI_3$-based PSCs achieved a certified efficiency as high as 25.2%, thus making FA-based perovskites promising candidates for PSCs.[22] Thus, given the lower bandgap values of FA-based perovskites, it would be of great interest to examine the behavior of $CMA_2FAPb_2I_7$ under high-pressure. As a result, performing high-pressure

studies can provide a solid comparison between the use of MA and FA organic cations, in particular for assessing the ability to achieve the Shockley-Quiesser limit at high-pressure, thus also providing a potential basis for the use in solar cell applications.

$CMA_2MAPb_2I_7$ and $CMA_2FAPb_2I_7$ have been previously synthesized by our collaborators from the Song Jin group at the University of Wisconsin-Madison. As seen in Figure 4.1, $CMA_2MAPb_2I_7$ and $CMA_2FAPb_2I_7$ both have an orthorhombic crystal structure with Pbcn and Pnma space groups, respectively (Table 4.1). The CMA organic spacer consists of a cyclohexane ring with a single NH_3^+ group attached. According to the previous study by Wei et al. $CMA_2MAPb_2I_7$ exhibits strong photoluminescence at 595 nm and an optical bandgap of 2.13 eV at ambient pressure.

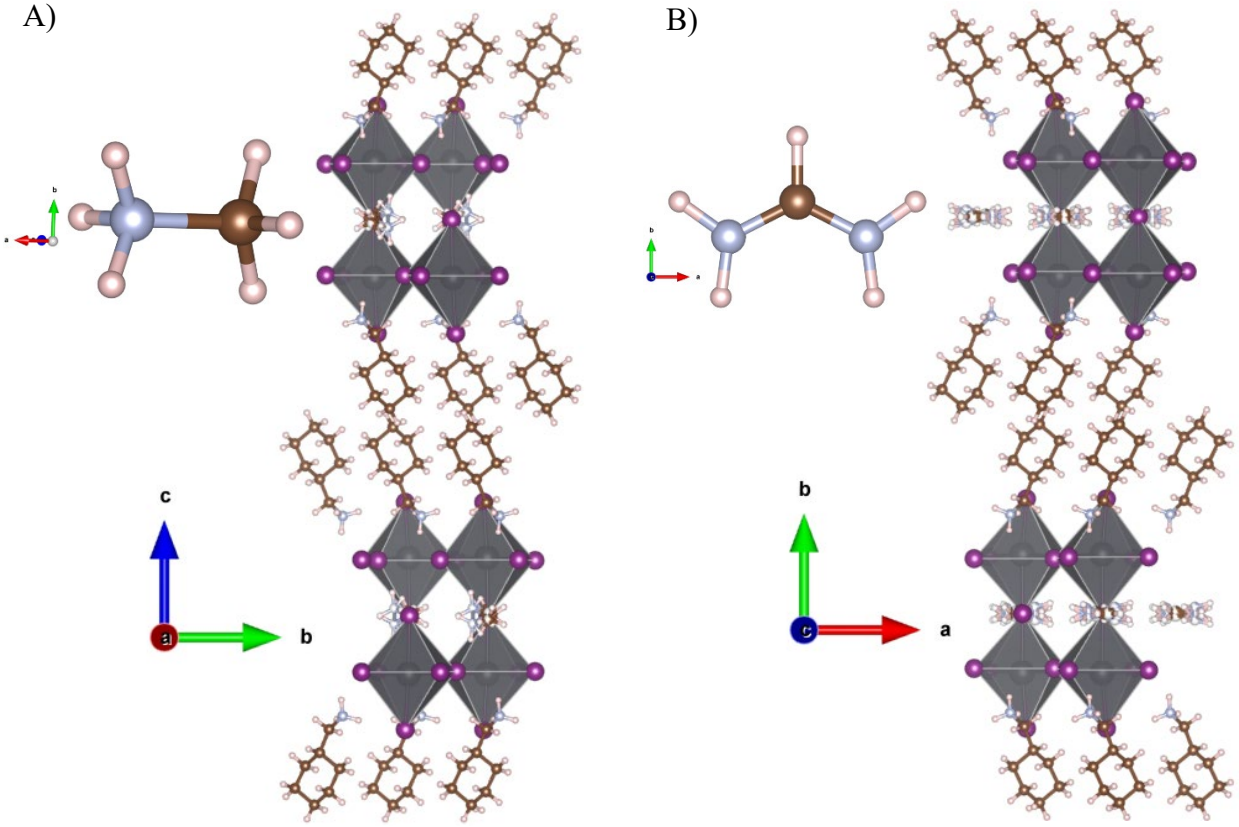

Figure 4.1. Crystal structures of (A) $CMA_2MAPb_2I_7$ and (B) $CMA_2FAPb_2I_7$ at ambient pressure with the structures of the MA and FA A-site cations.

Table 4.1. Crystallographic parameters of $CMA_2MAPb_2I_7$ and $CMA_2FAPb_2I_7$ under ambient conditions from our collaborators.

Parameter	$CMA_2MAPb_2I_7$	$CMA_2FAPb_2I_7$
Crystal Structure	Orthorhombic	Orthorhombic
Space Group	Pbcn	Pnma
a (Å)	8.770(19)	8.869(3)
b (Å)	8.760(19)	44.050(13)
c (Å)	44.400(9)	8.801(3)
V ($Å^3$)	3410.0(22)	3438.2(19)
Z	4	4

In this chapter the effects of HP on the structures and optoelectronic properties of $CMA_2MAPb_2I_7$ and $CMA_2FAPb_2I_7$ were investigated and compared. Vibrational spectroscopy was used to identify potential phase transitions and changes in the hydrogen bonding between the NH_3 groups of the CMA spacer and the iodine of the lead-iodide octahedra at HP. X-Ray diffraction (XRD) measurements were performed at HP and along with the LeBail refinements of the 1D powder patterns were used to examine the compressibility and provide further evidence of the phase transitions. The optoelectronic properties at HP were studied through Photoluminescence (PL) and UV-Vis Absorption (UV-Vis) measurements. PL was used to examine excitonic behavior at HP while UV-Vis measurements were used to study the changes to the bandgap.

4.2 Synthesis and Experimental Details

The $CMA_2MAPb_2I_7$ and $CMA_2FAPb_2I_7$ crystals used in this study were synthesized by Matthew Hautzinger from Prof. Song Jin's group at the University of Wisconsin-Madison. FTIR measurements followed the method detailed in section 2.3.2. Powder samples were loaded for the FTIR measurements. KBr was loaded for the FTIR measurements to reduce laser damage while no pressure transmitting medium (PTM) was required. XRD measurements followed the methods

detailed in section 2.3.3. Packed powder samples and silicone oil as the PTM were used for the XRD measurements. Photoluminescence and UV-Vis absorption measurements followed the methods detailed in section 2.3.4 and 2.3.5. Measurements were performed using single crystals with silicone oil as the PTM.

4.3 Results and Discussion

4.3.1 Vibrational Spectroscopy

The vibrational modes in both $CMA_2MAPb_2I_7$ and $CMA_2FAPb_2I_7$ were examined through high-pressure (HP) FTIR spectroscopy to help identify and characterize the structural changes and potential phase transitions upon compression. Of the various vibrational modes observed, focus is on those that provide the best understanding of the pressure-induced structural modifications, in particular those for the CMA spacer and MA and FA organic cations. The FTIR spectra at ambient pressure for both compounds are shown in Figure 4.2.

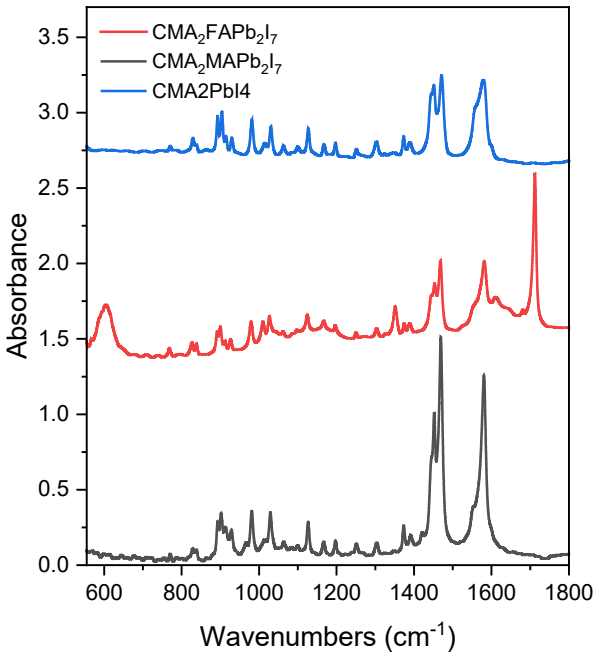

Figure 4.2. FTIR spectra of $CMA_2MAPb_2I_7$ and $CMA_2FAPb_2I_7$ in comparison with CMA_2PbI_4 at ambient pressure.

The vibrational modes were assigned through calculations of CMA in vapor form in vacuum and comparing it with the 0 GPa spectra. The assignment of the characteristic peaks is shown in Table 4.2 along with the schematics of each mode shown in Figure 4.3.

Table 4.2. Characteristic peak assignment for CMA spacer and MA^+ cation.

Calculated (cm^{-1})	***$CMA_2MAPb_2I_7$* (cm^{-1})**	***$CMA_2FAPb_2I_7$* (cm^{-1})**	**Assignment**
980	981	979	*C–N* stretching (MA^+)
1020	1029	1027	*NH_3* rocking
1500	1452	1453	*NH_3* bending
1502	1469	1468	*NH_3* bending
1669	1581	1581	*NH_3* scissoring

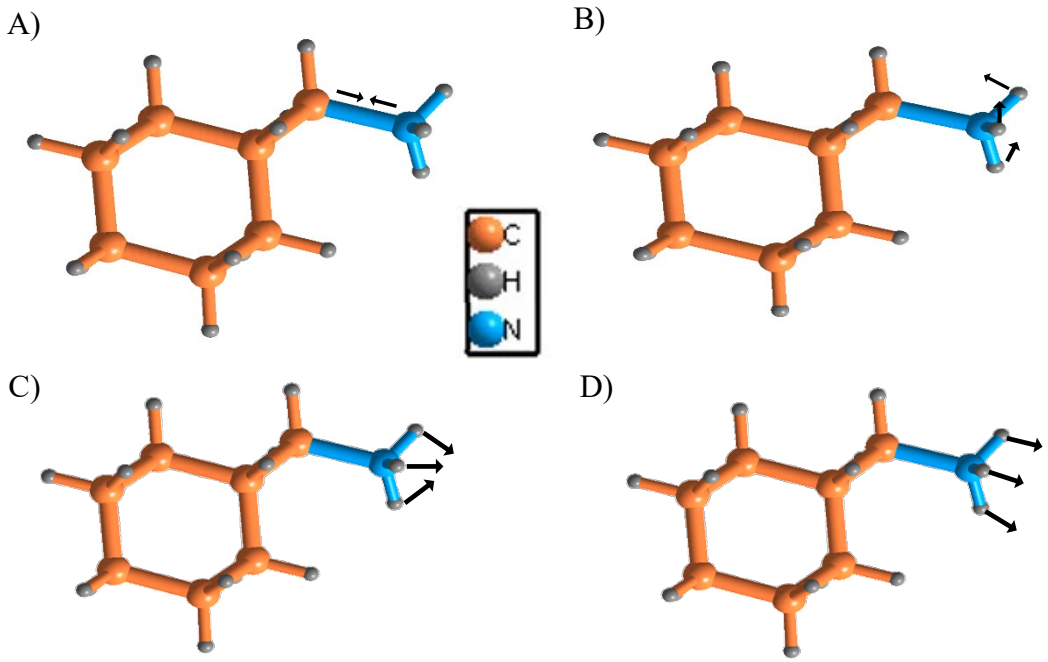

Figure 4.3. Schematics of characteristic vibrational modes in CMA. (A) *C–N* stretching mode, (B) *NH_3* rocking mode, (C) *NH_3* bending mode, (D) *NH_3* scissoring mode.

The *C–N* stretching mode for both *$CMA_2MAPb_2I_7$* (981 cm^{-1}) and *$CMA_2FAPb_2I_7$* (979 cm^{-1}) exhibits a blueshift upon compression (Figure 4.4). Both compounds experiencing a significant shift between 3-5 GPa with *$CMA_2FAPb_2I_7$* experiencing a much greater shift compared to

CMA₂MAPb₂I₇. The *NH₃* rocking mode for both *CMA₂MAPb₂I₇* (1029 cm^{-1}) and *CMA₂FAPb₂I₇* (1027 cm^{-1}) also exhibits a blueshift upon compression (Figure 4.5). Both compounds once again experience a significant shift between 3-5 GPa, with *CMA₂FAPb₂I₇* once again experiencing the greater shift . These results indicate a possible phase transition between 3-5 GPa, possibly a result of the high softness of the CMA spacers.

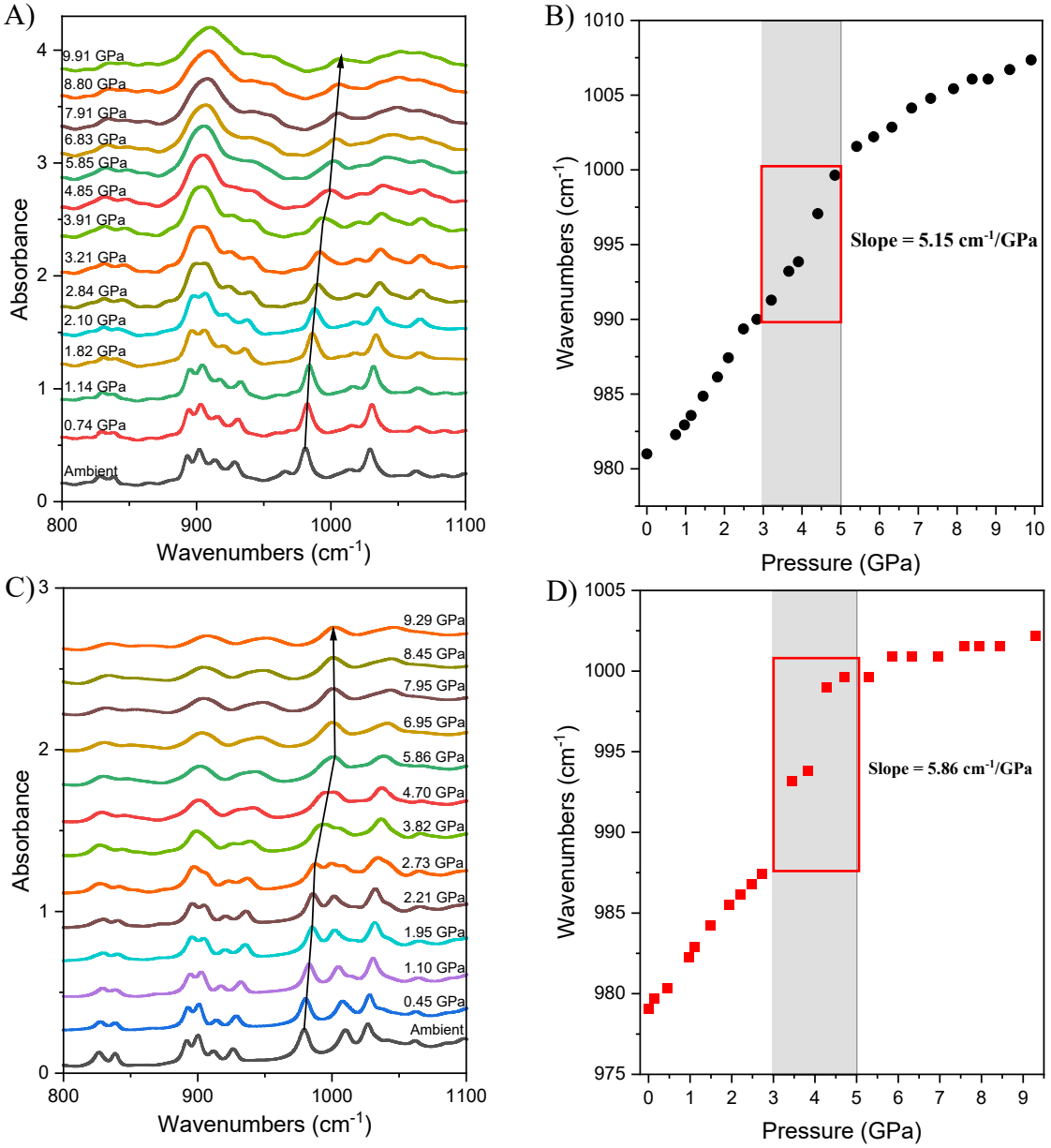

Figure 4.4. FTIR spectra of *C–N* stretching mode. (A) spectra of *CMA₂MAPb₂I₇* upon compression and (B) frequency as a function of pressure. (C) spectra of *CMA₂FAPb₂I₇* upon compression and (D) frequency as a function of pressure.

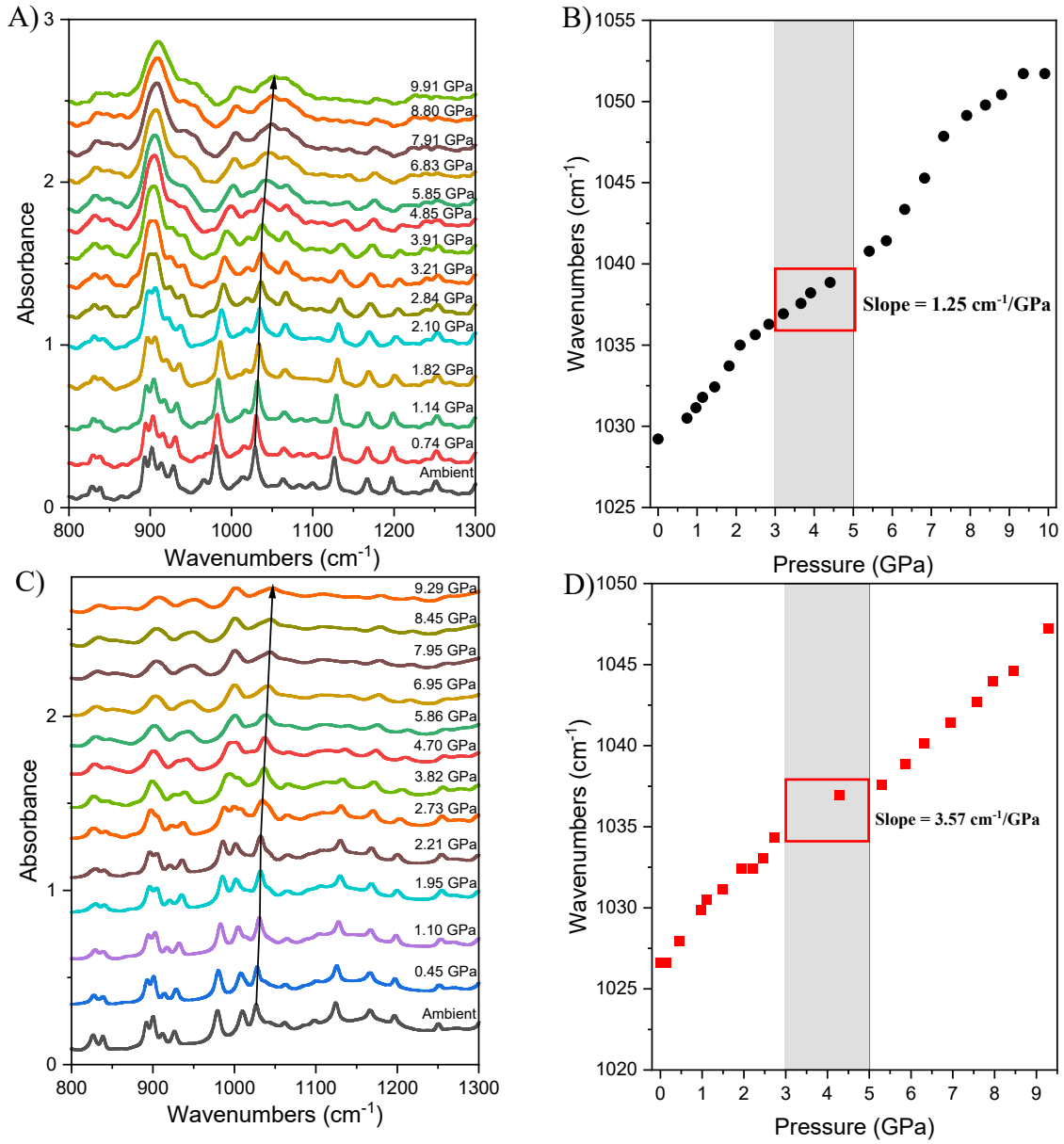

Figure 4.5. FTIR spectra of NH_3 rocking mode. (A) spectra of $CMA_2MAPb_2I_7$ upon compression and (B) frequency as a function of pressure. (C) spectra of $CMA_2FAPb_2I_7$ upon compression and (D) frequency as a function of pressure.

The NH_3 bending modes for both compounds exhibit a redshift shift upon compression (Figure 4.6), indicating H_N---I hydrogen bonding interactions likely between the NH_3 groups in the CMA spacers and the iodides in the lead-iodide octahedra. The presence of these bonds is further evidenced by the pressure-induced redshift of the NH_3 scissoring mode for both compounds

(Figure 4.7). Both modes, in general, experience a more significant shift between 3-5 GPa, thus providing further evidence of the phase transition between 3-5 GPa. These results also indicate a possible bandgap reduction, which in turn would suggest a shortening of the Pb-I bond lengths upon compression.

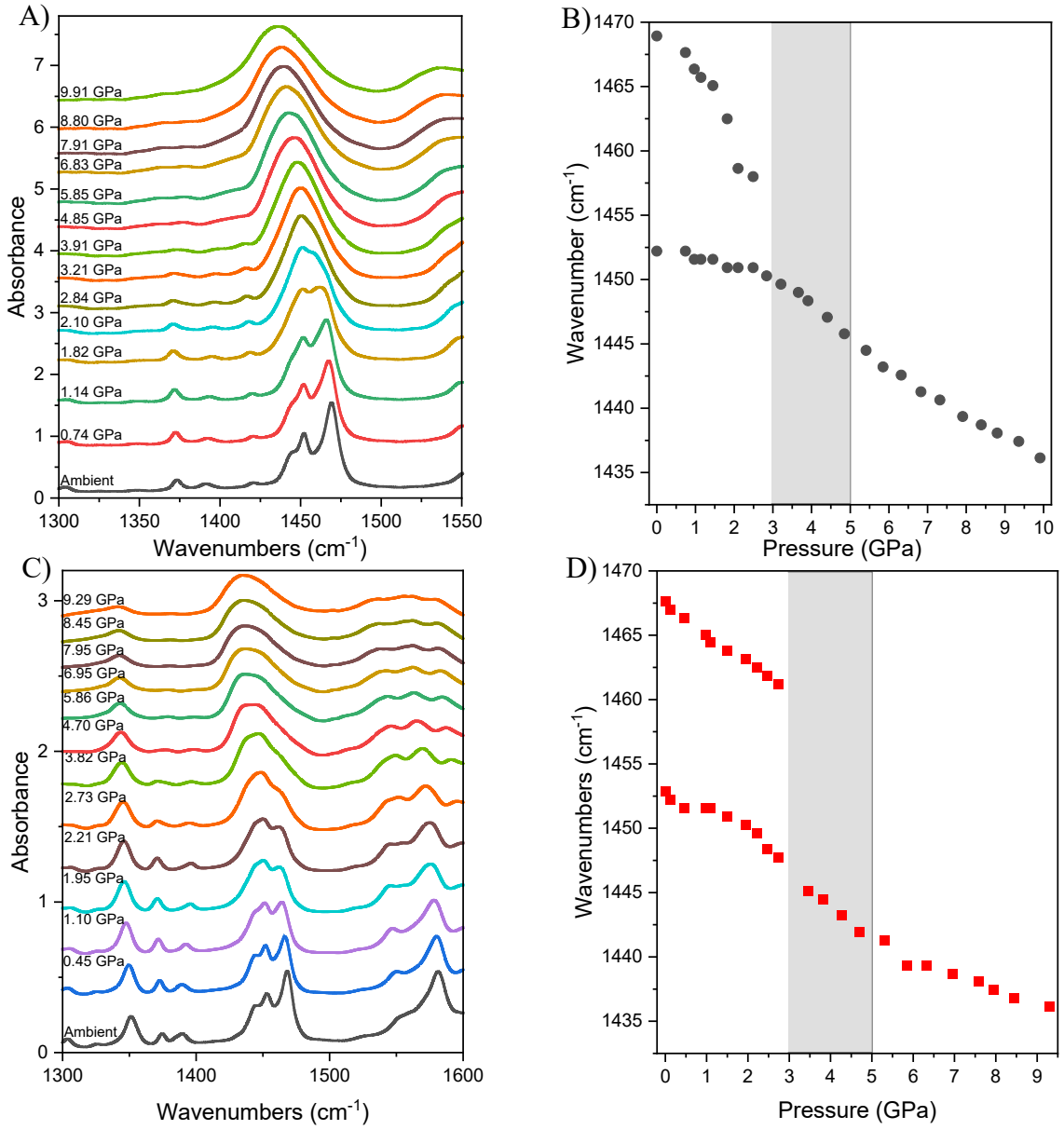

Figure 4.6. FTIR spectra of NH_3 bending modes. (A) spectra of $CMA_2MAPb_2I_7$ upon compression and (B) frequency as a function of pressure. (C) spectra of $CMA_2FAPb_2I_7$ upon compression and (D) frequency as a function of pressure.

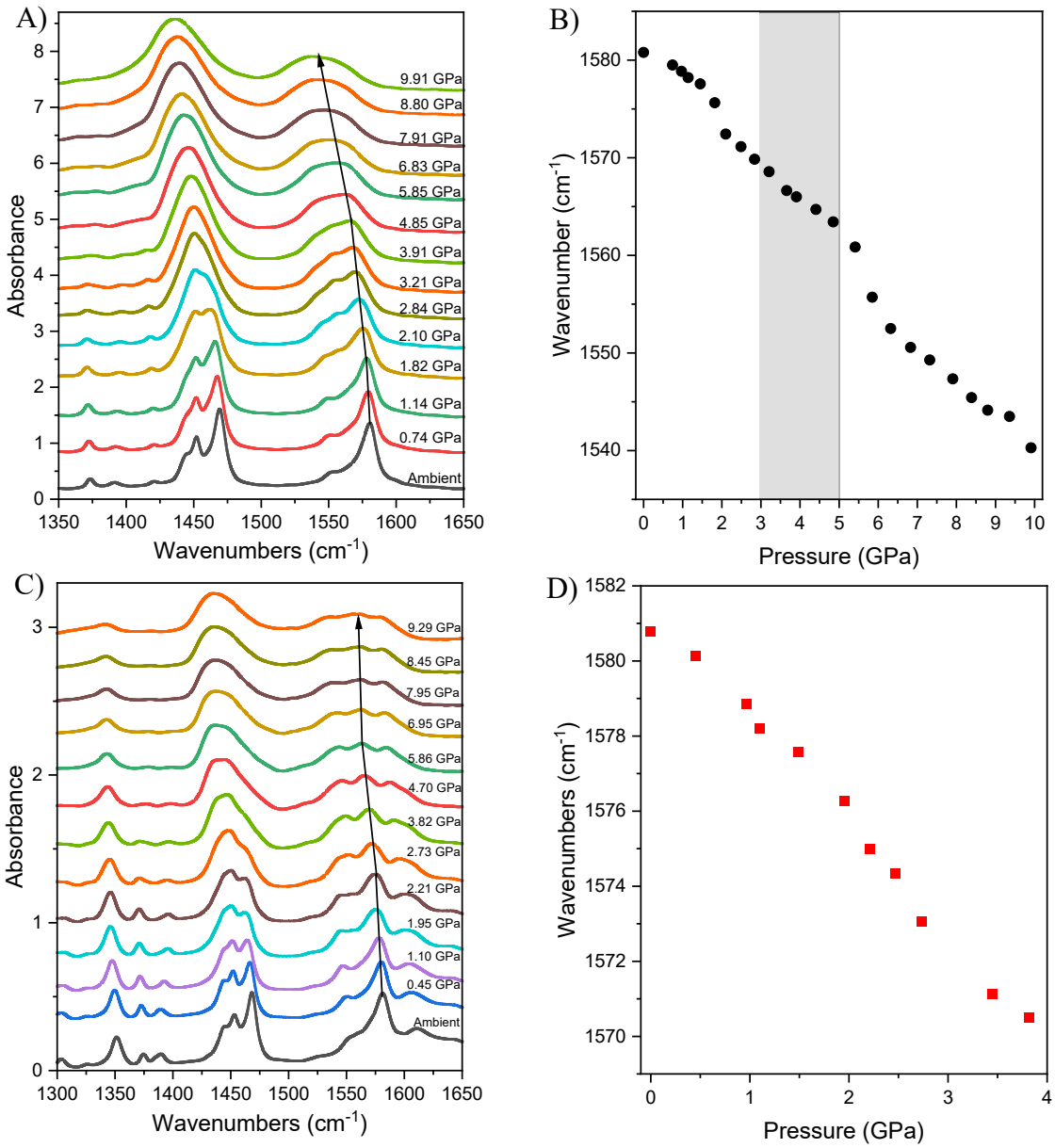

Figure 4.7. FTIR spectra of NH_3 scissoring mode. (A) spectra of $CMA_2MAPb_2I_7$ upon compression and (B) frequency as a function of pressure. (C) spectra of $CMA_2FAPb_2I_7$ upon compression and (D) frequency as a function of pressure.

Furthermore, the broadening of the characteristic peaks beyond around 4 GPa indicates the onset of amorphization. Additionally, upon decompression the recovered state was found to be identical to the pre-compression state for both compounds (Figure 4.8), indicating reversible structural modifications and no metastable changes upon pressure treatment.

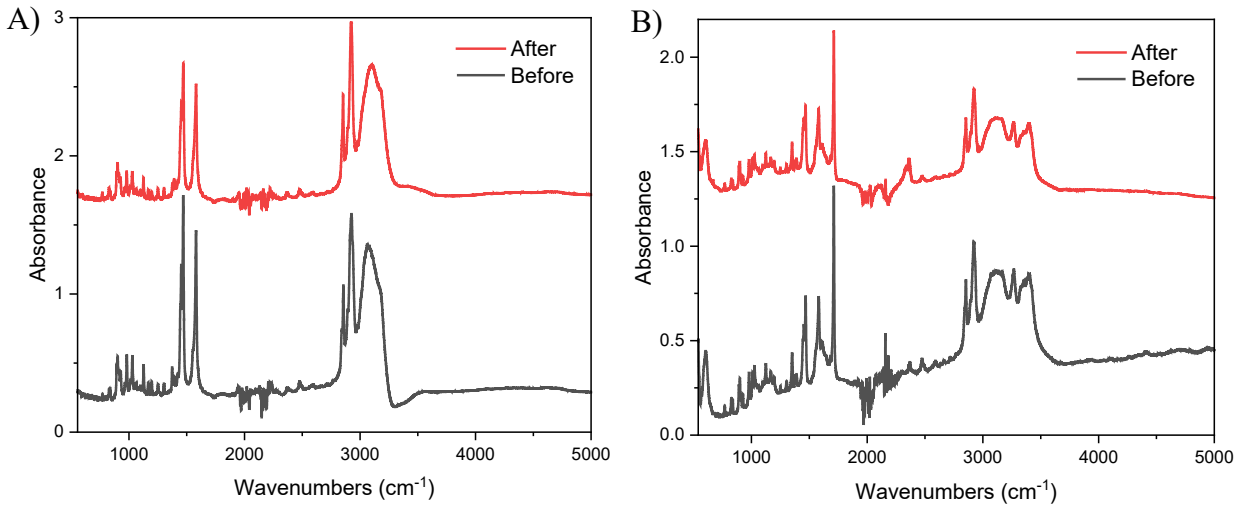

Figure 4.8. FTIR spectra of (A) $CMA_2MAPb_2I_7$ and (B) $CMA_2FAPb_2I_7$ before and after compression.

4.3.2 X-Ray Diffraction

To help provide further evidence of the pressure-induced structural modifications upon compression, in particular the proposed phase transition, *in situ* X-ray diffraction (XRD) measurements were performed. Based on the single crystal diffraction measurements conducted by our collaborators, both $CMA_2MAPb_2I_7$ and $CMA_2FAPb_2I_7$ were found to exhibit an orthorhombic crystal structure with Pbcn and Pnma space groups, respectively. The initial lattice parameters were obtained upon performing LeBail refinement of the diffraction patterns, as seen in Table 4.3.

Table 4.3. LeBail refined lattice parameters of $CMA_2MAPb_2I_7$ and $CMA_2FAPb_2I_7$ at ambient pressure.

Parameter	***$CMA_2MAPb_2I_7$***	***$CMA_2FAPb_2I_7$***
Space Group	Pbcn	Pnma
a (Å)	8.8319	8.8939(22)
b (Å)	8.703	44.224(8)
c (Å)	45.3086	8.7817(19)
V (Å^3)	3482.6415	3454.0519
Z	4	4

As evidenced by Figure 4.9, a disappearance of the peaks at around 11.5° and 12.8° above 3.20 GPa in $CMA_2MAPb_2I_7$, shown by the black arrows, is observed. Moreover, broadening of the peaks around 11.3° and 12.7° above 3.50 GPa in $CMA_2FAPb_2I_7$, shown by the red arrows, is also observed. These changes in the diffractions patterns provide further evidence of the phase transition between 3-5 GPa. Once again the lack of significant changes in the diffractograms at HP indicates the phase transition is isostructural.

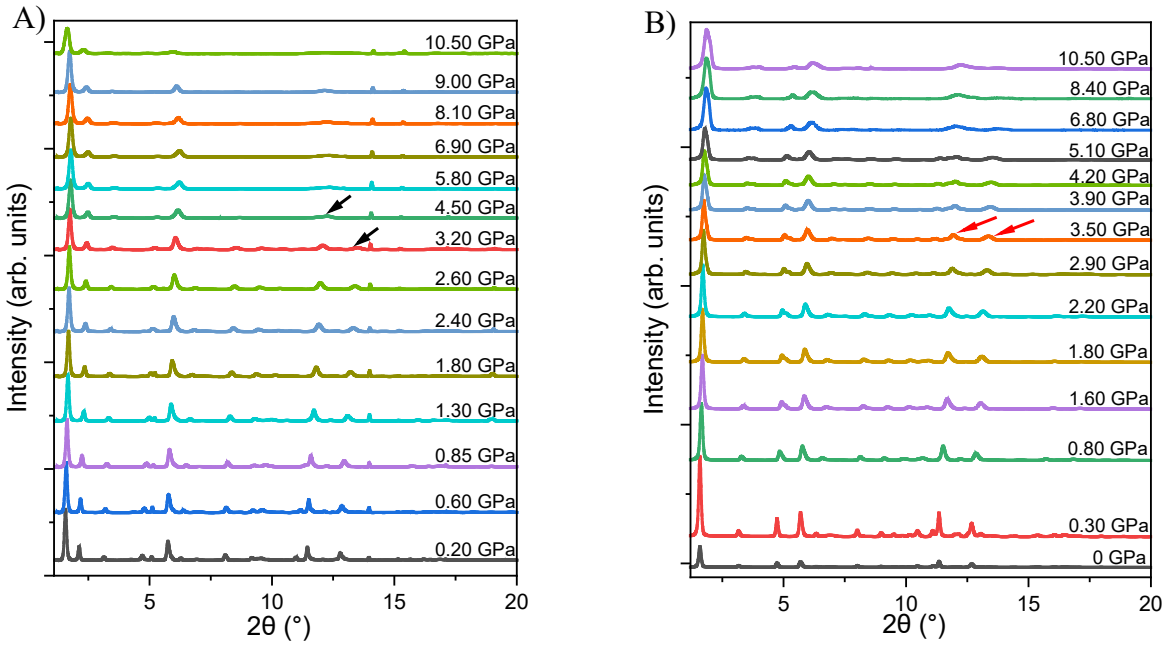

Figure 4.9. XRD diffractograms upon compression of CMA samples. (A) $CMA_2MAPb_2I_7$ with pressure-induced modifications shown by black arrows, and (B) $CMA_2FAPb_2I_7$ with pressure-induced modifications shown by red arrows.

Lebail refinements of the 1D XRD powder patterns were performed for both compounds to obtain the lattice parameters (Table 4.4 and Table 4.5), thus helping to gain a better of the structural modifications at HP. LeBail fitting below 3 GPa was found to be highly reliable (Figure 4.10), however upon further compression beyond 5 GPa the increase in uncertainty makes refinement much more challenging.

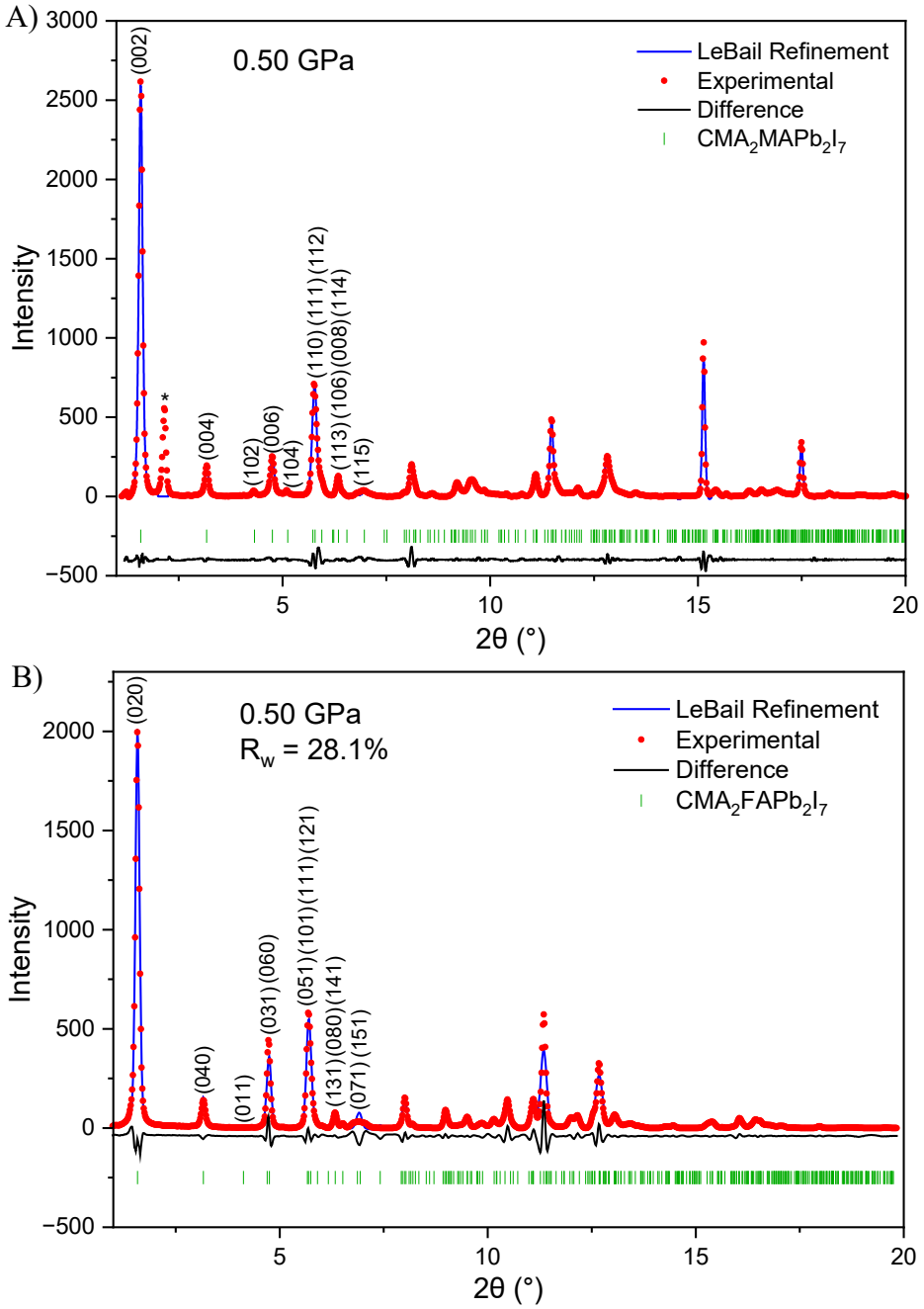

Figure 4.10. LeBail Refinements at 0.50 GPa for (A) *CMA₂MAPb₂I₇* and (B) *CMA₂FAPb₂I₇* with major reflections shown below 2θ = 7° and * representing impurities.

Upon performing the initial LeBail refinements, both $CMA_2MAPb_2I_7$ and $CMA_2FAPb_2I_7$ were found to maintain their respective space group symmetry throughout compression, thus providing evidence that the phase transition is indeed isostructural. As seen in Figure 4.11 and Table 4.4, for $CMA_2MAPb_2I_7$ the greatest compressibility occurs along the *c* axis, indicating anisotropic compression along the *c* direction. Interestingly, the *b* parameter was found to increase upon compression beyond 3 GPa, suggesting a possible negative linear compressibility of the *b* parameter at high-pressure. Such negative linear compressibility has been previously observed in CMA_2PbI_4.[23] In contrast, for $CMA_2FAPb_2I_7$ the greatest occurs along the *b* axis, indicating anisotropic compression along the *b* direction (Figure 4.11 and Table 4.5). Furthermore, a negative initial compressibility is also observed for both the *a* and *c* parameters at low-pressure (<3.5 GPa) and high-pressure (>3.5 GPa), respectively (Figure 4.11 and Table 4.5). These results in turn provide further evidence of phase transition between 3-5 GPa for both CMA compounds.

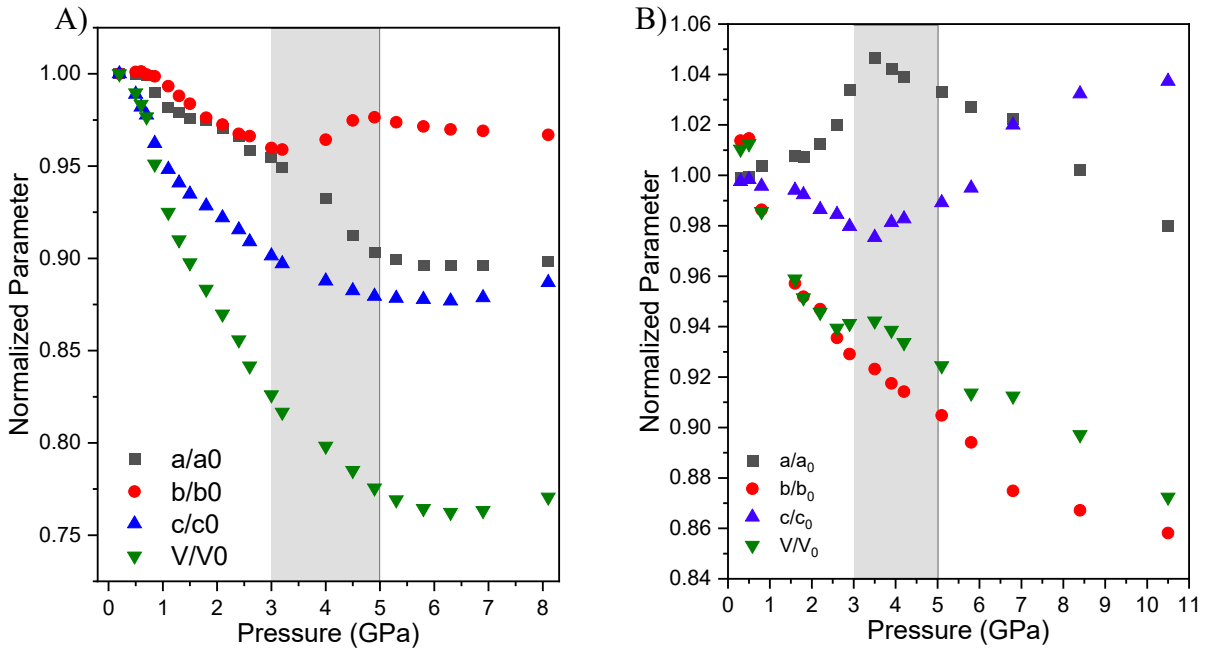

Figure 4.11. LeBail refined lattice parameters. (A) Normalized unit cell parameters of $CMA_2MAPb_2I_7$ and (B) normalized unit cell parameters of $CMA_2FAPb_2I_7$.

Table 4.4. LeBail refined lattice parameters of *$CMA_2MAPb_2I_7$* at HP.

Pressure (GPa)	a (Å)	b (Å)	c (Å)	V (Å^3)
0.20	8.8319	8.7031	45.3086	3482.6415
0.50	8.8288	8.7123	44.8089	3446.6628
0.60	8.8336	8.7142	44.4943	3425.0715
0.70	8.8261	8.6999	44.2984	3401.5053
0.85	8.7406	8.6913	43.6019	3312.3131
1.10	8.6732	8.6448	42.9636	3221.3282
1.30	8.6466	8.5987	42.6283	3169.3934
1.50	8.6195	8.5623	42.3565	3126.0258
1.80	8.607	8.4958	42.0658	3075.9924
2.10	8.5683	8.4635	41.7738	3029.3445
2.40	8.534	8.4198	41.4796	2980.499
2.60	8.4639	8.4093	41.1847	2931.3404
3	8.4326	8.3536	40.8409	2876.9377
3.20	8.3838	8.3459	40.6456	2843.9868
4	8.2347	8.3926	40.2234	2779.8611
4.50	8.0602	8.4831	39.9859	2734.0552
4.90	7.9768	8.4978	39.8471	2701.0456
5.30	7.9424	8.4743	39.7977	2678.6352
5.80	7.917	8.4551	39.7714	2662.2588
6.30	7.9169	8.4407	39.731	2654.9913
6.90	7.9168	8.4342	39.8146	2658.4957
8.10	7.9363	8.4156	40.1831	2683.7781
0	8.81550	8.72710	45.70280	3516.0881

Table 4.5. LeBail refined lattice parameters of $CMA_2FAPb_2I_7$ at HP.

Pressure (GPa)	a (Å)	b (Å)	c (Å)	V (Å^3)
0	8.8939	44.224	8.7817	3454.0519
0.30	8.88552	44.83332	8.76043	3489.8680
0.50	8.89	44.87167	8.76742	3497.4048
0.80	8.926	43.619	8.744	3404.4169
1.60	8.96273	42.32987	8.73024	3312.1783
1.80	8.9583	42.09471	8.7146	3286.2476
2.20	9.004	41.878	8.663	3266.5530
2.60	9.071	41.373	8.646	3244.7962
2.90	9.19647	41.08944	8.60381	3251.1907
3.50	9.30638	40.82654	8.56571	3254.5197
3.90	9.27062	40.57695	8.61797	3241.8521
4.20	9.24209	40.43131	8.63021	3224.8488
5.10	9.18662	40.01519	8.68644	3193.1759
5.80	9.13458	39.54092	8.73743	3155.8712
6.80	9.0944	38.68996	8.95701	3151.6305
8.40	8.91277	38.3497	9.06585	3098.7261
10.50	8.71612	37.95082	9.10946	3013.2633
1.30	8.81590	40.48640	8.64094	3084.1585

Additionally, once again upon decompression both $CMA_2MAPb_2I_7$ and $CMA_2FAPb_2I_7$ were found to nearly return to their pre-compression states (Figure 4.12), thus again indicating reversible modifications of the crystal structures and no metastable changes upon pressure treatment, consistent with the FTIR measurements.

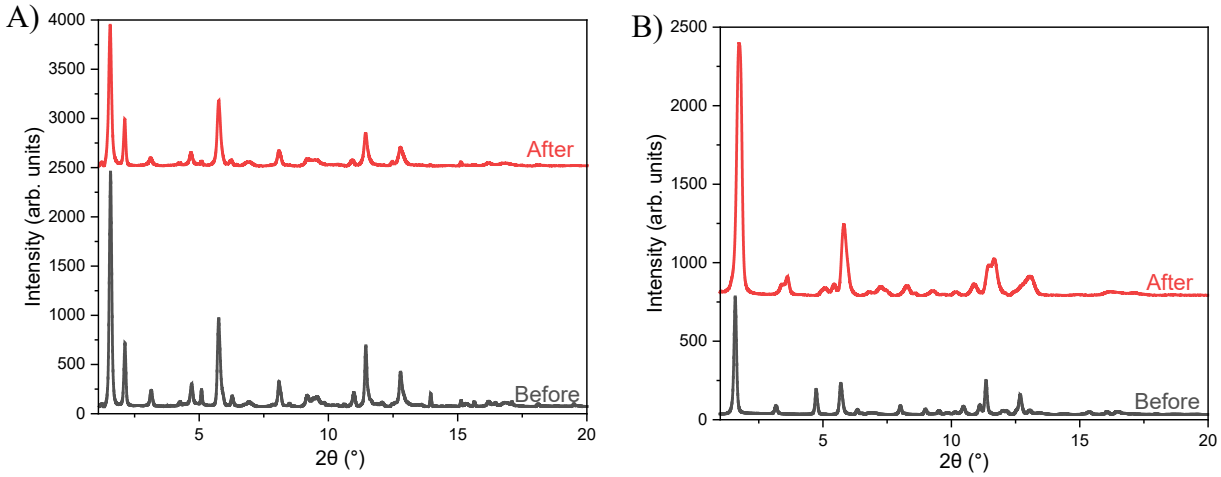

Figure 4.12. XRD patterns of (A) $CMA_2MAPb_2I_7$ and (B) $CMA_2FAPb_2I_7$ before and after compression.

4.3.3 Photoluminescence

To help us examine the impact of high-pressure (HP) on the photoluminescence (PL) emissions we first performed HP PL measurements using 360 nm UV laser excitation. As shown in Figure 4.13, at ambient pressure both $CMA_2MAPb_2I_7$ and $CMA_2FAPb_2I_7$ exhibit two distinct symmetric PL peaks at around 518 nm (peak A) and 578 nm (peak B) respectively. Based on the previous study conducted on CMA_2PbI_4 for n = 1 the major PL peak was found to occur at 521 nm.[23] Thus, the peak at 518 nm is most likely associated with the n = 1 octahedral layer while the peak at 578 nm is most likely associated with the n = 2 octahedral layer. In general, the intensity of both peaks increases upon compression in the low-pressure region (> 2 GPa). The intensity of peak A increases until 1.51 GPa for $CMA_2MAPb_2I_7$ and 0.97 GPa for $CMA_2FAPb_2I_7$, at which point the intensity is around 14 times stronger for $CMA_2MAPb_2I_7$ and two times stronger for $CMA_2FAPb_2I_7$ compared to the values at ambient pressure. In comparison, the intensity of peak B increases until 0.85 GPa for $CMA_2MAPb_2I_7$ and 1.32 GPa for $CMA_2FAPb_2I_7$, at which point the intensity is around 7 times stronger for $CMA_2MAPb_2I_7$ and 1.5 times stronger for $CMA_2FAPb_2I_7$ compared to the values at ambient pressure. These results likely suggest a much greater pressure effect of the PL intensity for $CMA_2MAPb_2I_7$ compared to $CMA_2FAPb_2I_7$. Upon further compression, the peak intensities gradually decrease until full quenching at around 8 GPa for both compounds.

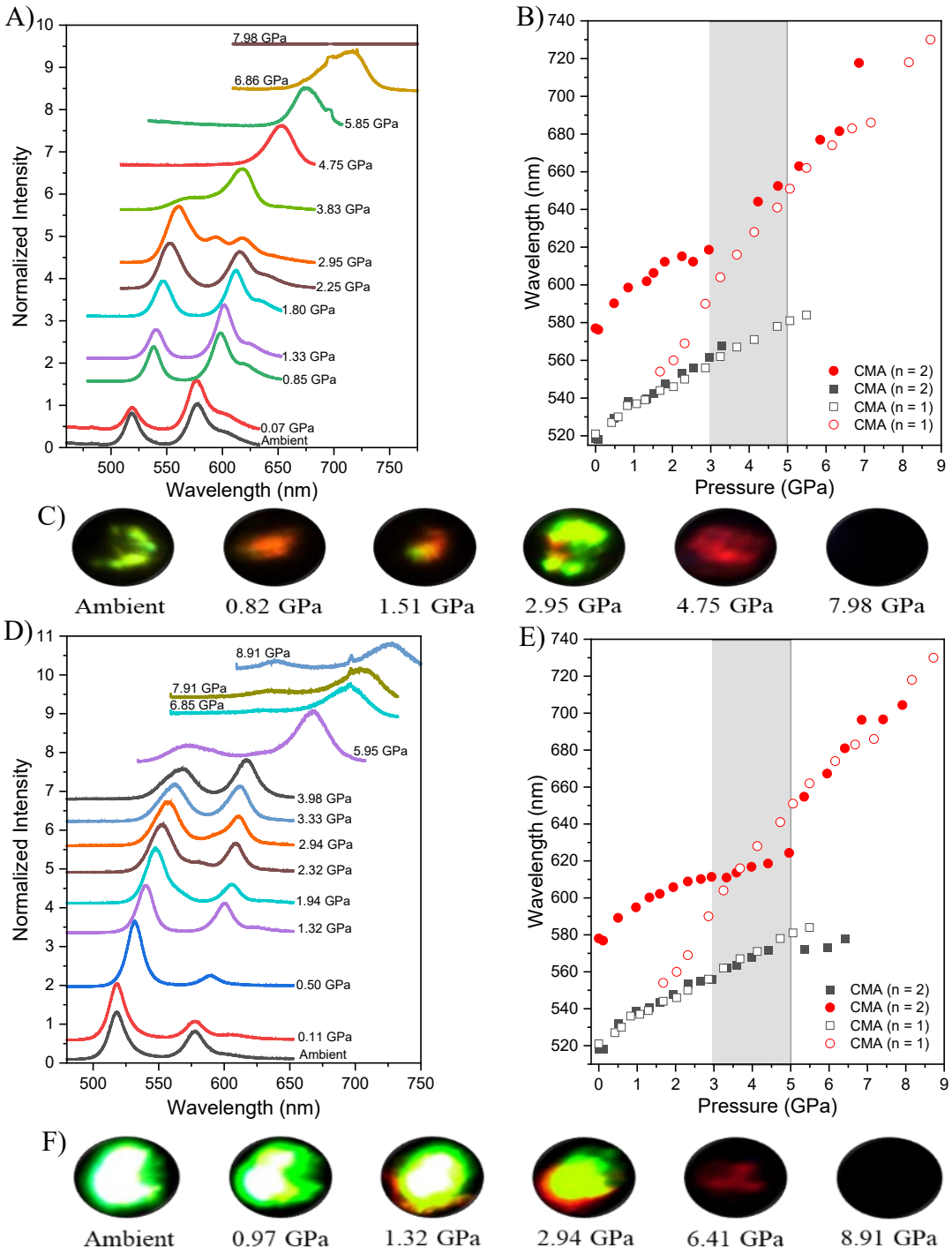

Figure 4.13. Selected PL spectra of $CMA_2MAPb_2I_7$ and $CMA_2FAPb_2I_7$ at HP in comparison with CMA_2PbI_4. (A) PL spectra of $CMA_2MAPb_2I_7$ upon compression, (B) PL emission wavelength as a function of pressure for, and (C) optical images at selected pressures. (D) PL spectra of the $CMA_2FAPb_2I_7$ upon compression, (E) PL emission wavelength as a function of pressure, and (F) optical images at selected pressures.

Upon compression, a redshift of both peaks for both compounds is observed, thus indicating a possible bandgap reduction, consistent with the redshift of the H_N---I hydrogen bonding interactions. The redshift is further evidenced by the optical images in Figure 4.13 which show a clear change from bright green emission at low-pressure to red and eventual black around 8 GPa. Interestingly, peak A is found to quench quicker than peak B, with full quenching observed upon compression to 3.83 GPa for $CMA_2MAPb_2I_7$ and 6.85 GPa for $CMA_2FAPb_2I_7$. Moreover, peak B for both compounds exhibits a prominent increase in the redshift between 3-5 GPa, providing further evidence of the phase transition identified by the FTIR and XRD measurements.

In addition, upon decompression the PL peaks for both compounds were once again found to return to pre-compression shape and position (Figure 4.14), thus indicating reversible PL behavior and no metastable change occurs, consistent with the vibrational spectroscopy and XRD measurements.

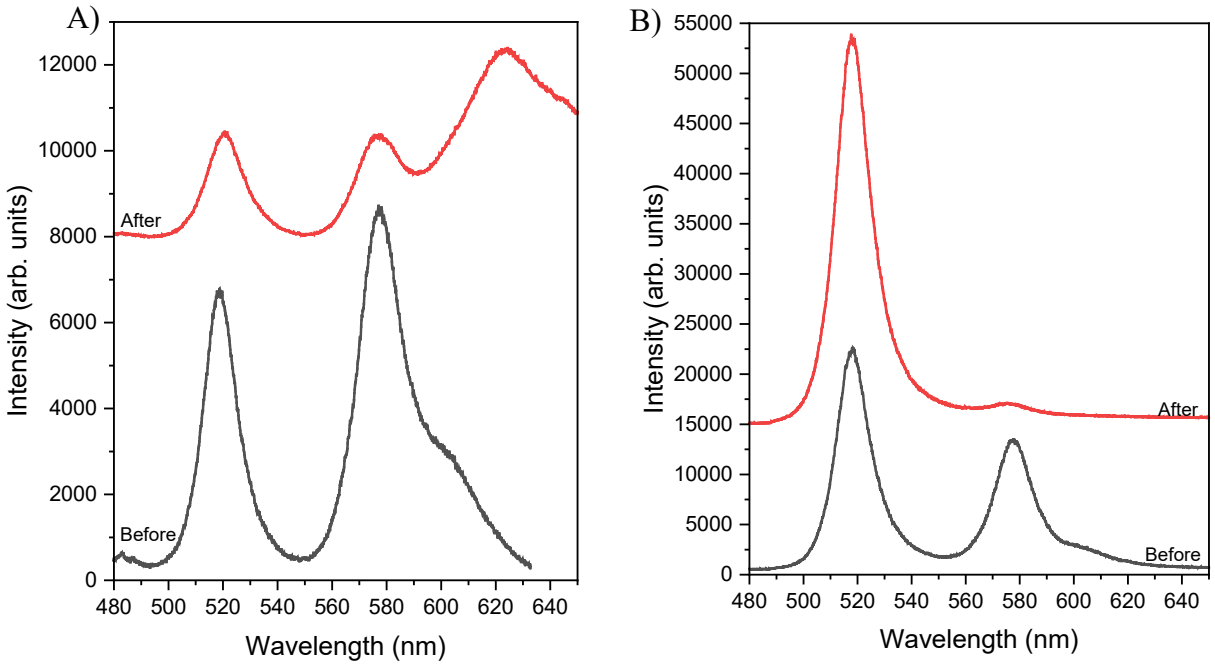

Figure 4.14. PL spectra of $CMA_2MAPb_2I_7$ (A) and $CMA_2FAPb_2I_7$ (B) before and after compression.

4.3.4 UV-Vis Absorption

HP UV-Vis absorptions measurements were used to analyze the impact of HP on the bandgap behavior of both $CMA_2MAPb_2I_7$ and $CMA_2FAPb_2I_7$. As seen in Figure 4.15, both compounds exhibit a redshift in the absorption edge upon compression, thus indicating a bandgap reduction in good agreement with the PL measurements. This is further evidenced by the optical images which show a clear change from a bright red crystal at ambient pressure to gradual dark red upon compression to around 10 GPa for both compounds. Interestingly, for $CMA_2MAPb_2I_7$ a continuous redshift of the absorption is observed upon compression to 4.77 GPa after which further compression to 7.53 GPa results in a temporary blueshift followed by a return to a redshift upon further compression to 9.88 GPa. Furthermore, upon decompression both compounds were found to return to the pre-compression state, indicating reversible bandgap behaviors, again consistent with the PL measurements.

Tuac analysis at ambient pressure indicates a bandgap of 2.08 eV for $CMA_2MAPb_2I_7$ and 2.11 eV for $CMA_2FAPb_2I_7$. A direct bandgap was observed at all pressure points and upon plotting the bandgap as a function of pressure, a monotonic bandgap reduction is observed from 2.08 to 1.95 eV upon compression to 4.77 GPa for $CMA_2MAPb_2I_7$ and 2.11 to 1.86 eV upon compression to 9.99 GPa for $CMA_2FAPb_2I_7$, once again consistent with the redshifts of the two major PL peaks.

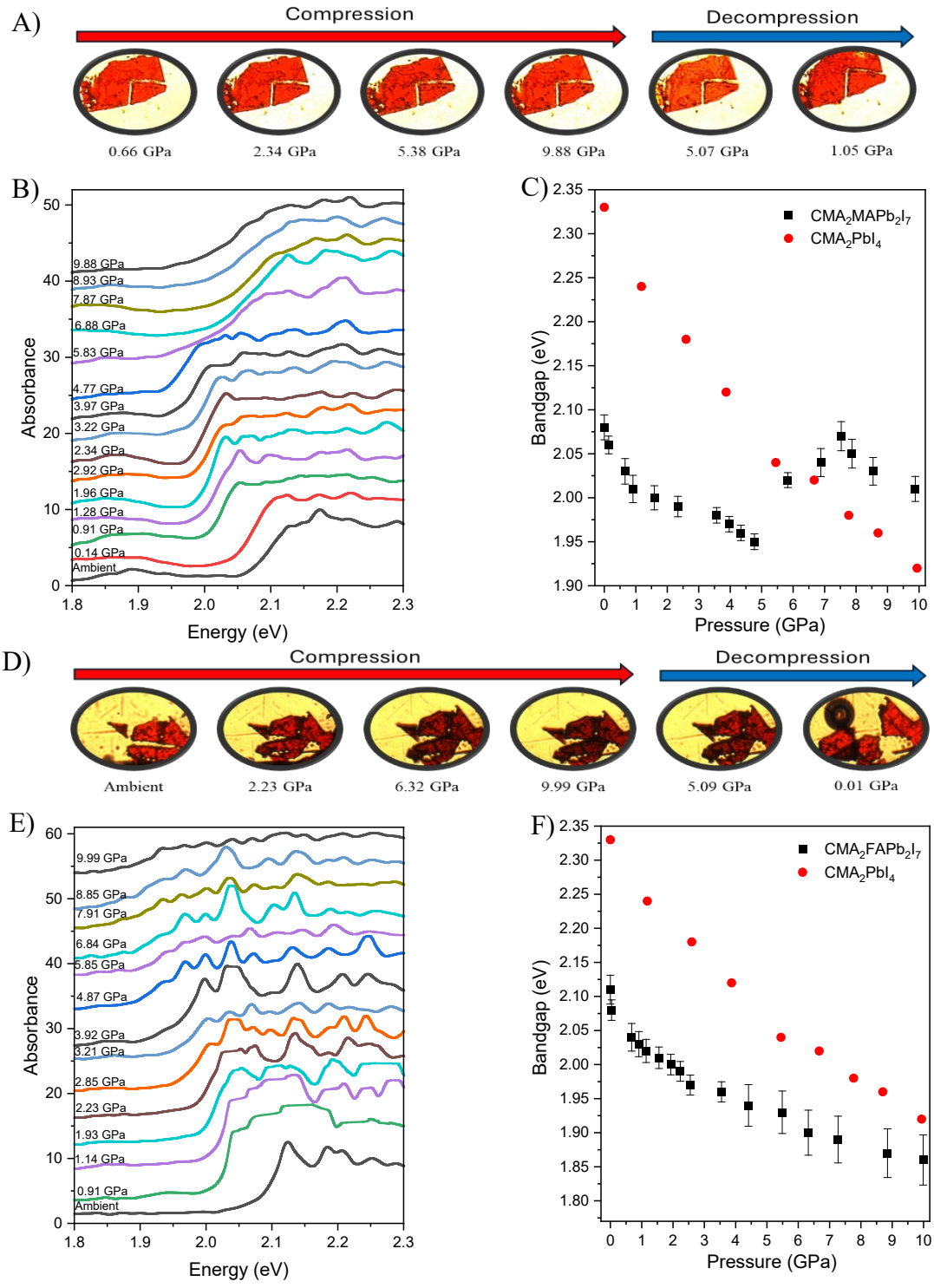

Figure 4.15. UV-Vis absorption of $CMA_2MAPb_2I_7$ and $CMA_2FAPb_2I_7$ at HP in comparison with CMA_2PbI_4. (A) Optical images of $CMA_2MAPb_2I_7$ at selected pressures, (B) absorbance spectra of $CMA_2MAPb_2I_7$ upon compression, and (C) bandgap as a function of pressure. (D) Optical images of $CMA_2FAPb_2I_7$ at selected pressures, (E) absorbance spectra of $CMA_2FAPb_2I_7$ upon compression, and (F) bandgap as a function of pressure.

Additionally, once again upon decompression the absorption edge and bandgap value returned to the pre-compression state for both compounds (Figure 4.16), indicating reversible bandgap behavior consistent with the FTIR, XRD, and PL measurements.

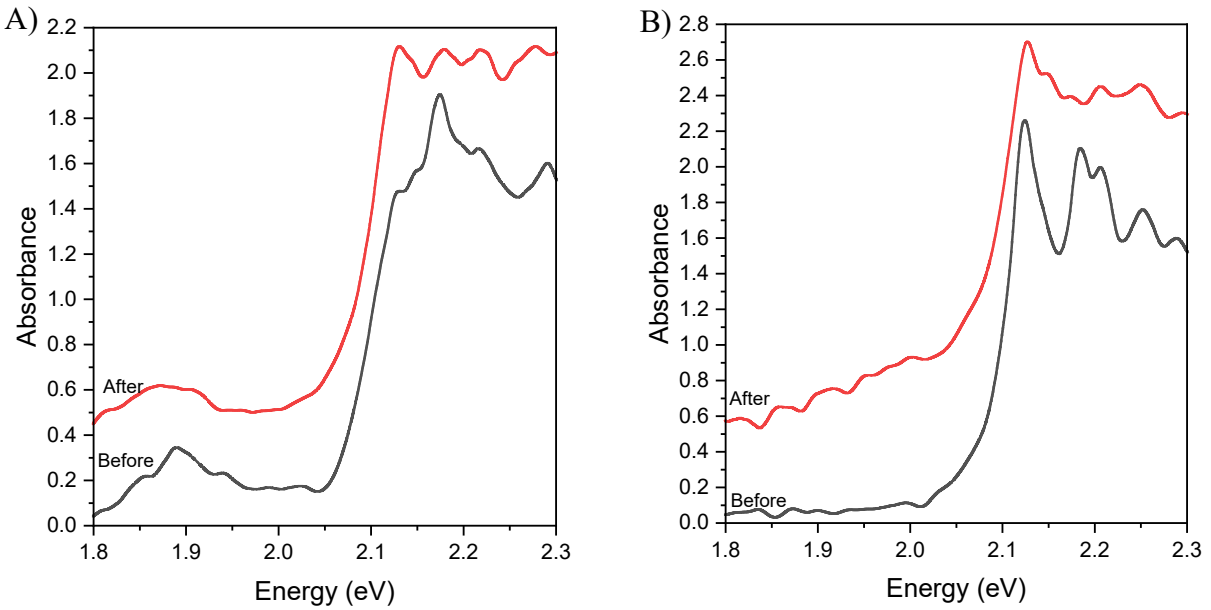

Figure 4.16. UV-Visible absorption spectra of $CMA_2MAPb_2I_7$ (A) and $CMA_2FAPb_2I_7$ (B) before and after compression.

4.4 Conclusions

This study represents the first high-pressure study conducted on both $CMA_2MAPb_2I_7$ and $CMA_2FAPb_2I_7$. FTIR measurements indicate a possible phase transition between 3-5 GPa and amorphization above 4 GPa. Redshifts of the NH_3 bending and NH_3 scissoring modes for both compounds suggests H_N---I hydrogen bonding interactions between the CMA spacers and the lead-iodide octahedra, indicating a possible bandgap reduction likely resulting from shortening of the Pb-I bond lengths. The phase transition was further confirmed by the XRD measurements and LeBail refinements of the 1D powder patterns identified the phase transition as isostructural. Furthermore, a possible negative linear compressibility of the *b* unit cell parameter was observed

for $CMA_2MAPb_2I_7$ upon compression beyond 3 GPa with similar negative linear compressibility previously observed in CMA_2PbI_4. A negative linear compressibility of both the *a* parameter at low-pressure (<3.5 GPa) and the *c* parameter at high-pressure (>3.5 GPa) was also observed for $CMA_2FAPb_2I_7$. The PL measurements indicate a prominent redshift of the second PL peak (578 nm) for both compounds between 3-5 GPa provides further evidence of the phase transition. The redshifts also indicate a possible bandgap reduction consistent with the redshift of the H_N---*I* hydrogen bonding interactions identified by the FTIR measurements. UV-Vis absorption measurements confirmed the bandgap reductions with reductions of 2.08 to 1.95 eV upon compression to 4.77 GPa and 2.11 to 1.86 eV upon compression to 9.99 GPa for $CMA_2MAPb_2I_7$ and $CMA_2FAPb_2I_7$, respectively. Computational studies along with further Rietveld refinements of the XRD patterns are required to provide further confirmation of the proposed pressure-induced structural modifications and optoelectronic properties as well to identify the origins behind the phase transition and mechanisms behind the pressure-induced optoelectronic properties.

4.5 References

(1) Mao, L.; Stoumpos, C. C.; Kanatzidis, M. G. Two-Dimensional Hybrid Halide Perovskites: Principles and Promises. *Journal of the American Chemical Society* **2019**, *141* (3), 1171-1190.

(2) Zhang, L.; Wang, K.; Lin, Y.; Zou, B. Pressure Effects on the Electronic and Optical Properties in Low-Dimensional Metal Halide Perovskites. *The Journal of Physical Chemistry Letters* **2020**, *11* (12), 4693-4701.

(3) Zhang, P.; Li, M.; Chen, W.-C. A Perspective on Perovskite Solar Cells: Emergence, Progress, and Commercialization. *Frontiers in Chemistry* **2022**, *10*, Review.

(4) Al-Ashouri, A.; Köhnen, E.; Li, B.; Magomedov, A.; Hempel, H.; Caprioglio, P.; Márquez, J. A.; Morales Vilches, A. B.; Kasparavicius, E.; Smith, J. A.; Phung, N.; Menzel, D.; Grischek, M.; Kegelmann, L.; Skroblin, D.; Gollwitzer, C.; Malinauskas, T.; Jošt, M.; Matic, G.; Rech, B.; Schlatmann, R.; Topic, M.; Korte, L.; Abate, A.; Stannowski, B.; Neher, D.; Stolterfoht, M.; Unold, T.; Getautis, V.; Albrecht, S. Monolithic perovskite/silicon tandem solar cell with >29% efficiency by enhanced hole extraction. *Science* **2020**, *370* (6522), 1300-1309.

(5) Liao, J. H.-H. Behind the Breakthrough of the ~30% Perovskite Solar Cell. *Joule* **2021**, *5* (2), 295-297.

(6) Stoumpos, C. C.; Kanatzidis, M. G. The Renaissance of Halide Perovskites and Their Evolution as Emerging Semiconductors. *Accounts of Chemical Research* **2015**, *48* (10), 2791-2802.

(7) Ortiz-Cervantes, C.; Carmona-Monroy, P.; Solis-Ibarra, D. Two-Dimensional Halide Perovskites in Solar Cells: 2D or not 2D? *ChemSusChem* **2019**, *12* (8), 1560-1575.

(8) Chakhmouradian, A. R.; Woodward, P. M. Celebrating 175 years of perovskite research: a tribute to Roger H. Mitchell. *Physics and Chemistry of Minerals* **2014**, *41* (6), 387-391.

(9) Jerpoth, S. S.; Iannello, J.; Aboagye, E. A.; Yenkie, K. M. Computer-aided synthesis of cost-effective perovskite crystals: an emerging alternative to silicon solar cells. *Clean Technologies and Environmental Policy* **2020**, *22* (5), 1187-1198.

(10) Wei, Y.; Chu, H.; Chen, B.; Tian, Y.; Yang, X.; Cai, B.; Zhang, Y.; Zhao, J. Two-dimensional cyclohexane methylamine based perovskites as stable light absorbers for solar cells. *Solar Energy* **2020**, *201*, 13-20.

(11) Wei, Y.; Chu, H.; Tian, Y.; Chen, B.; Wu, K.; Wang, J.; Yang, X.; Cai, B.; Zhang, Y.; Zhao, J. Reverse-Graded 2D Ruddlesden–Popper Perovskites for Efficient Air-Stable Solar Cells. *Advanced Energy Materials* **2019**, *9* (21), 1900612.

(12) Ehrler, B.; Alarcón-Lladó, E.; Tabernig, S. W.; Veeken, T.; Garnett, E. C.; Polman, A. Photovoltaics Reaching for the Shockley–Queisser Limit. *ACS Energy Letters* **2020**, *5* (9), 3029-3033.

(13) Rühle, S. Tabulated values of the Shockley–Queisser limit for single junction solar cells. *Solar Energy* **2016**, *130*, 139-147.

(14) Hu, J.; Yan, L.; You, W. Two-Dimensional Organic–Inorganic Hybrid Perovskites: A New Platform for Optoelectronic Applications. *Advanced Materials* **2018**, *30* (48), 1802041.

(15) Smith, I. C.; Hoke, E. T.; Solis-Ibarra, D.; McGehee, M. D.; Karunadasa, H. I. A Layered Hybrid Perovskite Solar-Cell Absorber with Enhanced Moisture Stability. *Angewandte Chemie International Edition* **2014**, *53* (42), 11232-11235.

(16) Cao, D. H.; Stoumpos, C. C.; Farha, O. K.; Hupp, J. T.; Kanatzidis, M. G. 2D Homologous Perovskites as Light-Absorbing Materials for Solar Cell Applications. *Journal of the American Chemical Society* **2015**, *137* (24), 7843-7850.

(17) Peng, W.; Yin, J.; Ho, K.-T.; Ouellette, O.; De Bastiani, M.; Murali, B.; El Tall, O.; Shen, C.; Miao, X.; Pan, J.; Alarousu, E.; He, J.-H.; Ooi, B. S.; Mohammed, O. F.; Sargent, E.; Bakr, O. M. Ultralow Self-Doping in Two-dimensional Hybrid Perovskite Single Crystals. *Nano Letters* **2017**, *17* (8), 4759-4767.

(18) Wu, X.; Trinh, M. T.; Niesner, D.; Zhu, H.; Norman, Z.; Owen, J. S.; Yaffe, O.; Kudisch, B. J.; Zhu, X. Y. Trap States in Lead Iodide Perovskites. *Journal of the American Chemical Society* **2015**, *137* (5), 2089-2096.

(19) Jia, Q.-Q.; Tong, L.; Lun, M.-M.; Fu, D.-W.; Zhang, T.; Lu, H.-F. Two-Dimensional Organic–Inorganic Hybrid Materials with Dielectric Switching and Photoluminescence Properties. *Crystal Growth & Design* **2022**, *22* (5), 2799-2805.

(20) Juarez-Perez, E. J.; Ono, L. K.; Qi, Y. Thermal degradation of formamidinium based lead halide perovskites into sym-triazine and hydrogen cyanide observed by coupled thermogravimetry-mass spectrometry analysis. *Journal of Materials Chemistry A* **2019**, *7* (28), 16912-16919.

(21) Ma, F.; Li, J.; Li, W.; Lin, N.; Wang, L.; Qiao, J. Stable α/δ phase junction of formamidinium lead iodide perovskites for enhanced near-infrared emission. *Chemical Science* **2017**, *8* (1), 800-805.

(22) Jeong, J.; Kim, M.; Seo, J.; Lu, H.; Ahlawat, P.; Mishra, A.; Yang, Y.; Hope, M. A.; Eickemeyer, F. T.; Kim, M.; Yoon, Y. J.; Choi, I. W.; Darwich, B. P.; Choi, S. J.; Jo, Y.; Lee, J. H.; Walker, B.; Zakeeruddin, S. M.; Emsley, L.; Rothlisberger, U.; Hagfeldt, A.; Kim, D. S.; Gratzel, M.; Kim, J. Y. Pseudo-halide anion engineering for α-$FAPbI_3$ perovskite solar cells. *Nature* **2021**, *592* (7854), 381-385.

(23) Ratté, J.; Macintosh, M. F.; DiLoreto, L.; Liu, J.; Mihalyi-Koch, W.; Hautzinger, M. P.; Guzei, I. A.; Dong, Z.; Jin, S.; Song, Y. Spacer-Dependent and Pressure-Tuned Structures and Optoelectronic Properties of 2D Hybrid Halide Perovskites. *The Journal of Physical Chemistry Letters* **2023**, *14* (2), 403-412.

5. Summary and Future Work

5.1 Summary

The use of two-dimensional hybrid organic-inorganic perovskites (HOIPs) in optoelectronic applications, in particular solar cells, has increased substantially over the years due to their high stability, greater organic-inorganic combinations for synthesis, ease of fabrication, and ease of modification of both the structures and optoelectronic properties. Pressure is an easy and effective method for studying the behavior and modifying the properties of several materials. For 2D HOIPs high-pressure (HP) is used to induce modifications to the crystal structures, changes in the bandgap, and to tune the photoluminescence (PL) emission and wavelength. In this work HP was used to induce modifications to the structures and optoelectronic properties of $DPDAPbI_4$, a Dion-Jacobson type 2D HOIP with a highly rigid organic spacer, and $CMA_2MAPb_2I_7$ and $CMA_2FAPb_2I_7$, n = 2 Ruddlesden-Popper type 2D HOIPs with a very soft organic spacer.

In chapter 3, the structures and optoelectronic properties of $DPDAPbI_4$ were studied at HP using Vibrational spectroscopy, X-ray diffraction (XRD), PL, UV-Vis absorption, and density functional theory calculations (DFT). A phase transition at 1.5 GPa was proposed by the vibrational spectroscopy measurements, later confirmed by the XRD and PL measurements and identified as isostructural by the XRD measurements. The greatest compressibility was found to occur during Phase I with a bulk modulus of 11.77 GPa and an anisotropic compression along the *c* direction was also observed. Amorphization was observed upon compression beyond 5 GPa. H_N---*I* bonding was also observed through the vibrational spectroscopy measurements. A 3-4-fold increase in the intensity of the major free exciton (FE) peak upon compression to 1.49 GPa was observed through

the PL measurements followed by a gradual decrease in intensity until quenching at around 6 GPa. Broadening of the self-trapped exciton (STE) peak was observed upon compression to 1.23 GPa. A bandgap reduction from 2.26 to 1.87 eV upon compression to 8.84 GPa was observed by the UV-Vis absorption measurements. Distortion analysis indicated a significant enhancement in the octahedral distortion between 1-2 GPa, in good agreement with the broadening of the STE peak. DFT calculations confirm the enhancement of the N–H···I hydrogen bonding interactions, resulting in the shortening of the Pb-I bond lengths upon compression and leading to the overall bandgap reduction. The pressure-induced modifications of $DPDAPbI_4$ are mainly driven by interactions between the rigid organic spacer and the lead-iodide octahedra, thus indicating a strong likelihood of reversible structural and optoelectronic property changes.

In chapter 4, the structures and optoelectronic properties of $CMA_2MAPb_2I_7$ and $CMA_2FAPb_2I_7$ were studied at HP using Fourier-transform infrared spectroscopy, XRD, PL, and UV-Vis absorption. The FIIR measurements propose a possible phase transition between 3-5 GPa for both compounds, later confirmed and identified as isostructural by the XRD measurements. H_N---I bonding was also observed along with amorphization beyond 4 GPa. Furthermore, a negative linear compressibility of the *b* unit cell parameter was observed for $CMA_2MAPb_2I_7$ upon compression beyond 3 GPa, and of both the *a* parameter at low-pressure (<3.5 GPa) and the *c* parameter at high-pressure (>3.5 GPa) was also observed for $CMA_2FAPb_2I_7$. PL measurements provide further confirmation of the phase transition resulting from the prominent redshift of the second PL peak (578 nm). UV-Vis absorption measurements indicate bandgap reductions of 2.08 to 1.95 eV upon compression to 4.77 GPa and 2.11 to 1.86 eV upon compression to 9.99 GPa for $CMA_2MAPb_2I_7$ and $CMA_2FAPb_2I_7$, respectively. These reductions are likely to result from

shortening of the Pb-I bond lengths most likely from enhancement of the N–H···I hydrogen bonding interactions upon compression. All measurements in general showed a return to the pre-compression state, indicating reversible modifications of both the structures and optoelectronic properties as well as no metastable changes upon compression.

5.2 Future Work

A solid understanding of $DPDAPbI_4$, $CMA_2MAPb_2I_7$, and $CMA_2FAPb_2I_7$ has been established throughout this study, however further experiments and computational work are required to strengthen the understanding of 2D HOIPs at HP.

For $CMA_2MAPb_2I_7$, and $CMA_2FAPb_2I_7$ single crystal XRD measurements at HP should be performed to provide a better understanding of the atomic positions and atom occupancy. Rietveld refinements of the 1D XRD powder patterns are also required to provide a deeper understanding of the compressibility and the potential negative linear compressibility.

Computational studies should also be performed for both $CMA_2MAPb_2I_7$, and $CMA_2FAPb_2I_7$ to further the understanding of the pressure-induced structural modifications and optoelectronic properties and to help propose the mechanisms behind these changes. It is likely believed that the bandgap reduction is a result of shortening of the Pb-I bond lengths due to enhancement of the N–H···I hydrogen bonding interactions upon compression.

Finally, it would also be of high interest to study tin-based 2D HOIPs at HP. Lead-iodide 2D HOIPs have been the most extensively studied HOIPs at HP over the years, showing intriguing

modifications to both the structures and optoelectronic properties. Tin is another common metal used to form 2D HOIPs[1], and given the highly interesting properties of lead-based 2D HOIPs at HP, studying tin-based 2D HOIPs at HP would provide a solid comparison between structures and properties of both at HP. Vibrational and XRD measurements should be performed to identify possible structural modifications at HP while PL and UV-Vis absorption measurements should be used to probe the optoelectronic properties at HP.

5.3 References

(1) Mao, L.; Stoumpos, C. C.; Kanatzidis, M. G. Two-Dimensional Hybrid Halide Perovskites: Principles and Promises. *Journal of the American Chemical Society* **2019**, *141* (3), 1171-1190. DOI: 10.1021/jacs.8b10851.

Aditya Kutty
University of Western Ontario

EDUCATION

Master of Science in Chemistry **September 2022 – Present**
University of Western Ontario, ON, Canada
Supervisor: Yang Song

Honours Bachelor of Science (BSc) **2018 – 2022**
Specialist in Chemistry
University of Toronto, ON, Canada

TEACHING EXPERIENCE

Teaching Assistant **January 2024 – April 2024**
Lab TA for Discovering Chemical Energetics (Chemistry 1302B)
University of Western Ontario, ON, Canada
Professors: Christina Booker, Francois Lagugne-Labarthet, Jamie Noel, and Yang Song

Teaching Assistant **September 2023 – December 2023**
Lab TA for Discovering Chemical Structure (Chemistry 1301A)
University of Western Ontario, ON, Canada
Professors: Christina Booker, Felix Lee, and Lars Konermann

Teaching Assistant **January 2023 – April 2023**
Lab TA for Discovering Chemical Energetics (Chemistry 1302B)
University of Western Ontario, ON, Canada
Professors: Christina Booker, Jamie Noel, Ken Yeung, and Yang Song

Teaching Assistant **September 2022 – December 2022**
Lab TA for Discovering Chemical Structure (Chemistry 1301A)
University of Western Ontario, ON, Canada
Professors: Christina Booker, Felix Lee, and Kanwal Tanwir

RESEARCH EXPERIENCE

Master Student in Chemistry **September 2022 – Present**
University of Western Ontario, ON, Canada
Supervisor: Yang Song

PUBLICATIONS

A. Kutty, J. Ratté, R. Guan, J. Liu, S. Tao, Y. Lin, M. P. Hautzinger, W. Mihalyi-Koch, S. Jin, and Y. Song. Pressure-Tuned Structures and Optoelectronic Properties of a Dion-Jacobson Type 2D Hybrid Organic-Inorganic Lead Iodide Perovskite, in Preparation.

R. Guan, J. Liu, **A. Kutty**, Z. Yu, Y. Ji, Y. Li, and Y. Song. Pressure Mediated Phase Transition and Dihydrogen Bonding Formation in Trimethylamine Borane. *J. Mater. Chem. C*, **2024**, *12* (37), 14833-14843.

CONFERENCE PRESENTATIONS

A. Kutty, J. Ratté, R. Guan, J. Liu, S. Tao, Y. Lin, M. Macintosh, W. Mihalyi-Koch, M. P. Hautzinger, S. Jin, and Y. Song. "Pressure-Tuned Structures and Optoelectronic Properties of a Dion-Jacobson Type 2D Hybrid Organic-Inorganic Lead Iodide Perovskite", Canadian Chemistry Conference and Exhibition 2024, Winnipeg, MB, Canada, **2024**.